

UNIVERSIDADE DE LISBOA  
FACULDADE DE CIÊNCIAS  
DEPARTAMENTO DE FÍSICA



# **Modelling the Head and Neck Region for Microwave Imaging of Cervical Lymph Nodes**

Ana Catarina Domingos Pelicano

**Mestrado Integrado em Engenharia Biomédica e Biofísica**  
Perfil em Radiações em Diagnóstico e Terapia

Dissertação orientada por:  
Prof. Raquel Conceição  
Prof. Sara Madeira

# Acknowledgements

I wish to express my most sincere gratitude to both my supervisors Prof. Raquel Conceição and Prof. Sara Madeira for their guidance, expertise, unconditional support, patience and encouragement throughout this learning process. I am especially grateful to Prof. Raquel for her kindness and encouraging words during a very vulnerable period of my personal life and for presenting me new challenges, introducing me to the topic and providing me the opportunity to enter her research group. I could not ask for a better mentor. I would like to extend my gratitude to my colleagues and friends in the group, Daniela and Matteo, for their enthusiasm and motivation, and for patiently answering my endless questions. I am sincerely thankful to the staff in the Instituto de Biofísica e Engenharia Biomédica, IBEB (Institute of Biophysics and Biomedical Engineering).

I wish to express my gratitude to all my colleagues and friends who have accompanied me during these last 5 years in Biomedical Engineering, in particular Inês, Daniela, Mariana, Laëticia, Sofia, and Campagnolo for all the moments of laugh and despair we shared. I was very lucky to be a part of such an intelligent, motivated and funny group of people.

I would like to thank to my closest friends Rita, Sardo, Malcato, Marco and Gonçalo who have always been there for me, for their friendship, inspiration, motivation and advice. A special word of appreciation goes to my best friend Rita for her endless support and patience, and also for her valuable suggestions throughout this work.

Finally, I would like to show my appreciation for my family's unconditional support and love throughout the years. A special thank you to my parents Paula and Jorge for believing in me and give the courage to fight every battle to achieve my professional and personal goals, to my little sister Inês for reminding me to laugh and enjoy every step of the way, to my grandparents Tó and Talinha for their kindness and wisdom and to my aunts and uncles, for their motivation and trust in me.

## Resumo

O termo “cancro da cabeça e pescoço” refere-se a um qualquer tipo de cancro com início nas células epiteliais das cavidades oral e nasal, seios perinasais, glândulas salivares, faringe e laringe. Estes tumores malignos apresentaram, em 2018, uma incidência mundial de cerca de 887.659 novos casos e taxa de mortalidade superior a 51%. Aproximadamente 80% dos novos casos diagnosticados nesse ano revelaram a proliferação de células cancerígenas dos tumores para outras regiões do corpo através dos vasos sanguíneos e linfáticos das redondezas. De forma a determinar o estado de desenvolvimento do cancro e as terapias a serem seguidas, é fundamental a avaliação dos primeiros gânglios linfáticos que recebem a drenagem do tumor primário – os gânglios sentinela – e que, por isso, apresentam maior probabilidade de se tornarem os primeiros alvos das células tumorais. Gânglios sentinela saudáveis implicam uma menor probabilidade de surgirem metástases, isto é, novos focos tumorais decorrentes da disseminação do cancro para outros órgãos.

O procedimento *standard* que permite o diagnóstico dos gânglios linfáticos cervicais, gânglios que se encontram na região da cabeça e pescoço, e o estadiamento do cancro consiste na remoção cirúrgica destes gânglios e subsequente histopatologia. Para além de ser um procedimento invasivo, a excisão cirúrgica dos gânglios linfáticos representa perigos tanto para a saúde mental e física dos pacientes, como para a sua qualidade de vida. Dores, aparência física deformada (devido a cicatrizes), perda da fala ou da capacidade de deglutição são algumas das repercussões que poderão advir da remoção de gânglios linfáticos da região da cabeça e pescoço. Adicionalmente, o risco de infeção e linfedema – acumulação de linfa nos tecidos intersticiais – aumenta significativamente com a remoção de uma grande quantidade de gânglios linfáticos saudáveis. Também os encargos para os sistemas de saúde são elevados devido à necessidade de monitorização destes pacientes e subseqüentes terapias e cuidados associados à morbilidade, como é o caso da drenagem linfática manual e da fisioterapia.

O desenvolvimento de novas tecnologias de imagem da cabeça e pescoço requer o uso de modelos realistas que simulem o comportamento e propriedades dos tecidos biológicos. A imagem médica por micro-ondas é uma técnica promissora e não invasiva que utiliza radiação não ionizante, isto é, sinais com frequências na gama das micro-ondas cujo comportamento depende do contraste dielétrico entre os diferentes tecidos atravessados, pelo que é possível identificar regiões ou estruturas de interesse e, consequentemente, complementar o diagnóstico. No entanto, devido às suas características, este tipo de modalidade apenas poderá ser utilizado para a avaliação de regiões anatómicas pouco profundas.

Estudos indicam que os gânglios linfáticos com células tumorais possuem propriedades dielétricas distintas dos gânglios linfáticos saudáveis. Por esta razão e juntamente pelo facto da sua localização pouco profunda, consideramos que os gânglios linfáticos da região da cabeça e pescoço constituem um excelente candidato para a utilização de imagem médica por radar na frequência das micro-ondas como ferramenta de diagnóstico.

Até à data, não foram efetuados estudos de desenvolvimento de modelos da região da cabeça e pescoço focados em representar realisticamente os gânglios linfáticos cervicais. Por este motivo, este projeto consistiu no desenvolvimento de dois geradores de fantasmas tridimensionais da região da cabeça e pescoço – um gerador de fantasmas numéricos simples (gerador I) e um gerador de fantasmas numéricos mais complexos e anatomicamente realistas, que foi derivado de imagens de ressonância magnética e que inclui as propriedades dielétricas realistas dos tecidos biológicos (gerador II). Ambos os geradores permitem obter fantasmas com diferentes níveis de complexidade e assim acompanhar diferentes fases no processo de desenvolvimento de equipamentos médicos de imagiologia por micro-ondas. Todos os

fantomas gerados, e principalmente os fantomas anatomicamente realistas, poderão ser mais tarde impressos a três dimensões.

O processo de construção do gerador I compreendeu a modelação da região da cabeça e pescoço em concordância com a anatomia humana e distribuição dos principais tecidos, e a criação de uma interface para a personalização dos modelos (por exemplo, a inclusão ou remoção de alguns tecidos é dependente do propósito para o qual cada modelo é gerado). O estudo minucioso desta região levou à inclusão de tecidos ósseos, musculares e adiposos, pele e gânglios linfáticos nos modelos. Apesar destes fantomas serem bastante simples, são essenciais para o início do processo de desenvolvimento de dispositivos de imagem médica por micro-ondas dedicados ao diagnóstico dos gânglios linfáticos cervicais.

O processo de construção do gerador II foi fracionado em 3 grandes etapas devido ao seu elevado grau de complexidade. A primeira etapa consistiu na criação de uma *pipeline* que permitiu o processamento das imagens de ressonância magnética. Esta *pipeline* incluiu: a normalização dos dados, a subtração do *background* com recurso a máscaras binárias manualmente construídas, o tratamento das imagens através do uso de filtros lineares (como por exemplo, filtros passa-baixo ideal, Gaussiano e Butterworth) e não-lineares (por exemplo, o filtro mediana), e o uso de algoritmos não supervisionados de *machine learning* para a segmentação dos vários tecidos biológicos presentes na região cervical, tais como o *K-means*, *Agglomerative Hierarchical Clustering*, *DBSCAN* e *BIRCH*. Visto que cada algoritmo não supervisionado de *machine learning* anteriormente referido requer diferentes hiperparâmetros, é necessário proceder a um estudo pormenorizado que permita a compreensão do modo de funcionamento de cada algoritmo individualmente e a sua interação / performance com o tipo de dados tratados neste projeto (isto é, dados de exames de ressonâncias magnéticas) com vista a escolher empiricamente o leque de valores de cada hiperparâmetro que deve ser considerado, e ainda as combinações que devem ser testadas. Após esta fase, segue-se a avaliação da combinação de hiperparâmetros que resulta na melhor segmentação das estruturas anatómicas. Para esta avaliação são consideradas duas metodologias que foram combinadas: a utilização de métricas que permitam avaliar a qualidade do *clustering* (como por exemplo, o Silhouette Coefficient, o índice de Davies-Bouldin e o índice de Calinski-Harabasz) e ainda a inspeção visual. A segunda etapa foi dedicada à introdução manual de algumas estruturas, como a pele e os gânglios linfáticos, que não foram segmentadas pelos algoritmos de *machine learning* devido à sua fina espessura e pequena dimensão, respetivamente. Finalmente, a última etapa consistiu na atribuição das propriedades dielétricas, para uma frequência pré-definida, aos tecidos biológicos através do Modelo de Cole-Cole de quatro pólos. Tal como no gerador I, foi criada uma interface que permitiu ao utilizador decidir que características pretende incluir no fantoma, tais como: os tecidos a incluir (tecido adiposo, tecido muscular, pele e / ou gânglios linfáticos), relativamente aos gânglios linfáticos o utilizador poderá ainda determinar o seu número, dimensões, localização em níveis e estado clínico (saúdável ou metastizado) e finalmente, o valor de frequência para o qual pretende obter as propriedades dielétricas (permitividade relativa e condutividade) de cada tecido biológico.

Este projeto resultou no desenvolvimento de um gerador de modelos realistas da região da cabeça e pescoço com foco nos gânglios linfáticos cervicais, que permite a inserção de tecidos biológicos, tais como o tecido muscular e adiposo, pele e gânglios linfáticos e aos quais atribui as propriedades dielétricas para uma determinada frequência na gama de micro-ondas. Estes modelos computacionais resultantes do gerador II, e que poderão ser mais tarde impressos em 3D, podem vir a ter grande impacto no processo de desenvolvimento de dispositivos médicos de imagem por micro-ondas que visam diagnosticar gânglios linfáticos cervicais, e consequentemente, contribuir para um processo não invasivo de estadiamento do cancro da cabeça e pescoço.

**Palavras-chave:** cancro da cabeça e pescoço; gânglios linfáticos cervicais; fantomas numéricos; fantomas antropomórficos; segmentação de MRI; propriedades dielétricas.

# Abstract

Head and neck cancer is a broad term referring to any epithelial malignancies arising in the paranasal sinuses, nasal and oral cavities, salivary glands, pharynx, and larynx. In 2018, approximately 80% of the newly diagnosed head and neck cancer cases resulted in tumour cells spreading to neighbouring lymph and blood vessels. In order to determine cancer staging and decide which follow-up exams and therapy to follow, physicians excise and assess the Lymph Nodes (LNs) closest to the primary site of the head and neck tumour – the sentinel nodes – which are the ones with highest probability of being targeted by cancer cells. The standard procedure to diagnose the Cervical Lymph Nodes (CLNs), *i.e.* lymph nodes within the head and neck region, and determine the cancer staging frequently involves their surgical removal and subsequent histopathology. Besides being invasive, the removal of the lymph nodes also has negative impact on patients' quality of life, it can be health threatening, and it is costly to healthcare systems due to the patients' needs for follow-up treatments/cares.

Anatomically realistic phantoms are required to develop novel technologies tailored to image head and neck regions. Medical MicroWave Imaging (MWI) is a promising non-invasive approach which uses non-ionizing radiation to screen shallow body regions, therefore cervical lymph nodes are excellent candidates to this imaging modality. In this project, a three-dimensional (3D) numerical phantom generator (generator I) and a Magnetic Resonance Imaging (MRI)-derived anthropomorphic phantom generator (generator II) of the head and neck region were developed to create phantoms with different levels of complexity and realism, which can be later 3D printed to test medical MWI devices. The process of designing the numerical phantom generator included the modelling of the head and neck regions according to their anatomy and the distribution of their main tissues, and the creation of an interface which allowed the users to personalise the model (e.g. include or remove certain tissues, depending on the purpose of each generated model). To build the anthropomorphic phantom generator, the modelling process included the creation of a pipeline of data processing steps to be applied to MRIs of the head and neck, followed by the development of algorithms to introduce additional tissues to the models, such as skin and lymph nodes, and finally, the assignment of the dielectric properties to the biological tissues. Similarly, this generator allowed users to decide the features they wish to include in the phantoms.

This project resulted in the creation of a generator of 3D anatomically realistic head and neck phantoms which allows the inclusion of biological tissues such as skin, muscle tissue, adipose tissue, and LNs, and assigns state-of-the-art dielectric properties to the tissues. These phantoms may have a great impact in the development process of MWI devices aimed at screening and diagnosing CLNs, and consequently, contribute to a non-invasive staging of the head and neck cancer.

**Keywords:** head and neck cancer; cervical lymph nodes; numerical phantoms; anthropomorphic phantoms; MRI segmentation; dielectric properties.

# Contents

|   |           |
|---|-----------|
| Acknowledgements.....                                   | ii        |
| Resumo .....  | iii       |
| Abstract .....  | v         |
| List of Figures .....                                   | viii      |
| List of Tables.....                                     | xi        |
| Acronyms .....  | xii       |
| <b>1. Chapter I - Introduction.....</b>                 | <b>1</b>  |
| <b>1.1. Motivation and Background</b>                   | <b>1</b>  |
| 1.1.1. Available Lymph Nodes Imaging Modalities .....   | 1         |
| 1.1.2. Medical Microwave Imaging .....                  | 2         |
| <b>1.2. Objectives</b>                                  | <b>3</b>  |
| <b>1.3. Contributions</b>                               | <b>4</b>  |
| <b>1.4. Dissertation Overview</b>                       | <b>4</b>  |
| <b>1.5. Chapter conclusions</b>                         | <b>5</b>  |
| <b>2. Chapter II – Literature Review .....</b>          | <b>6</b>  |
| <b>2.1. Anatomical Background</b>                       | <b>6</b>  |
| 2.1.1. Head and Neck Anatomy.....                       | 6         |
| 2.1.2. Head and Neck Lymphatic System.....              | 9         |
| 2.1.3. Head and Neck Cancer .....                       | 11        |
| <b>2.2. Phantom Studies</b>                             | <b>13</b> |
| <b>2.3. Phantom Development</b>                         | <b>15</b> |
| 2.3.1. Filtering Techniques .....                       | 15        |
| 2.3.2. Unsupervised Clustering Techniques.....          | 17        |
| 2.3.3. Clustering Quality.....                          | 20        |
| <b>2.4. Head and Neck Modelling</b>                     | <b>22</b> |
| 2.4.1. Dielectric Properties .....                      | 22        |
| 2.4.2. Dielectric Properties of biological tissues..... | 23        |
| 2.4.3. Finite-Difference Time-Domain Method.....        | 23        |
| <b>2.5. Chapter Conclusions</b>                         | <b>24</b> |
| <b>3. Chapter III – 3D Numerical Models .....</b>       | <b>25</b> |
| <b>3.1. Materials</b>                                   | <b>25</b> |
| <b>3.2. Methodology</b>                                 | <b>25</b> |
| <b>3.3. Results and Discussion</b>                      | <b>28</b> |
| 3.3.1. Numerical Phantom Generator .....                | 29        |
| <b>3.4. Chapter Conclusions</b>                         | <b>31</b> |
| <b>4. Chapter IV – 3D Anthropomorphic Models .....</b>  | <b>32</b> |

|  |           |
|--|-----------|
| <b>4.1. Materials</b>                                  | <b>32</b> |
| <b>4.2. Methodology</b>                                | <b>33</b> |
| 4.2.1. Step 1 - MRI Data Selection .....               | 34        |
| 4.2.2. Step 2 - Data Cleaning .....                    | 34        |
| 4.2.3. Step 3 - Unsupervised Clustering .....          | 37        |
| 4.2.4. Step 4 – Synthetic Tissues Insertion .....      | 39        |
| 4.2.5. Step 5 – Dielectric Properties Assignment ..... | 39        |
| 4.2.6. Methodology Overview .....                      | 41        |
| <b>4.3. Results and Discussion</b>                     | <b>42</b> |
| 4.3.1. Step 1 - MRI Data Selection .....               | 42        |
| 4.3.2. Step 2 – Data Cleaning .....                    | 44        |
| 4.3.3. Step 3 - Unsupervised Clustering .....          | 48        |
| 4.3.4. Step 4 – Synthetic Tissues Insertion .....      | 57        |
| 4.3.5. Step 5 - Dielectric Properties Assignment ..... | 58        |
| 4.3.6. Development of the Anthropomorphic Model .....  | 58        |
| 4.3.7. 3D Anthropomorphic Phantom Generator .....      | 62        |
| <b>4.4. Chapter Conclusions</b>                        | <b>64</b> |
| <b>5. Chapter V – Conclusions and Future work.....</b> | <b>66</b> |
| <b>References .....</b>                                | <b>68</b> |
| <b>Appendix A.....</b>                                 | <b>78</b> |
| <b>Appendix B.....</b>                                 | <b>79</b> |
| <b>Appendix C .....</b>                                | <b>85</b> |

# List of Figures

|  |    |
|--|----|
| <b>Figure 2. 1:</b> Division of the neck into anterior and posterior cervical triangles by the sternocleidomastoid muscle. Highlight of some clinically important landmarks as the hyoid bone and thyroid cartilage [31].  | 8  |
| <b>Figure 2. 2:</b> Sagittal section of the upper aerodigestive tract [51].  | 9  |
| <b>Figure 2. 3:</b> Lymph node representation demonstrating the pathways of lymph into and out of the node. (From [31]).   | 10 |
| <b>Figure 2. 4:</b> Representation of the location of cervical lymph nodes in levels I-VI in relation to the head and neck. (From [31]).   | 11 |
|  |    |
| <b>Figure 3. 1:</b> Schematics of the nomenclature used for the coordinates above; coronal plane at top left and sagittal plane at top right. The values in cm used to model the head and neck are presented below. (Adapted from [29]).   | 26 |
| <b>Figure 3. 2:</b> Representation of the central coronal slice of the developed phantom, which includes the skin tissue, adipose tissue, muscle tissue, bone tissue, and mixed tissue.  | 27 |
| <b>Figure 3. 3:</b> a) Representation of a model which includes all the previously discussed tissues such as skin, muscle, fat, bone and mixed tissue and LNs, both healthy and diseased. b) “Zoom in” of the representation above in order to better visualise the different tissues type of each lymph node.   | 28 |
| <b>Figure 3. 4:</b> Interface which allows the user to add subcutaneous adipose tissue to the phantom.   | 29 |
| <b>Figure 3. 5:</b> Interface which allows the user to add muscular tissue to the phantom.   | 29 |
| <b>Figure 3. 6:</b> Interface which allows the user to add bone tissue to the phantom.   | 29 |
| <b>Figure 3. 7:</b> Interface which allows the user to add mixed tissue to the phantom.  | 29 |
| <b>Figure 3. 8:</b> Interface which allows the user to choose the variability of the dielectric properties of the tissues included into the mixed tissue type.   | 29 |
| <b>Figure 3. 9:</b> Interface which allows the user to add skin tissue to the phantom.   | 29 |
| <b>Figure 3. 10:</b> Interface which allows the user to add lymph nodes to the phantom.  | 30 |
| <b>Figure 3. 11:</b> Interface which allows the user to add the number of lymph nodes to the phantom.  | 30 |
| <b>Figure 3. 12:</b> Informative note which specifies the frontiers of the six different levels of the lymph nodes.  | 30 |
| <b>Figure 3. 13:</b> Interface which allows the user to choose the size, location and state of a lymph node.   | 30 |
| <b>Figure 3. 14:</b> Interface which allows the user to choose whether he/she wants to specify the location of the LNs or if he/she prefers the phantom generator to automatically assign positions to the LNs.  | 30 |
| <b>Figure 3. 15:</b> Interface which allows the user to save the designed model of the head and neck in a .mat file.   | 30 |
|  |    |
| <b>Figure 4. 1:</b> Dielectric properties curves considered to assign the dielectric properties to the tissues in the cervical region, which are represented in the developed models and phantom generator. The graph on the left depicts the permittivity curves, and the graph on the right shows the conductivity curves, for the considered biological tissues. Both curves were obtained by using the 4-Cole-Cole formulation with the parameters given in [118]. | 40 |
| <b>Figure 4. 2:</b> Dielectric properties curves considered to assign the dielectric properties to the LNs which are inserted in the developed models. The graph on the left depicts the permittivity curves, and the graph  |    |



|   |    |
|---|----|
| on the right shows the conductivity curves, for the healthy and unhealthy cross-section and surface of the LNs. Both curves were obtained by using the 4-Cole-Cole formulation with the Debye parameters given by [119]. The missing 4-Cole-Cole parameters were assumed to be null. ....   | 41 |
| <b>Figure 4. 3:</b> Illustration of the methodology steps followed during this dissertation. ....   | 42 |
| <b>Figure 4. 4:</b> Scans of patients 5 and 4, on the left and right, respectively. In both figures, the axial plane of the cricoid cartilage was considered, for comparison purposes. ....   | 43 |
| <b>Figure 4. 5:</b> Axial slice of the normalised MRI exam after background subtraction is represented at the top left. Results obtained (the same axial slice is shown) after applying the median filter and a 2D K-means segmentation of the axial slice (bottom left), 3D K-means segmentation of the original-shaped voxels (top right) and the 3D K-means segmentation of pseudo-cubic transformed voxels (bottom right). The right sternocleidomastoid muscle is located within the black circles and the red circles indicates areas with small-sized granularities.....   | 45 |
| <b>Figure 4. 6:</b> Axial slice of the normalised MRI exam after background subtraction is represented at the top left. Results obtained (the same axial slice is shown) after applying the Gaussian LP filter and a 2D K-means segmentation of axial slices (bottom left), 3D K-means segmentation of the original-shaped voxels (top right) and 3D K-means segmentation of the pseudo-cubic transformed voxels (bottom right). The right sternocleidomastoid muscle is located within the black circles and the red circles indicates areas with small-sized granularities..... | 45 |
| <b>Figure 4. 7:</b> Axial slice of the normalised MRI exam after background subtraction is represented at the top left. Results obtained (the same axial slice is shown) after applying the Butterworth LP Filter ( $n=2$ ) and a 2D K-means segmentation of axial slices (bottom left), 3D K-means segmentation of the original-shaped voxels (top right) and 3D K-means segmentation of the pseudo-cubic transformed voxels (bottom right). The right sternocleidomastoid muscle is located within the black circles. ....  | 46 |
| <b>Figure 4. 8:</b> Axial slice of the normalised MRI exam after background subtraction is represented at the top left. Results obtained (shown in the same axial slice) after applying the ideal LP filter and a 2D K-means segmentation of axial slices (bottom left), 3D K-means segmentation of the original-shaped voxels (top right) and 3D K-means segmentation of the pseudo-cubic transformed voxels (bottom right). The right sternocleidomastoid muscle is located within the black circles. ....  | 46 |
| <b>Figure 4. 9:</b> Results of the filtering test with Option B – the combination of the best filters yielding from Option A. Application of the Gaussian and median filters alone, and the combination of the Gaussian filter followed by the median and the median filter followed by the Gaussian filter, from left to right and top to bottom, respectively. The black circles indicate regions with small-sized granularities. ....  | 48 |
| <b>Figure 4. 10:</b> DBSCAN clustering results of a slice of the 3D MRI data: 6 and 162 clusters, from left to right. ....  | 49 |
| <b>Figure 4. 11:</b> Histogram of the gray levels of MRI data after normalisation and background subtraction. ....  | 50 |
| <b>Figure 4. 12:</b> Segmented image ( $k = 7$ ) after the application of the BIRCH clustering algorithm, on the left. Final image ( $k = 4$ ) resulting from the manual combination of clusters that likely represent the same tissue type, on the right.....  | 51 |
| <b>Figure 4. 13:</b> Segmented image ( $k = 10$ ) after the application of the BIRCH clustering algorithm, on the left. Final image ( $k = 5$ ) resulting from the manual combination of clusters that represent the same tissue type, on the right.....  | 51 |
| <b>Figure 4. 14:</b> Segmented images after the application of the agglomerative hierarchical clustering algorithm, with different $k$ numbers of cluster. a) $k = 4$ , b) $k = 5$ , c) $k = 6$ and d) $k = 7$ . ....   | 52 |
| <b>Figure 4. 15:</b> Segmented images after the application of the K-means clustering algorithm, with different $k$ numbers of cluster. a) $k=4$ , b) $k=5$ , c) $k=6$ , and d) $k=7$ .....   | 55 |

|   |           |
|---|-----------|
| <b>Figure 4. 16:</b> Segmented images after the application of the K-means clustering algorithm, with $k=5$ , on the left column, and $k=6$ on the right. Several slices were studied, $z = 10, 20$ and $30$ , from top to bottom, respectively. ....                             | <b>56</b> |
| <b>Figure 4. 17:</b> Final data processing pipeline used to build realistic models of the head and neck region. ....  | <b>57</b> |
| <b>Figure 4. 18:</b> Skin insertion algorithm created from the binary mask on the left; the blue line is the skin layer around the body. Results of the application of the LNs insertion algorithm on the right; healthy LN represented in red and metastasised LN in brown. .... | <b>57</b> |
| <b>Figure 4. 19:</b> Segmented image resulting from the application of the final data processing pipeline to the MRI exam, on the left. Final image after the merger of clusters, on the right. The black circles mark bone tissue (a vertebra). ....                             | <b>58</b> |
| <b>Figure 4. 20:</b> Pipeline with the methodology of the combination process of MRI images of patient 5 acquired using different sequences, and the results obtained at step 1, 2, and 3. ....   | <b>60</b> |
| <b>Figure 4. 21:</b> Interface which allows the user to add subcutaneous adipose tissue to the realistic phantom. ....  | <b>63</b> |
| <b>Figure 4. 22:</b> Interface which allows the user to add skin tissue to the realistic phantom. ....  | <b>63</b> |
| <b>Figure 4. 23:</b> Interface which allows the user to add muscular tissue to the realistic phantom. ....  | <b>63</b> |
| <b>Figure 4. 24:</b> Interface which allows the user to add lymph nodes to the realistic phantom. ....  | <b>63</b> |
| <b>Figure 4. 25:</b> Interface which allows the user to add the number of lymph nodes to the realistic phantom. ....  | <b>63</b> |
| <b>Figure 4. 26:</b> Informative note which specifies the frontiers of the six different levels of the lymph nodes ....   | <b>63</b> |
| <b>Figure 4. 27:</b> Interface which allows the user to choose the size, location and state of a lymph node. ....   | <b>63</b> |
| <b>Figure 4. 28:</b> Interface which allows the user to choose the frequency value at which the algorithm should interpolate the dielectric properties values of the biological tissues. ....   | <b>63</b> |
| <b>Figure 4. 29:</b> Interface which allows the user to choose whether he/she wants to specify the location of the LNs or if he/she prefers the phantom generator to automatically assign positions to the LNs. ....  | <b>64</b> |
| <b>Figure 4. 30:</b> Interface which allows the user to save the phantom. ....  | <b>64</b> |

# List of Tables

|  |    |
|--|----|
| <b>Table 2. 1:</b> Mean value of external anthropometry of the head and neck and strength variables, for male and female subjects (adapted from [29]).   | 7  |
| <b>Table 2. 2:</b> TNM Staging for the Larynx, Oropharynx, Hypopharynx, Oral Cavity, Salivary Glands, and Paranasal Sinuses (adapted from [54]). Tis, T1, T2, T3, T4a and T4b correspond to carcinoma in situ, tumour with 2 cm or less in greatest dimension, tumour greater than 2 cm but no more than 4 cm in greatest dimension, tumour with more than 4 cm, moderately advanced local disease and greatly advanced local disease, respectively. N0, N1 and N2 refer to no regional node metastasis, metastasis in a single ipsilateral LN with 3 cm or less in greatest dimension, and metastasis in a single ipsilateral LN with more than 3 cm and less than 6 cm in greatest dimension or in multiple ipsilateral LNs, none more than 6 cm in greatest dimension, respectively. M0 and M1 refer to no distant metastasis and distant metastasis, respectively. | 13 |
| <b>Table 4. 1:</b> MRI TCGA-HNSC dataset.  | 33 |
| <b>Table 4. 2:</b> Values of the silhouette coefficient calculated for each segmented image obtained from Agglomerative Hierarchical clustering with varying k number of clusters from 4 to 7.   | 53 |
| <b>Table 4. 3:</b> Values of the silhouette coefficient, and Davies-Bouldin and Calinski-Harabasz indexes calculated for each segmented image from scenario a) to d), obtained from Agglomerative Hierarchical clustering with varying k number of clusters from 4 to 7, respectively. The value of each metric corresponding to the best clustering according to each clustering evaluation method, is highlighted.   | 53 |
| <b>Table 4. 4:</b> Values of the silhouette coefficient, and Davies-Bouldin and Calinski-Harabasz indexes calculated for each segmented image from scenario a) to d), obtained from Agglomerative Hierarchical clustering with varying k number of clusters from 4 to 7, respectively. The value of each metric corresponding to the best clustering according to each clustering evaluation method, is highlighted.   | 55 |
| <b>Table 4. 5:</b> Results from the combination of clusters by means of addition. The numbers in the rows and columns correspond to the cluster numbers from the segmented T1- and T2-weighted images.   | 61 |
| <b>Table 4. 6:</b> Results from the combination of clusters by means of multiplication. The numbers in the rows and columns correspond to the cluster numbers from the segmented T1- and T2-weighted images.   | 61 |

# Acronyms

|             |  |
|-------------|--|
| 2D          | Two-Dimensional  |
| 3D          | Three-Dimensional  |
| ALN         | Axillary Lymph Node  |
| BIRCH       | Balanced Iterative Reducing and Clustering using Hierarchies |
| CFT         | Characteristic Feature Tree                                  |
| CHI         | Calinski-Harabasz Index                                      |
| CLN         | Cervical Lymph Node  |
| CSF         | CerebroSpinal Fluid  |
| CT          | Computed Tomography  |
| DBI         | Davies-Bouldin Index   |
| DBSCAN      | Density-Based Spatial Clustering of Applications with Noise  |
| DICOM       | Digital Imaging and Communications in Medicine               |
| DM          | Data Mining  |
| DNA         | DeoxyriboNucleic Acid  |
| EIS         | Electrical Impedance Spectroscopy                            |
| FT          | Fourier Transform  |
| HPV         | Human Papilloma Virus  |
| LN          | Lymph Node   |
| LP          | Low Pass   |
| ML          | Machine Learning   |
| MRI         | Magnetic Resonance Imaging                                   |
| MWI         | MicroWave Imaging  |
| PET         | Positron Emission Tomography                                 |
| SPAIR       | SPectral Attenuation Inversion Recovery                      |
| STIR        | Short T1 Inversion Recovery                                  |
| TCIA        | The Cancer Imaging Archive                                   |
| TCGA - HNSC | The Cancer Genome Atlas Head-Neck Squamous Cell Carcinoma    |
| TMM         | Tissue Mimicking Material                                    |
| TSE         | Turbo Spin-Echo  |
| UWB         | Ultra-WideBand   |

# Chapter I - Introduction

## 1.1. Motivation and Background

Head and neck cancer is a broad term referring to any epithelial malignancies arising in the paranasal sinuses, nasal and oral cavity, salivary glands, pharynx, and larynx. This type of cancer reported 887,659 worldwide new cases in 2018, with over 51% death incidence [1]. In up to 80% of these cancer cases, cancer cells metastasised through lymphatic and blood vessels [2] [3].

Currently there is no satisfactory neoadjuvant (i.e. pre-operative) diagnosis to assess whether cancer has spread to neighbouring LNs. The assessment of LNs within the head and neck region, also referred to as Cervical LNs (CLNs), often requires their surgical removal and subsequent histopathology. This practice frequently results in the removal of healthy CLNs, which ultimately has negative impact on the patient's health and quality of life, and also on the economy of a country, due to the high costs of surgeries and follow-up therapies supported by healthcare systems [4] [5].

When CLN excision is performed certain repercussions are expected. The patients' physical recovery often becomes a slower process, the speech and swallowing may be hampered, and the physical appearance is oftentimes deformed. In addition, the removal of healthy CLNs increases the risk of infection and lymphedema [6] [7] [8]. The extraction of too many lymph nodes causes patients to lose the capability to drain lymph into the lymphatic system, requiring continuous monitoring and treatment in case of infection or allergic reactions. Hence, they need to regularly undergo specific treatments, such as Manual Lymphatic Drainage or Lymphatic Drainage, with specific equipment in physiotherapy sessions, and take special care when travelling or doing certain sports.

If CLNs could be accurately diagnosed with a non-invasive approach ahead of surgery, the quality of life of cancer patients and survivors could potentially be significantly improved and the burden on patients and on healthcare systems reduced [6] [9].

### 1.1.1. Available Lymph Nodes Imaging Modalities

The modalities to image CNLs are divided into two main branches: the first one provides anatomic information, which is the category where the conventional diagnosis methodologies fall into, and the second one, the more recent one, gathers information about the molecular nature of a tumour. While anatomical imaging concerns the detection of the lesion and its extension, biological imaging focuses on studying the behaviour of the tumour and its response to chemoradiation [10].

In order to identify the status of the cancer and decide the measures to be taken as a response, physicians evaluate the LNs closest to the primary site of the tumour, which are the ones with highest probability of being targeted by cancer cells. These first LNs are also known as Sentinel Lymph Nodes.

Neck dissection is the standard procedure to assess whether the cancer cells have spread to neighbouring tissues. Despite being a highly accurate method, it is invasive which may cause discomfort to the patient, some bruising and soreness in the area where the sample was taken from, it can also be painful, and entail a significant risk of infection [4] [6].

Other golden-standard techniques for LN imaging include ultrasound, Computed Tomography (CT), Positron Emission Tomography (PET), and Magnetic Resonance Imaging (MRI). Ultrasound is the *de facto* imaging modality to diagnose head and neck tumours, but neoadjuvant diagnosis of CLNs was proven non-conclusive unless the high frequency waves used to identify possible metastatic LNs were combined with fine-needle aspiration cytology to assess if there is abnormality in the sample tissue. [11] This procedure has reported sensitivity and specificity as high as 98% and 95%, respectively [8]. Visual inspection and palpation may also help locate swollen CLNs. Regardless its advantages, ultrasound is highly dependent on the operator who must be well experienced and have great anatomical knowledge of the area under test, therefore the human error cannot be neglected.

CT has reportedly been used for CLN diagnosis because of its availability, lower cost and fast scan times, but cannot reliably detect CLNs smaller than 5 mm [8]. Besides, CT uses ionizing radiation. MRI also has been universally accepted as a tool for head and neck cancer staging; due to its better tissue contrast, MRI is sometimes preferred over CT depending on the location and extent of the tumour. Conversely, MRI is also prone to motion and swallowing-related artifacts [12].

PET scanning with  $^{18}\text{F}$ -Fluoro-2-DeoxyGlucose (FDG) is a widely used imaging modality which allows the identification of nodal and distant metastasis by highlighting increased metabolic activities with radiotracer in those areas and thus, critical in evaluation of advanced stage cancers [13]. Combined PET and CT scans were proven more accurate than either modality alone in identifying malignant lesions in the head and neck region [14]. Besides, PET/CT scanning is also valuable in radiation therapy planning, and in recurrent lesions monitoring and treatment [15]. However, nuclear medicine techniques are not the chosen modalities for CLN imaging because of the high costs and the exposure to radioactive materials.

Other imaging modalities, such as Electrical Impedance Spectroscopy (EIS) [16], have reported initial promising CLN diagnosis (of previously located CLNs) but these are not widely available nor used.

### **1.1.2. Medical Microwave Imaging**

As a result of the lack of alternatives to assess CLNs, MicroWave Imaging (MWI) presents itself as an interesting option. Even though it uses non-ionizing radiation ranging from 3 to 300 GHz, which corresponds to wavelengths varying between 10 cm to 1 mm [17], radiation with such characteristics suffers significant attenuation in biological tissues, which limits the depth of screening and the resolution of image. Hence, it is only suited for mass screening of shallow body regions (depth up to ~6 cm).

Medical MWI uses signals based on the dielectric contrast between different tissues, propagating through the body to visualise internal structures. This is founded on the premise that tissues with different dielectric properties generate electromagnetic scatterings when radiated with microwaves. The scattering of the incident wave alters the energy detected at the receivers and the transmitters, which are used to form maps of the electrical property distributions in the body. Microwave images for medical applications can be created using two approaches: tomography, if the shape of the target and the distribution of the permittivity are acquired from the incident and scattered fields, and radar-based technology if only the reflections from the object are used [18]. The focus of this dissertation is on the radar-based imaging method.

Radar MWI operates by illuminating an anatomical region of interest (or models mimicking that region) with an Ultra-WideBand (UWB) pulse, and recording and processing the resulting backscattered signals. Medical radar MWI systems typically comprise: UWB antennas, transmit/receive electronics, and dedicated skin artefact removal and beamforming algorithms. Skin artefact removal algorithms

remove the large reflection produced by the skin surface; beamforming focuses the backscattered signals so that signals from high scattering regions (e.g. tumour tissues) are combined coherently and signals from clutter are combined incoherently; finally resulting in an image which shows the dielectric scatterers [19] [20]. Instead of creating anatomical images of the body, radar-based MWI creates a map of microwave scattering obtained from transmission and receiving of short electromagnetic pulses, which translates in a map of the dielectric properties of the irradiated area. Here, the abnormalities in the tissues are easily detected and quantified [21]. In addition to being a comfortable and non-invasive imaging modality, it is also portable, low-cost, user-independent, and uses low-power.

MWI has gained significant momentum in the past few years with numerous research projects, patient studies [19] [20] and clinical trials [22] [23], and new products being brought to market (e.g. MARIA<sup>TM</sup> [24]), mostly in the area of breast cancer and stroke detection. Although MWI technology has matured considerably for some clinical applications, performance improvements are required to make clinical usage feasible.

## 1.2. Objectives

The main objective of this dissertation is to use Machine Learning (ML) techniques to create anatomically realistic phantoms which can be later used to develop medical MWI systems for screening and diagnosis, as there is a significant diagnostic blind-spot regarding mass screening of lymph nodes in the case of head and neck cancers.

As screening CLNs using a microwave UWB radar technology has never been attempted before, the first goal (I) of this project comprises modelling the head and neck region according to its anatomy, with special attention to tissue architecture and distribution. This includes:

(I.1) developing two-dimensional (2D) numerical phantoms inspired by some preliminary state-of-the-art 2D breast models published in [25] [26] [27];

(I.2) developing three-dimensional (3D) numerical phantoms with different levels of complexity based on the developed 2D phantoms, which included skin, fat, bone and muscle tissues and CLNs.

The second goal (II) consists of developing 3D anatomically realistic MRI-derived phantoms of the head and neck region, using state-of-the-art segmentation algorithms and realistic dielectric properties of biological tissues. The procedure of building these phantoms will include a thorough study of:

(II.1) data cleaning techniques to enhance MRI image quality (data normalisation, background subtraction, linear and non-linear filtering);

(II.2) Data Mining (DM) clustering techniques such as K-means, Agglomerative Hierarchical, BIRCH and DBSCAN for data segmentation;

(II.3) metrics such as Silhouette Coefficient, Davies-Bouldin and Calinski-Harabasz indexes, used for clustering evaluation and algorithm selection purposes.

(II.4) the assignment of the dielectric properties of the biological tissues to the phantoms using the 4-pole-Cole-Cole model, and a strategy of piecewise-linear mapping.

### 1.3. Contributions

While working on this dissertation, I have adapted an existing “building-block” 2D numerical model of the breast region to operate in the head and neck region. I have also developed from scratch a 3D numerical phantom generator for the head and neck region, using MATLAB®. Furthermore, an MRI-derived 3D anthropomorphic phantom generator for the head and neck region was also adapted from an existing phantom generator used for the breast, previously developed within this research group.

During this period of time, a collaboration with the Instituto de Telecomunicações (IT) of the Instituto Superior Técnico (IST) has included the creation of a 3D printed brain model for imaging tests. The model consisted of three different anatomically realistic hollow compartments designed to mimic the shape of the white and gray matter, the cerebellum and a blood clot, which could be latter filled with fluids that mimicked the properties of these structures. These will be printed in Instituto de Biofísica e Engenharia Biomédica (IBEB) early in 2020.

In addition, I have also presented a poster regarding part of the work developed in this dissertation at the 11<sup>th</sup> Workshop on Biomedical Engineering (WBME) in April 2019 – Appendix A – and submitted a paper for the Best Student Paper Award to the 13<sup>th</sup> Congress of the URSI Portuguese Committee – “Espaço: Desafios e Oportunidades”, Lisbon, Portugal which was presented in December 2019. I also submitted the following conference paper: A.C. Pelicano, R.C. Conceição, “Head and Neck Numerical Phantom Development for Cervical Lymph Node Microwave Imaging” in Appendix B, which was accepted in EuCAP 2020 in convened session CS60 Sensors and Systems for Microwave Biomedical Imaging and Sensing, Copenhagen, Denmark – paper by invitation.

### 1.4. Dissertation Overview

The remainder of this dissertation is organized as follows. A background literature review of the head and neck region is presented in Chapter II. It includes reviews of the head and neck anatomy, a description of the lymphatic system of this region, and finally a subchapter dedicated to head and neck cancer, its formation and currently used staging system. A review of phantom development topics is also given in Chapter II. It is specially focused on filtering techniques for data cleaning and unsupervised clustering methods for data segmentation of MRI images. Some head and neck modelling topics were also addressed in this chapter. Such topics include studies regarding the measurements of the dielectric properties of biological tissues, the formulations which describe the behaviour of dielectric properties of biological tissues over a frequency range and the studies of both numerical and realistic phantoms developed to test MWI systems.

Chapter III details the 3D numerical phantom generator. The relevant materials and methodologies used in the construction of the generator as well as the generator itself and its different levels of complexity are discussed within this chapter.

Chapter IV comprises the methodology and materials used to develop a 3D anthropomorphic model. It also includes a step-by-step decision-making process regarding the construction of the 3D MRI-based phantom generator.

The overall conclusions as well as identified limitations and suggestions for future work, are discussed in Chapter V.



## **1.5. Chapter conclusions**

In this chapter I have shown, how to this day, the available imaging modalities used to diagnose CLNs present several drawbacks that not only compromise the patients' health and quality of life, but also have a negative impact on healthcare systems.

Due to its characteristics, MWI appears to be a possible solution for this problem since it can be widely adopted for mass screening of shallow body regions. Furthermore, LNs within the head and neck are a prime target for this methodology both because of their shallow location and dielectric properties.

It is then of crucial and timely importance to develop anthropomorphic head and neck models to develop novel imaging techniques, such as MWI, which have the potential to correctly diagnose CLNs in a neoadjuvant and non-invasive manner. The successful detection and removal of metastatic CLNs will prevent tumour cells entering the blood system and metastasising to other parts of the body.

# Chapter II – Literature Review

In the interest of understanding all the concepts and assumptions used in the course of this work, a background overview of several topics is provided in this chapter. The present chapter is divided in four main topics. The anatomical background starts with a comprehensive review regarding head and neck anatomy and lymphatic system network followed by an overview of head and neck cancer, including tumour formation and currently used staging system. The phantom studies section revises the existing numerical and physical models developed to mimic regions of the human body, especially in the head and neck region. Additionally, the phantom development section includes an overview of the filtering techniques and unsupervised clustering methods required to extract anatomical knowledge from MRI exams. Finally, head and neck modelling section includes an overview of studies regarding the dielectric properties of the tissues under study, and a summary of the methods which can be used to describe the behaviour of the dielectric properties of such tissues for varying microwave frequencies.

## 2.1. Anatomical Background

The head and neck regions of the human body are extremely complex and highly specialized. The present section aims at summarizing the most important concepts within the scope of this dissertation.

### 2.1.1. Head and Neck Anatomy

The human head is commonly divided into two separate regions: cranium and face. Along with the brain, four of the five sensorial organs are located within this part of the human body, such as the eyes, ears, nose and taste buds. The main functionality of the human head is the protection of the brain, which is an extremely vulnerable organ responsible for controlling most of the body systems [28]. The geometry of the human head was addressed in a study conducted by Vasavada et al [29]. They showed that human female and male heads are not geometrically similar, and the most prominent differences were observed in width, depth, and height rather than the size of its circumference. Conversely, in the case of the neck, the most significant difference in terms of gender concerns the circumference diameter (see Table 2.1).

The neck, also referred to as cervical region, is responsible for supporting the weight of the head and allowing its movement. This region of highly compact tissues contains extremely vulnerable structures, such as arteries, veins, nerves and important glands [28]. It extends from the pericraniocervical line to the level of the clavicle. Usually, the neck is divided into two main triangles by the sternocleidomastoid muscle which obliquely transects it. Accordingly, the anterior and the posterior cervical triangles are created. The first has its apex directed inferiorly and is limited superiorly by the inferior border of the mandible, anteriorly by the median line of the neck, and posteriorly by the sternocleidomastoid muscle. Similarly, the posterior cervical triangle has its apex directed superiorly, the sternocleidomastoid muscle as the anterior and lateral borders, the trapezius muscle as the posterior frontier, and the base located at the clavicle level [30] (see Figure 2.1). These two triangles can be further

subdivided into six smaller triangles [28]. The cervical region of the human body consists of two main cervical muscles, the sternocleidomastoid muscle and the trapezius muscle, bones such as seven cervical vertebrae and the hyoid bone, and cartilages of pharynx and larynx [30].

Table 2. 1: Mean value of external anthropometry of the head and neck and strength variables, for male and female subjects (adapted from [29]).

|   | Male        | Female      |
|---|-------------|-------------|
| <b>General</b>                                      |             |             |
| Age (years)   | 25.8 ± 5.3  | 21.6 ± 3.0  |
| Height (cm)   | 169 ± 3     | 169 ± 3     |
| Weight (kg)   | 74 ± 9      | 66 ± 9      |
| <b>Head</b>   |             |             |
| Circumference (mm)                                  | 577 ± 13    | 562 ± 15    |
| Width (mm)  | 153 ± 8     | 148 ± 8     |
| Depth (mm)  | 199 ± 8     | 190 ± 6     |
| Height (mm)   | 197 ± 15    | 184 ± 8     |
| <b>Neck</b>   |             |             |
| Length (C7) (mm)                                    | 108 ± 5     | 107 ± 5     |
| Length (sternum) (mm)                               | 175 ± 13    | 174 ± 8     |
| Circumference (mm)                                  | 394 ± 22    | 331 ± 20    |
| Width (mm)  | 117 ± 11    | 106 ± 7     |
| Depth (mm)  | 123 ± 7     | 103 ± 5     |
| Width/depth (mm)                                    | 0.95 ± 0.07 | 1.03 ± 0.07 |
| Length/circumference                                | 0.27 ± 0.02 | 0.32 ± 0.02 |
| Head Circ <sup>3</sup> /Neck Circ <sup>2</sup> (mm) | 125 ± 13    | 164 ± 21    |
| <b>Strength</b>                                     |             |             |
| Flex (N)  | 149 ± 44    | 82 ± 26     |
| cFlex (N)   | 197 ± 44    | 127 ± 25    |
| Ext (N)   | 244 ± 69    | 173 ± 31    |
| cExt (N)  | 292 ± 69    | 219 ± 32    |

Head and neck cancer sites comprise the oral and nasal cavities, paranasal sinuses, salivary glands, pharynx and larynx (see Figure 2.2). A more detailed description of such structures is presented below.

- **Oral cavity:** located within the head region, consists of cheeks, lips, hard palate and soft palate. The opening of the oral cavity is referred to as the oral orifice. This cavity is limited anteriorly by the lips and posteriorly by the pharynx. Laterally, the border is limited by the cheeks of the face, and superiorly and inferiorly limited by the frontiers of the oral cavity are the palate and the floor of the mouth, respectively [31].
- **Nasal cavity:** irregular space located between the roof of the mouth and the base of the cranium. It consists of two chambers formed by cranial and facial bones, separated sagittally by an osseocartilaginous septum. The nasal cavity serves as a communication gateway between the paranasal sinuses and the nasopharynx [30].
- **Paranasal sinuses:** consist of four sets of air spaces housed within certain bones of the skull surrounding the nasal area. Each sinus communicates via drainage ducts into the nasal cavity. Their function is not well-known although some think they help warm and moisten the inhaled air, lighten the skull bones, act as sound resonators, and provide mucus for the nasal cavity [31].

- Salivary glands:** divided into major and minor glands according to their size. There are numerous minor glands located within the palatal region, however the major ones lie outside the oral cavity. The major salivary glands include the parotid, submandibular, and sublingual glands. Regardless of their size, they have the same purpose: produce saliva, which is drained directly into the oral cavity to lubricate, clean and help in digestion. The parotid gland is the largest of the salivary glands, albeit it only produces approximately 25% of the total salivary volume. The gland extends from each ear, along the zygomatic arch and inferior to the mandible. The duct associated with the parotid salivary gland is the Stensen duct. The submandibular salivary gland is the second largest major salivary gland which lies inferiorly and posteriorly to the base of the tongue. It is responsible for the production of 60% to 65% of total salivary volume. The saliva produced by these salivary glands is drained into the oral cavity through the Wharton ducts, which open directly into the oral cavity in the sublingual caruncle, on each side of the lingual frenum. Finally, the third salivary gland is the sublingual gland located under the mucous membrane of the floor of the mouth and anterior to the submandibular gland. This gland contributes with 10% of the total salivary volume. The Bartholin ducts, which are main ducts responsible for draining the saliva from the sublingual glands to the oral cavity, open at the sublingual caruncle as the ducts of the submandibular glands. In addition, several small other ducts that open in an area posterior to the sublingual caruncle are called ducts of Rivinus [28] [31].

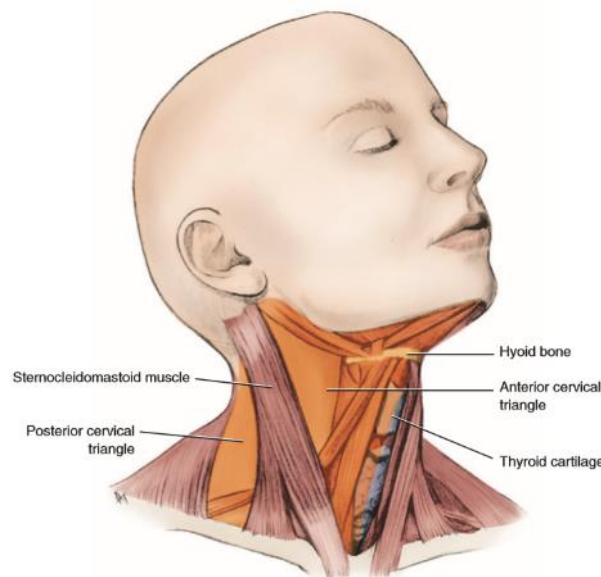


Figure 2. 1: Division of the neck into anterior and posterior cervical triangles by the sternocleidomastoid muscle. Highlight of some clinically important landmarks as the hyoid bone and thyroid cartilage [31].

- Pharynx:** inverted cone-shaped organ, 12–14 cm long which extends from the cranial base to the lower border of the cricoid cartilage. This organ connects with the nasal and oral cavities via the nasopharynx and oropharynx, respectively. Also, the pharynx continues to the larynx of the respiratory system, through the laryngopharynx, and to the esophagus of the digestive

system. Accordingly, the nasopharynx is located posterior to the nasal cavity and above the soft palate, the oropharynx is the middle portion of the pharynx between the soft palate and the level of the hyoid bone and finally, the laryngopharynx begins from the level of the hyoid bone and opens into the esophagus and larynx. The hyoid bone is a “U”-shaped bone located in the anterior midline of the neck, superior and anterior to the thyroid cartilage of the larynx and below to the mandible. It has the particularity of not being articulated with any other bones which allows its mobility for mastication, swallowing, and speech [28] [30] [31].

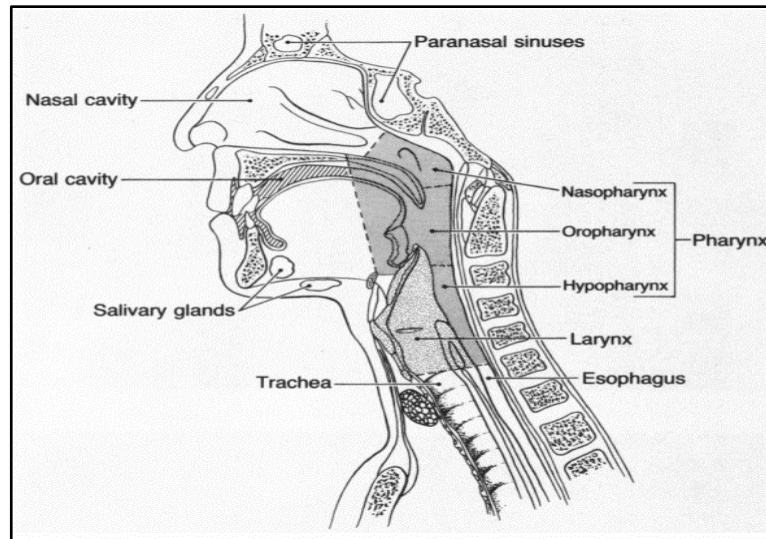


Figure 2. 2: Sagittal section of the upper aerodigestive tract [51].

- **Larynx:** tube which extends from the laryngopharynx to the lower border of the cricoid cartilage, where it continues into the trachea. The main function of the larynx is to prevent food from entering the trachea, allow the passage of air to the lungs and finally, produce sound. It is composed of six paired cartilages and three large and unpaired cartilages. The biggest unpaired cartilage is the thyroid cartilage, also known as “Adam’s apple”, which is more prominent in adult males due to increased levels of masculine hormones [28]. The cricoid cartilage is the only cartilage that forms a complete ring around the trachea and is located below the thyroid cartilage [30].

### 2.1.2. Head and Neck Lymphatic System

The lymphatic system of the human body is composed of vessels, nodes, ducts, and tonsils forming a one-way pathway which transports lymph back to the bloodstream. The lymph is in fact interstitial fluid accumulated in spaces between cells which has entered the lymphatic capillaries instead of returning to blood via vascular capillaries. The smaller lymphatic vessels containing lymph, the lymphatic capillaries, converge into one of the two principal larger lymphatic ducts, the thoracic duct or the right lymphatic duct. In the case of the head and neck region, the thoracic duct drains lymph from the left side of the head and neck to the left subclavian vein, while the right lymphatic duct drains from the right side of the head and neck into the right subclavian vein. When this system does not function

well, the extra interstitial fluid is not properly drained from the tissues and a condition called lymphedema occurs [28].

The lymph is a clear watery fluid which contains proteins, microorganisms and absorbed fats. Besides draining the excessive amount of interstitial fluid to the circulatory system, the lymphatic system is also responsible for transporting absorbed fats and some vitamins from the small intestine to the blood and has an important role in immunological defences against disease processes such as infection and cancer [31]. The tonsils of the lymphatic system are small amounts of lymphoid tissue located near the ear, nose and pharyngeal regions aimed at removing toxins that could begin disease processes [28]. Finally, the lymph nodes are round, oval, or bean-shaped bodies of organized lymphoid tissue enclosed within fibrous connective tissue capsules, surrounded by perinodal adipose tissue. These bodies are grouped in clusters along the lymphatic vessels and are named after the anatomical region they are adjacent to. Depending on their depth from the skin surface, they are classified as superficial if located in the hypodermis or deep lymph nodes. In healthy conditions, the size of the lymph nodes varies between 1 to 25 mm long, they are also soft and mobile in the neighbouring tissues [32].

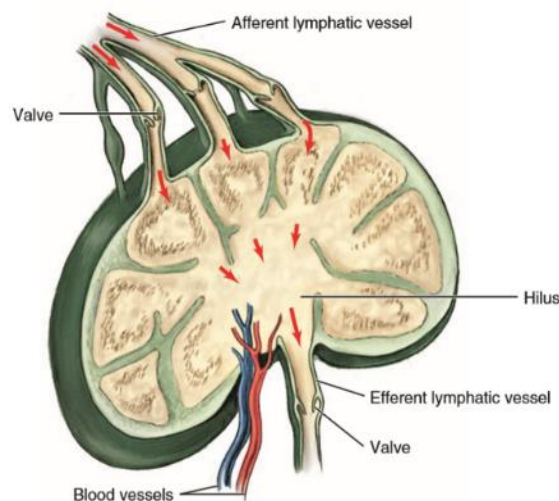


Figure 2. 3: Lymph node representation demonstrating the pathways of lymph into and out of the node. (From [31]).

Lymph nodes contain lymphocytes, white blood cells that remove bacteria and other foreign substances from the fluid. In short, they purify the lymph. Moreover, the lymph nodes are involved in lymphocytes production whenever foreign organisms are found in the lymph, by stimulating cell division of the lymphocytes inside. The lymph flows into the lymph node by a multiple number of afferent lymphatic vessels that enter the subcapsular sinus and is carried out by a single efferent lymphatic vessel, which emerges from the hilus – a depression on one side of the node [28] observed in Figure 2.3)

Throughout the human body approximately 450 lymph nodes were found, with around 70 lymph nodes on head and neck region alone [32]. Clinicians divide them into six levels based both on their location or nearby anatomic structures as well as their depth: (see Figure 2.4)

- **Level I:** located at the chin level, superior to the mandible angle.
- **Level II:** located inferiorly to the mandibular angle, above the hyoid bone and anteriorly/adjacent to the sternocleidomastoid muscle.
- **Level III:** located between the hyoid bone and the thyroid cartilage, adjacent to the sternocleidomastoid muscle.
- **Level IV:** located between the thyroid cartilage and the clavicle, adjacent to the sternocleidomastoid muscle.
- **Level V:** located between the skull base and the clavicle, within the posterior triangle.
- **Level VI:** located anteriorly to the sternocleidomastoid muscle and between the hyoid bone and the top of the manubrium, the uppermost segment of the sternum.

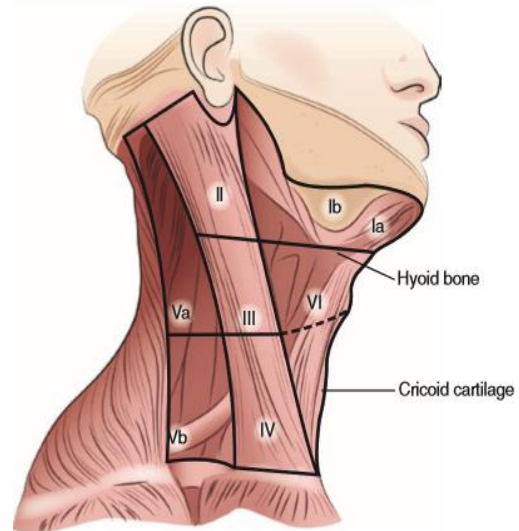


Figure 2. 4: Representation of the location of cervical lymph nodes in levels I-VI in relation to the head and neck. (From [31]).

### 2.1.3. Head and Neck Cancer

Tumour is a generic term for a large group of diseases characterized by abnormal cell growth. It is classified as malignant (*i.e.* cancer) or benign depending on their ability to invade nearby tissues through lymphatic or blood vessels. Once the malignant tumour successfully spreads to other parts of the body it can interfere with the digestive, nervous, and circulatory systems. It may also release hormones that alter body function [33]. Cancer of the head and neck comprise arising cancers in particular regions such as the salivary glands, oral and nasal cavity, pharynx, larynx and paranasal sinuses.

#### 2.1.3.1. Tumour formation

Certain genetic events, such as the activation of proto-oncogenes or the elimination of tumour-suppressor genes, control the development of the disease. Some examples are the inactivation of the p16 gene due to the loss of chromosomal region 9p21, which is frequently observed in patients with head and neck cancer in an early stage of the disease [34] [35]. Mutations on the p53 tumour-suppressor gene are also detected in roughly 50% of all head and neck cancers [36] [37]. And, in about a third of all these tumours, an amplification of 11q13 and overexpression of oncogene cyclin D1 occurs, which is associated with advanced-stage disease and presence of lymph node metastases [38]. Around 90% of head and neck cancers are Squamous Cell Carcinoma of the Head and Neck (SCCHN), for which tobacco and alcohol consumption are the most important risk factors [39] [40]. In these cases, carcinogens present in those substances (*i.e.* tobacco and alcohol) cause genetic mutations of the p53 [41]. Other occupational risk factors include exposure to diesel fumes [42], paint and asbestos; woodworking and metal fabricating occupations [43]. Over the past years, a continuous increase in the incidence of oropharyngeal cancer was observed, despite the decrease of risk behaviours, such as tobacco and alcohol consumption [44] [45]. Investigators indicated the Human Papilloma Virus (HPV)

as a cause of oropharyngeal cancer due to the presence of oncogenic HPV DeoxyriboNucleic Acid (DNA) in more than 50% of epithelial cancers arising in the oropharynx [46] [47] [48]. DNA from Epstein-Barr virus was also found in cancerous tissues from the nasopharyngeal region, thus an association between this virus and nasopharyngeal cancer was established [49].

In an early stage of the disease, the symptoms are only vague and vary according to the location of the primary site; accordingly, dentists and primary care physicians are instructed to perform a thorough analysis of the patients, particularly if they adopt risk behaviours [50]. Sinusitis and unilateral obstruction of the nasal airway are some of the symptoms referred by patients with early stage nasal cavity cancer; in more advanced tumours, facial swelling or pain, exophthalmos and loosening of the molars are mentioned. Regarding oral cavity malignancies, the most common signs pointed out by patients are pain, ulcers that do not heal and changes in the fit of dentures. Within the pharynx, symptoms vary according to the region where tumours arise. Nasal obstruction, epistaxis and serous otitis are some of the frequent symptoms referred by patients with early stage nasopharyngeal cancer; in more advanced cases, patients present cranial neuropathies and posterior cervical lymphadenopathy. Conversely, symptoms of early stage oropharynx and hypopharynx cancer rarely exist and consequently, the diagnosis is only determined in later stages. Otalgia and persistent unilateral sore throat are referred in these cases. Finally, for cancer arising in the laryngeal region, the symptoms may include hoarseness and pain [51].

Cranial nerve dysfunction, pain, impaired speech and swallowing, and airway compromise may result from head and neck tumour recurrence, particularly in patients who suffer from alcohol and tobacco addiction. Thus, social and psychological care programmes are encouraged in these situations [52].

#### **2.1.3.2. Tumour Staging**

State-of-the-art clinical diagnosis of head and neck cancer often involves removal of CLNs for TNM staging [53]. This staging system comprises all the clinically available information of the patient regarding the cancer. T stands for size and extent of the primary tumour, N refers to the number of metastatic lymph nodes and finally, M refers to whether the cancer has metastasized to secondary sites. Together, the classifications of each letter determines the overall clinical stage (I, II, III, or IV), and may indicate if metastases have spread to other organs [53] [54] [55]. Cancer staging is the assessment of the level of cancer progression and is critical in deciding therapy options. Depending on the type of head and neck tumour different CLNs from a sub-set of levels I-VI (see Figure 2.4) can be removed [56]. Currently CLN assessment often requires surgical removal and subsequent histopathology. More detailed information about the stages of head and neck cancer can be found in Table 2.2.



Table 2. 2: TNM Staging for the Larynx, Oropharynx, Hypopharynx, Oral Cavity, Salivary Glands, and Paranasal Sinuses (adapted from [54]). Tis, T1, T2, T3, T4a and T4b correspond to carcinoma *in situ*, tumour with 2 cm or less in greatest dimension, tumour greater than 2 cm but no more than 4 cm in greatest dimension, tumour with more than 4 cm, moderately advanced local disease and greatly advanced local disease, respectively. N0, N1 and N2 refer to no regional node metastasis, metastasis in a single ipsilateral LN with 3 cm or less in greatest dimension, and metastasis in a single ipsilateral LN with more than 3 cm and less than 6 cm in greatest dimension or in multiple ipsilateral LNs, none more than 6 cm in greatest dimension, respectively. M0 and M1 refer to no distant metastasis and distant metastasis, respectively.

| Stage Grouping |       |       |    |
|----------------|-------|-------|----|
| Stage 0        | Tis   | N0    | M0 |
| Stage I        | T1    | N0    | M0 |
| Stage II       | T2    | N0    | M0 |
| Stage III      | T3    | N0    | M0 |
|                | T1    | N1    | M0 |
|                | T2    | N1    | M0 |
|                | T3    | N1    | M0 |
| Stage IVA      | T4a   | N0    | M0 |
|                | T4a   | N1    | M0 |
|                | T1    | N2    | M0 |
|                | T2    | N2    | M0 |
|                | T3    | N2    | M0 |
| Stage IVB      | Any T | N3    | M  |
|                | T4b   | Any N | M0 |
| Stage IVC      | Any T | Any N | M1 |

## 2.2. Phantom Studies

Realistic physical phantoms are an important tool in MWI system development, for which several authors have reported a number of Tissue Mimicking Materials (TMMs) with dielectric properties comparable to biological tissues, at microwave frequencies.

The human breast has been the most studied organ with MWI, thus more studies have been published over time, with an increasing level of complexity, regarding this region of the body. Several researchers have suggested TMMs for short-lived phantoms of the breast [57] [58] [59] [60]. Such phantoms varied over a large spectrum regarding their simplicity and level of realism. Some of the most simplistic TMMs short-lived phantoms of the breast developed in [57] consisted of a cylindrical structure with a diameter of 10 cm and a height of 30 cm which included TMMs for skin (the structure of the cylinder) and fatty tissues (the interior of the cylinder) and tumours. These tumours were represented with a hemispherical shape attached to a ground plane and placed in the breast model and with dimensions of 1 and 2 cm. Later, phantoms with an increasing complexity levels were built in [59]. Some of the tissues included consisted of a layer of skin, one or two dense inhomogeneous tissues and a spherical tumour. These phantoms were created using hemispheres as the mould. Additionally, anatomically realistic 3D MRI-derived numerical and physical phantoms were developed in [58]. The numerical phantoms were considered immersed in an oil-like coupling medium, with an interior of homogeneous fat, a 2 mm layer of skin and a homogeneous chest wall. The physical phantom was also constructed from MRI exams.

Its realistic shape was formed by a 1-mm-thick mould of polyethylene and it contains two different TMMs for the skin and an interior of homogenous fat. Croteau *et al* [60] created a hemispherical and a realistic model for the breast. In the first case, the skin TMM was constructed with a Plexiglas mould with a hemispherical shape, the fat tissue was poured into the skin mould and finally, a lid with protrusions was used to create the fibroglandular tissue and the tumour cavities. After this, the lid was removed, and a syringe was used to inject the tumour and the fibroglandular liquids. In the case of the realistic breast models, a clay modelling technique was used to form the realistic shape of the breast, the insertion of the skin, tumour and fibroglandular tissue mimicking materials follows the same methodology as described for the hemispherical model.

Long-lasting breast phantoms were also suggested in [61] [62]. In [61], realistic phantoms of the breast were built using a carbon-rubber mixture for the 2 mm skin tissue and a homogenous interior of liquid (e.g., canola oil and glycerine). The phantom created could withstand mechanical stress due to the compression of the breast. According to [62], different proportions of graphite, carbon black and urethane allowed the construction of a TMM which exhibited a wide range of dielectric properties comparable to the dielectric properties of the human soft tissues from 1 to 10 GHz. This TMM was flexible and mechanically strong, therefore it was ideal for creating complex phantoms and robust structures such as skin layers.

In [63], breast phantoms were produced with 3D printed moulds for the skin, adipose tissue, bone, fat, fibroglandular and tumour TMMs. These phantoms were extended to allow variation of local characteristics. More recently, a numerical phantom of the axillary region based on medical image segmentation via DM clustering algorithms, and with the inclusion of the dielectric properties of the tissues for varying microwave frequencies, was reported to permit an alternative methodology for the assessment of the lymph nodes in the underarm region [25].

Inspired by the above detailed breast phantoms, some of the features of the head and neck models that can be considered are: the shape of the moulds (a spherical or ellipsoid shape for the head, and a cylindrical shape for the neck region), the main layers of tissue considered and their heterogeneity. Besides, some of the developed TMMs can also have applicability in the case of the head and neck physical phantoms.

In the context of the head region, few authors have attempted to design models of this region. Scapaticci *et al.* [64] developed a planar numerical model of the human head which consisted of five layers, with different dielectric properties and lengths, concerning skin tissue, fat tissue, cortex bone, CerebroSpinal Fluid (CSF) and brain tissue. A single-pole Cole-Cole model was used to evaluate the behavior of the dielectric properties of biological tissues over a frequency range from 0.1 to 10 GHz. Later, Bjelogrić *et al.* [65] made a contribution to the state-of-the-art by designing a spherically stratified model in which every concentric layer between the brain and the background medium represented a particular tissue. The printed multilayered spherical structure used fused deposition modeling technology with white ABS (Acrylonitrile Butadiene Styrene) for the plastic. Each shell with a 2 mm thickness was filled with liquids mimicking the main human head tissues, such as brain tissue, CSF, cortical bone, fat and skin.

Both numerical and physical phantoms allowed to represent the human body in a simplistic way, compared to one of the most recent numerical models, such as the one developed by Fhager *et al.* [66], where they have added more realism to the phantoms in order to create a realistic simulation environment. The later was based on an existing anatomical tissue model of a healthy subject from BrainWeb [67]. This model includes the main tissues of the head such as CSF, blood, muscle, grey and white matter, fat and skull. They fitted the Debye model to the experimental data to describe the dispersive behavior of the dielectric properties of the different tissues.

From the developed head phantoms, some of the tissues that should be considered when designing head and neck phantoms for radar based MWI screening are the exterior of skin, and also bone tissue and an interior volume of heterogeneous materials. Besides, the single-pole Cole-Cole model has already been used for describing the variation of the dielectric properties of the head biological tissues over the frequency of interest of radar based MWI.

Head and neck phantoms developed so far were used in the context of radiation dosimetry, in which they must be able to represent the biological tissues regarding their x-ray absorption and scattering properties, and their dimensions, thicknesses and depths. Brand *et al.* [68] phantom considered only the bone tissue of the human skull and cervical vertebrae, soft tissues for the interior of the phantom and facial contours and also, air passages in the oral and nasal cavities, paranasal sinuses, pharynx, and larynx. Molineu *et al.* [69] designed a head and neck phantom for intensity-modulated radiation therapy which consists of an anatomically realistic outer plastic shell for the contour of the head and neck, imageable targets with radiation dosimeters, and a remaining volume of water. Head and neck phantoms were also developed in the context of hyperthermia. Paulides *et al.* [70] developed an elliptical shape neck with a homogeneous muscle and some major structures such as trachea and spine. These structures were modeled based on semi-3D approximations from CT scans. Merunka *et al.* [71] adapted and simplified a neck phantom from the whole human body phantom of [72]. The simplified phantom consisted of a cylindrical shape with a diameter of 55 mm and 100 mm of height, with four structures: skin, muscle, cervical vertebrae, and larynx with tumour tissues.

## **2.3. Phantom Development**

The creation of computational phantoms that mimic the biological structures of the human body is a vast field of study. Within the context of this dissertation, I will focus on exploring unsupervised clustering methods to separate the biological tissues of the MRI exams according to their intensity levels, and ultimately, their biological nature. The choice of unsupervised clustering was based on the lack of labelled data available regarding our MRI data. Before applying the clustering methods, filtering techniques are required for data cleaning. The filtering techniques and the unsupervised clustering methods studied in this dissertation are detailed below. Moreover, some methods used in this work to assess the clustering quality are also described in this section.

### **2.3.1. Filtering Techniques**

MRI images are generally prone to Gaussian noise and Salt and Pepper noise due to image acquisition errors, such as sensor noise and electronic circuit noise, and transmission errors. Gaussian noise is a statistical noise with a probability density function of the Gaussian distribution and Salt and Pepper noise consists of corrupted pixels which were either set to have the value 0 or the maximum value of the pixels in the image [73].

The enhancement of the MRI exams is a critical process, especially when analysing medical images. The removal of noise, which corrupts the information in the image, and the smoothness of other sharp transitions (e.g. edges) can be accomplished by using filters in the frequency domain. The Fourier Transform (FT) is a fundamental mathematical tool in signal processing, which allows the two-way conversion between the spatial and frequency domain of the periodic signals that compose a function (image). In the Fourier transform, low frequencies are responsible for the general appearance of an

image over smooth areas, while high frequencies are responsible for detail, *i.e.*, sharp transitions such as noise and edges. If the goal is to remove noise, then filters capable of suppressing high frequencies while leaving the low frequencies unchanged should be applied. This will result in smoothing (blurring) in the frequency domain. Such filters are called Low Pass (LP) filters. In this work, the ideal, Butterworth and Gaussian filters, which cover the range from very sharp (ideal) to very smooth (Gaussian) filter functions, were considered [74].

### **Ideal LP filters**

In these filters, the components of the FT with a frequency above a specified circular cut-off frequency ( $f_c$ ) are completely attenuated while the frequencies below the  $f_c$  value pass without any attenuation. The transfer function,  $H(u, v)$  of these 2D filters is given by Equation 2.1.

$$H(u, v) = \begin{cases} 1 & \text{if } D(u, v) \leq D_0 \\ 0 & \text{if } D(u, v) > D_0 \end{cases} \quad (2.1)$$

with  $D(u, v)$  is the distance from any point  $(u, v)$  to the centre (origin) of the FT, and  $D_0$  represents the specified distance calculated with the  $f_c$  value.

In the spatial domain, the final image resulting from the use of the convolution theorem shows some important characteristics: as the filter in the frequency domain gets narrower, the more severe blurring and ringing effects are shown in the spatial domain [74]. Ringing effects, generally caused by partial or complete loss of high-frequency information, are seen as rippling artifacts near sharp edges in images [75].

### **Butterworth LP filters**

These filters can be viewed as a transition between two “extremes” of filter functions due to their additional parameter called the filter order,  $n$ . For high values of  $n$ , the Butterworth filter approaches the form of the ideal filter, while lower-order values result in smooth filters, similar to Gaussian filters. The transfer function of a Butterworth LP filter is presented in Equation 2.2.

$$H(u, v) = \frac{1}{1 + \left[ \frac{D(u, v)}{D_0} \right]^{2n}} \quad (2.2)$$

A Butterworth LP filter of order 1 does not have a discontinuity as sharp as the ideal LP filter but, conversely, it causes no ringing in any of the images. Order 2 filters have a ringing effect which is generally imperceptible, however the same does not happen for filters of higher orders. According to [74], Butterworth LP filters of order 2 are the best when balancing between efficient lowpass filtering and tolerable ringing characteristics.

## Gaussian LP filters

These filters have the smoothest transfer function out of all the previously mentioned. The transfer function has a Gaussian shape and it is defined by Equation 2.3:

$$H(u, v) = e^{-D^2(u, v)/2D_0^2} \quad (2.3)$$

where  $D_0$  is the standard deviation, *i.e.* a measure of the spread of the Gaussian curve.

Because the inverse FT of the Gaussian LP filter is also a Gaussian, the ringing effect does not exist [74]. In medical imaging, a tight control in the transition between the low and high frequencies is sometimes required. Besides, the absence of ringing is a very important factor when choosing a LP filter. When the separation between the frequencies that should pass or be removed is a determining factor for image processing, then Butterworth LP filters of order 2 should be considered given its narrower profile compared to the Gaussian profile, for the same value of cut-off frequency [74]. Otherwise, Gaussian filters are usually preferred over Butterworth filters.

## Median filters

Unlike the above-mentioned linear filters, in which the output value of a pixel results from a linear combination of the values of the pixels in the neighbourhood, non-linear filters such as the median were also tested at this stage. Non-linear filters are spatial domain filters, as opposed to the previous frequency domain filters. Particularly, the median filter allows the replacement of the value of a pixel by the median of the gray levels in its neighbourhood [74]. These filters are quite effective in the presence of Salt and Pepper noise and cause less blurring than linear smoothing filters of similar size [74].

### 2.3.2. Unsupervised Clustering Techniques

Image segmentation is a process of utmost importance for many medical image analysis tasks because it allows the partitioning of the image into non-overlapping homogenous regions of comparable properties such as intensity, depth, colour, or texture [76]. The goal is to change the representation of the image into something that is more meaningful and easier to comprehend. Image segmentation is typically used to locate objects and boundaries (lines, curves, etc.) in images [77].

DM is the process of discovering interesting patterns and knowledge from considerable amounts of data. It comprises techniques from distinct domains, such as statistics, pattern recognition, machine learning, and others. Typically, we use clustering methods, also known as unsupervised learning, to discover hidden patterns within the data [78] [79]. Hence, for some applications, clustering is also called data segmentation and it can be successfully applied to medical image analysis [80].

Clustering is the process of grouping a set of data objects into clusters (which should be grouped by similarity and in principle should correspond to different classes) by maximizing intraclass similarity and minimizing interclass similarity. Traditional clustering techniques are broadly classified into the following categories: partitioning methods, hierarchical methods, density-based methods, and grid-based methods [78]. Apart from the grid-based methods, which take a space-driven approach, all the previously mentioned methods are data-driven – they partition the set of objects according to their distribution in the embedding space. In space-driven methods, the partition of the embedding space into

cells occurs independently of the distribution of the objects [78]. All previously mentioned data-driven methods will be intensively presented below.

The proximity measure is an important step since it allows the definition of the concept of similarity between data samples. Some methods, such as the partitioning methods, determine the similarity between objects given the distance between them. Different types of distance between samples include the Euclidean, city block (or Manhattan), Chebychev and Mahalanobis distances [81]. In others, such as density-based methods, the similarity does not rely on the absolute distance between objects but may be defined by the notion of density (number of objects in their neighbourhood region), which allows the creation of clusters of arbitrary shape [78].

## Partitioning Methods

Partitioning methods are generally distance-based methods that divide the data into  $k$  clusters, each with a minimum of one object. These methods are also classified as parametric techniques, since the number of clusters must be defined *a priori*. Objects within the same clusters are considered “close” whereas the ones in different groups are considered “far apart”. The most well-known and commonly used partitioning techniques is the K-means. The K-means method is a centroid-based technique in which the centroid of a cluster is its centre point, *i.e.* the centroid is defined as the mean of the objects assigned to each cluster. This method is extremely sensitive to outliers and noise since the mean value of the clusters is easily distorted by these data points. Besides, it is efficient in finding mutually exclusive clusters of spherical shape in small- to medium-size datasets, although it is not suitable for discovering nonconvex shaped clusters. Moreover, the need for the *a priori* specification of the  $k$  number of clusters can be considered as a disadvantage of this method [78]. In order to tackle this limitation of the partitioning methods, some analytical techniques have already been studied to determine the optimal  $k$  [82] [83].

In the medical analysis research area, partitioning algorithms have been widely used for image segmentation. Rajapakse *et al* [84] presented a three-tissue model which uses the K-means method to segment cerebral MRI images, by distinguishing between the major three tissue classes within the brain (white matter, grey matter and cerebrospinal fluid). The algorithm was proven sufficiently accurate even in the presence of noise and intensity inhomogeneities of the scanners. Later, Chen *et al* [85] described an algorithm combining 3D segmentation using K-means clustering and knowledge-based morphological operations on a sequence of cardiac CT volumetric images. This technique was proven very successful at differentiating regions which may be separate in anatomy but whose boundaries are not clearly defined by image intensity information. The K-means methodology was also shown valuable when used as a primary segmentation on MRI images before applying improved watershed segmentation algorithms. By using the proposed process, Ng *et al* [77] were able to considerably reduce the amount of over-segmentation when segmenting the masseter, a muscle of mastication. Later Riahi's [86] results showed great effectiveness of the designed K-means clustering algorithm in detecting the borders of different sized brain tumours found in MRI scans. More recently, Muneer and Joseph [87] and Sharma *et al* [88] tested the performance of K-means algorithms for brain lesion detection using MRI examinations.

In the context of lymph node segmentation, Conceição *et al* [25] presented a methodology for segmenting torso tissues and axillary lymph nodes in the axillary region, in which they used K-means clustering tools to segment CT images of the upper torso.

## Hierarchical Methods

These methods, which can be distance-based or density-based, organise data objects into a hierarchy of clusters. They are categorized into agglomerative algorithms when clusters are recursively merged together into larger clusters, or divisive ones when clusters are split into smaller groups, *i.e.* subclusters. As merging and splitting decisions cannot be undone, nor perform object swapping between clusters, hierarchical clustering methods can lead to poor quality clustering if the decisions are not well chosen [78].

Unlike the K-means algorithm, the hierarchical method does not require *a priori* knowledge of the number of clusters. Instead, it allows the introduction of this number in the algorithm as a termination criterium for merger/splitting decisions.

Agglomerative algorithms start by treating each observation as a separate cluster. Then, it follows the computation of a similarity (distance) matrix, which exhibits the distance between all clusters [89]. Several distance metrics are available, and their choice depends on the data. For example, the Euclidean distance, which is the most commonly used, is the length of the straight line drawn from one cluster to another. Next, the linkage metric will define how the distance is computed. The type of linkage metric used has a significant impact on hierarchical algorithms because it reflects the concept of closeness. Among these, the single-link and complete-link algorithms are most popular in large datasets [79] yet very sensitive to outliers or noisy data. Besides, average linkage, and sum of square distances, also known as the Ward linkage, are also frequently used [78].

In a comparative study of brain tumour detection using Digital Imaging and Communications in Medicine (DICOM) images, the hierarchical algorithm was proven faster – almost half of the time required by K-means clustering in the segmentation of MRI brain scans [89]. More recently, Gors *et al* [90] studied a hierarchical clustering algorithm applied to Alzheimer's disease detection.

In order to improve cluster quality in hierarchical methods, other clustering techniques were integrated in the hierarchical method, resulting in multiphase clustering such as Balanced Iterative Reducing and Clustering using Hierarchies (BIRCH). Compared to Agglomerative methods, BIRCH gains in scalability and in its ability to undo the previous decisions of merging or splitting clusters. First, it hierarchically partitions the objects into a tree structure, the Characteristic Feature Tree (CFT), where each subcluster contains statistical information of the objects within it. Then, any clustering algorithm, such as a typical partitioning algorithm, is applied to perform clustering on the leaf nodes of the CFT [78].

## Density-based Methods

Density-based clustering algorithms offer the possibility to find clusters of arbitrary shapes, in presence of noise and without prior knowledge, such as the number of clusters. Besides, fewer parameters at the start of the process are required in comparison with the above approaches [91] [92]. In this technique, clusters are modelled as dense regions in the data space, separated by sparse regions [78].

Density-Based Spatial Clustering of Applications with Noise (DBSCAN) is one of the promising density-based clustering techniques which detects arbitrary clusters using two user defined thresholds: *Epsilon* (Eps) and Minimum Points (MinPts) which correspond to the radius of a neighbourhood for every object and the density threshold of dense regions, respectively. The Eps-neighbourhood of an object is the space within a radius, Eps, centred at the object and the density of a region is measured by the number of data objects within the region circumscribed by that radius [78]. Initially, DBSCAN starts

by marking all the objects in the dataset as *unvisited*. Then it randomly selects an *unvisited* object  $p$ , marks it as *visited* and observes if the Eps-neighbourhood of  $p$  has at least MinPts objects. If not,  $p$  is marked as a noise point. Otherwise, a new cluster  $C$  with  $p$  is created and the objects within the Eps-neighbourhood of  $p$  are considered as a subset of objects  $N$ . Of the objects of  $N$ , those that do not belong to any cluster are iteratively added to  $C$  until the subset  $N$  is empty. At this time,  $C$  is completed. The following cluster is created by selecting a new *unvisited* object  $p$  from the initial dataset.

In short, this technique detects the dense area first and then allocates non-dense areas to one of the dense clusters based on a proximity criterion function. Thus, it can easily detect outliers [81].

Celebi *et al* [91] adapted a DBSCAN clustering algorithm to perform the detection of the boundaries of the skin lesions and identification of subregions within the lesion with different colouring. The proposed algorithm was able to accurately detect the lesion borders in 80% of the image samples and was proven valid for different colour subregions identification. Bandyopadhyay and Paul [93] also studied the performance of a DBSCAN algorithm for segmenting brain tumours from MRI exams. More recently, Roy and Bhattacharyya [92] have adopted a generalized version of a DBSCAN clustering algorithm in order to segment grey and white matter along with tumour tissues using brain MRI scans.

### 2.3.3. Clustering Quality

After applying a clustering algorithm, it is important to assess how good the resulting clusters are. When the ground truth of a dataset is available, we use extrinsic methods to compare the clustering against the group truth. Otherwise, intrinsic methods which evaluate the goodness of a clustering by considering how well the clusters are separated are used [78]. Some of the intrinsic methods tested in this work included: the silhouette coefficient, the David-Bouldin index, and the Calinski-Harabasz index, which are detailed below. In this work, clustering evaluation algorithms are particularly important for the determination of the optimal  $k$  number of clusters to be used when performing data segmentation.

#### Silhouette coefficient

This coefficient is computed for all objects of a dataset. Its value varies between 1 and -1, whether the object belongs to a compact cluster and it is far away from other clusters, or the object is closer to objects in other clusters rather than objects within the same cluster, respectively [78]. For each data point, this coefficient ( $s$ ) is defined by Equation 2.4:

$$s = \frac{b - a}{\max(a, b)} \quad (2.4)$$

where  $a$  and  $b$  represent the average distance between a sample and all other points in the same cluster and the minimum average distance from a sample of a cluster to all other clusters, respectively. Alternatively, it is also possible to compute the average silhouette coefficient value of all objects within a cluster in order to measure the cluster's fitness within a clustering [78]. Some of the advantages of using the silhouette coefficient in clustering evaluation include the fact that the score of the coefficient is bounded to the interval  $[-1, 1]$  and it is easy to understand that the higher the score, the denser and more well separated the clusters are.



### Davies-Bouldin Index (DBI)

This index takes into consideration both errors caused by representing the data objects with their cluster centroids (intra cluster diversity) and the distance between clusters (inter cluster diversity) [94]. Intra cluster diversity of a cluster  $j$  is given by the Mean Square Error (MSE) value in Equation 2.5.

$$MSE_j = \frac{1}{N} \sum d(c_j, x_i)^2 \quad (2.5)$$

where  $N$  is the number of data vector,  $d$  represents the distance between the data vector  $x_i$  and the centroid of the cluster  $j$ ,  $c_j$ . Small values of intra cluster diversity reflects the compactness of the clusters. Inter cluster diversity is calculated as the distance between the centroids,  $c_j$  and  $c_k$ , of the two clusters  $j$  and  $k$ , respectively. Moreover, a measure of closeness,  $R_{j,k}$ , can be obtained from the intra and inter cluster diversities in Equation 2.6.

$$R_{j,k} = \frac{MSE_j + MSE_k}{|c_j - c_k|} \quad (2.6)$$

Small values of closeness indicate well separated clusters. Conversely, large values of  $R_{j,k}$  refer to clusters close to each other. Then, the DBI is defined in Equation 2.7.

$$DBI = \frac{1}{M} \sum_{j=1}^M \max_{j \neq k} R_{j,k} \quad (2.7)$$

where  $M$  is the number of clusters [95].

The lower the DBI, the better the partition of the data.

### Calinski-Harabasz Index (CHI)

This index, in Equation 2.8, expresses the ratio between cluster variance and the overall within-cluster variance.

$$CHI_k = \frac{N - k}{k - 1} \frac{BCSS_k}{WCSS_k} \quad (2.8)$$

where  $N$  refers to the number of data points,  $k$  represents the number of clusters,  $BCSS_k$  is the between cluster sum of squares, and  $WCSS_k$  is the within cluster sum of squares [96]. A higher value of CHI relates to a model with better defined clusters. Although this algorithm is fast to compute, this index is generally higher for convex clusters than other types clusters, such as the ones obtained from density-based clustering [97].

## 2.4. Head and Neck Modelling

Medical MWI systems promise additional imaging and diagnosis tools. These systems use signals based on the dielectric contrast between different tissues, propagating through the body to visualise internal structures. To test them, the anatomical region of interest needs to be mimicked, with special attention to tissue architecture, distribution, and dielectric properties. Within this section, a review of some important topics regarding head and neck modelling is presented. Such topics include studies regarding both dielectric properties of biological tissues and developed numerical and realistic phantoms of the human body, especially of the head and neck region.

### 2.4.1. Dielectric Properties

In the context of medical MWI, an external electromagnetic field is applied to biological materials resulting in electromagnetic scatterings generated by tissues with different dielectric properties. The interaction between the materials and the electrical field is described by the complex permittivity,  $\epsilon$ , in which the real part,  $\epsilon'$ , refers to the amount of energy stored in the material, and the complex part  $\epsilon''$  given by Equation 2.9, is the loss factor that includes both dielectric loss,  $\epsilon_d''$ , and conductivity,  $\sigma$ , the latter given in Siemens per metre (S/m). The complex permittivity parameter is measured in terms of Faraday per metre (F/m). Generally, the relative permittivity,  $\epsilon_r$ , is used which is dimensionless [98]. To achieve this, the complex permittivity is divided by the permittivity of free space,  $\epsilon_0 = 8.854 \times 10^{-12}$  F/m, in Equation 2.10.

$$\epsilon'' = \epsilon_d'' + \frac{\sigma}{\omega} \quad (2.9)$$

$$\epsilon_r = \frac{\epsilon}{\epsilon_0} = \frac{\epsilon' - j\epsilon''}{\epsilon_0} \quad (2.10)$$

where  $\omega = 2\pi f$  is the angular frequency of the field in radians per second.

Together, the conductivity and relative permittivity form the more relevant dielectric properties of biological tissues as a function of frequency, where the latter is intrinsically related to the water content present in the tissue sample. In a rich water content tissue, such as muscle, the values of permittivity are greater than those of low water content tissues, such as fat. Likewise, higher values of conductivity are found in high water content tissues. Considering a microwave travelling through a tissue: the higher the conductivity of the tissue (and water content), the more energy will be absorbed by or lost to that tissue and consequently, the greater will be the attenuation of the microwave energy and the lower will be the penetration depth of the radiation. Moreover, the conductivity increases with the frequency [21].

Cancerous tissues differ significantly from healthy tissues regarding their dielectric properties. The morphological and physiological changes that occur in tumour cells affect their membrane permeability, and consequently, the process of osmosis, by causing an increase of water flow to the interior of the cell. Hence, the extra quantities of water and sodium ions inside the cancerous cells lead to greater values of conductivity and relative permeability when compared to healthy cells of the same tissue type [99].

### 2.4.2. Dielectric Properties of biological tissues

A small number of studies [100] [101] [102] have addressed the dielectric properties of tissues of healthy and metastatic Axillary Lymph Nodes (ALNs) in the context of breast cancer. Joines *et al* [101] first measured the electrical conductivity and relative permittivity of 6 malignant ALN tissues from 50 to 900 MHz. No healthy ALNs were analysed. Later, Choi *et al* [102] examined the dielectric properties of breast cancer tissue and ALNs tissue in frequencies ranging between 0.5 GHz and 30 GHz. They observed that metastatic lymph nodes showed dielectric characteristics similar to the bulk cancer tissues but completely different from normal ALNs. More recently, Cameron *et al* [100] conducted a preliminary study of the electrical properties of healthy and malignant LNs. They measured the dielectric properties of 23 samples by placing probes in contact with the exterior surface of the nodes and also in contact with its cross-section surface. Results showed higher permittivity and conductivity in tissues with tumour content. The measurements in this study are encouraging but not conclusive, especially due to the limited number of samples.

Dielectric properties of CLNs have not been directly studied, but Malich *et al* [103] suggested significant contrast between benign and malignant CLNs properties through the use of EIS to differentiate sonographically-located suspicious or highly suspicious CLNs.

In 1996, Gabriel *et al* [104] [105] completed a comprehensive study in which they measured dielectric properties of many human tissues such as the heart, lungs, muscle, skin, bone, etc, which are the tissues surrounding CLNs that have to be considered in the head and neck model.

### 2.4.3. Finite-Difference Time-Domain Method

The Finite-Difference Time-Domain (FDTD) method has been widely used to model the propagation of electromagnetic waves in a specified material and simulate its behaviour at several frequencies. The dielectric properties of biological tissues are frequency-dependent and their variation with frequency is very complex; hence the dielectric properties of biological materials are very dispersive [106]. In order to incorporate dispersion into the FDTD methods, some auxiliary formulations that describe the behaviour of the dielectric properties of biological tissues over a wide frequency band are required.

The dielectric spectrum of a tissue is characterized by three main relaxation regions at low, medium and high frequencies and by some minor dispersion. To a first order approximation, the expression for the complex relative permittivity,  $\varepsilon^*$ , is a function of angular frequency, as given in Equation 2.11 by the Debye model, which corresponds to the manifestation of a single polarization mechanism over the frequency range:

$$\varepsilon^*(\omega) = \varepsilon_\infty + \frac{\varepsilon_s - \varepsilon_\infty}{1 + j\omega\tau} + \frac{\sigma_s}{j\omega\varepsilon_0} \quad (2.11)$$

where  $\tau$  is the relaxation time constant,  $\sigma_s$  and  $\varepsilon_s$  refer to the static ionic conductivity and static permittivity at  $\omega = 0$ , respectively, and  $\varepsilon_\infty$  represents the permittivity at  $\omega = \infty$  [105].

Despite being very intuitive and of fast computation, the Debye model does not represent the frequency variation of many biological tissues accurately over a wide frequency band because of the complexity of biological materials. In this case, each dispersion region may be broadened by multiple contributions to it. The Cole–Cole model offers an alternative approach since it introduces a distribution

parameter that accounts for the broadening of the dispersion. Moreover, the spectrum of a tissue is better described in terms of multiple Cole-Cole dispersions, given by Equation 2.12.

$$\varepsilon^*(\omega) = \varepsilon_\infty + \sum_n \frac{\Delta\varepsilon_n}{1 + (j\omega\tau_n)^{(1-\alpha_n)}} + \frac{\sigma_s}{j\omega\varepsilon_0} \quad (2.12)$$

where  $\Delta\varepsilon = \varepsilon_s - \varepsilon_\infty$ ,  $\alpha$  is the distribution parameter,  $n$  is the number of relaxation mechanisms considered in the whole frequency range of interest and  $\tau_n$  is the relaxation time constant of each relaxation mechanism [105].

In conclusion, the Cole-Cole model is usually used as a fitting tool with the purpose of describing the variation of the dielectric properties within biological tissues, even though it is not adequate for modelling the propagation of the electromagnetic waves in this type of tissue, given the complex numerical computation of electromagnetic fields [107]. On the contrary, the Debye model is very intuitive and of fast computation but does not represent accurately the biological tissues' dispersive dielectric properties over a wide frequency band [108].

## 2.5. Chapter Conclusions

This chapter details some important anatomical structures of the cervical region of the human body which are vital when designing an anthropomorphic phantom of this region, especially when aiming at organising the LNs within levels from I-VI. The anthropomorphic phantom generator will be further discussed within chapter IV.

The phantom studies revised contributed and served as inspiration to the head and neck phantoms design process. Such process requires additional steps regarding the pre-processing of the MRI exams which were highlighted in section 2.3.

In addition, this chapter also demonstrates how the study of the dielectric properties of biological tissues have been used to identify and then model diseased tissues, hence validating the importance of MWI for clinical diagnosis.

## Chapter III – 3D Numerical Models

This dissertation is divided in two main objectives. In this chapter, only one objective is addressed: the development of a phantom generator of 3D computation models for the head and neck region with different levels of complexity. I also intend to create a repository of these models to be accessed within the research group. The second objective of developing a repository of computational anatomically realistic phantoms based on MRI segmented data will be later discussed in Chapter IV.

Chapter III starts with a detailed description of relevant preliminary data that served as basis for the initial part of this dissertation and the methodologies used to represent the biological tissues in a numerical model. Then, the developed 3D numerical phantom generator will be presented along with all its structures and levels of complexity. Finally, this chapter ends with the limitations encountered over the course of this part of the work and some simple conclusions.

### 3.1. Materials

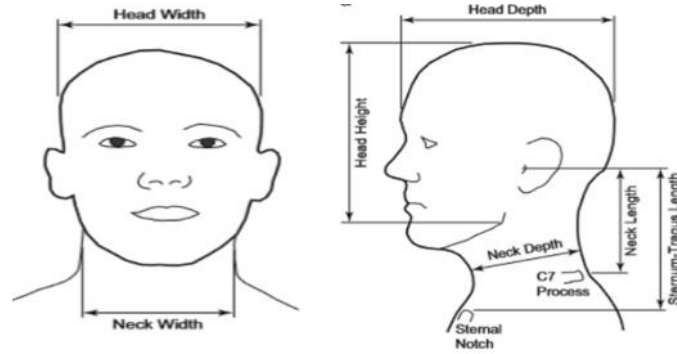
Previous work developed within the research group was focused on creating 2D numerical models of the underarm region. In order to obtain such models, which are published in [25] [26] [27], my group colleagues have utilised a “building-block” technique that allowed the creation and inclusion in the model of numerical structures aimed at mimicking the biological tissues observed in their region of interest, the axilla. Tissues such as skin, muscle, heterogenous tissue (mixture of adipose and fibro-connective tissue), and LNs could be inserted in these models.

Similarly, I intend to obtain analogous type of models for the head and neck region in order to assess the feasibility of the MWI prototype system in imaging and diagnosing CLNs. Hence, 2D numerical models of the cervical region have been developed in MATLAB® R2018a based on the recent work within the group, which was previously mentioned. During the construction of these models, vast structural changes were performed since my focus was on a very different body region which includes biological structures such as skin, muscle, bone, subcutaneous adipose tissue, mixed tissues (later discussed in the methodology section) and LNs. Moreover, later modifications were necessary in order to convert the 2D model into a more realistic 3D model. This section details the final 3D phantom generator for head and neck region obtained during my work.

### 3.2. Methodology

The numerical models developed in this section are not anatomically realistic shaped, yet they are anatomically inspired and a reasonable approximation and good starting point for feasibility studies. Each numerical phantom was modelled with the dimension of 40.0 cm in the three coordinates, the volume size is  $800 \times 800 \times 800$  voxels and the unitary element of the grid represents 0.5 mm of height, length and depth. To model the human head and neck, a volume bound by an ellipsoid and a cylinder

were used, respectively. The dimensions used for these structures approximate their real average size according to [29], the values, in cm, are shown in Figure 3.1.



|             | Width | Height/Length | Depth |
|-------------|-------|---------------|-------|
| <b>Head</b> | 15.0  | 20.0          | 20.0  |
| <b>Neck</b> | 12.0  | 5.0           | 12.0  |

Figure 3. 1: Schematics of the nomenclature used for the coordinates above; coronal plane at top left and sagittal plane at top right. The values in cm used to model the head and neck are presented below. (Adapted from [29]).

In the head, I have differentiated three ellipsoid-shaped layers with different thicknesses corresponding to skin, fat and muscle tissues, and a nucleus of a material called mixed tissue. From the outside perspective towards the nucleus, the first superficial layer corresponds to skin tissue with a thickness of 1.4 mm [109]. Immediately after the skin, a second layer was included which corresponds to subcutaneous adipose tissue with 6.0 mm of thickness. [110] Finally, a layer corresponding to the cranium with a thickness of 4.0 mm was included [111]. To all the above tissues, a unique value was associated to the specific tissue type considered. This value is vital when associating the dielectric properties to the tissues, however this will be later discussed in a more complex model, in Chapter IV.

The head and neck region of the human body is an extremely complex area which consists of compact zones of different tissues with different sizes, shapes and directions. In some regions the main structures are easily identified, but there are other regions where this task is not that easy given the mixture of different and small tissues observed. With this in mind, the remaining volume, which is referred to as the mixed tissue, consists of a mixture of a variable amount of adipose tissue, loose connective tissue, platysma (muscle) and small bones [30]. In this case, the model will either associate a unique value of intensity to this tissue type as before, or randomly associates two different values of intensity (lower and upper bound) to the voxels, depending on the level of variability of the dielectric properties the user intends to introduce in the model.

The neck region was modelled with concentric cylinders. I considered four main tissues aside from the heterogeneous region previously mentioned. From the exterior to the interior, the skin corresponds to the first and superficial layer immediately followed by the layer of the subcutaneous adipose tissue – the second layer. The third layer is the muscle layer with a thickness of 25.0 mm [112] which mimics the sternocleidomastoid and trapezius muscle distribution in order to protect the cervical vertebrae, which are represented in the fourth layer - the bone tissue. Figure 3.2 shows the central coronal slice of the developed phantom for the head and neck region with all the previously mentioned anatomical structures.

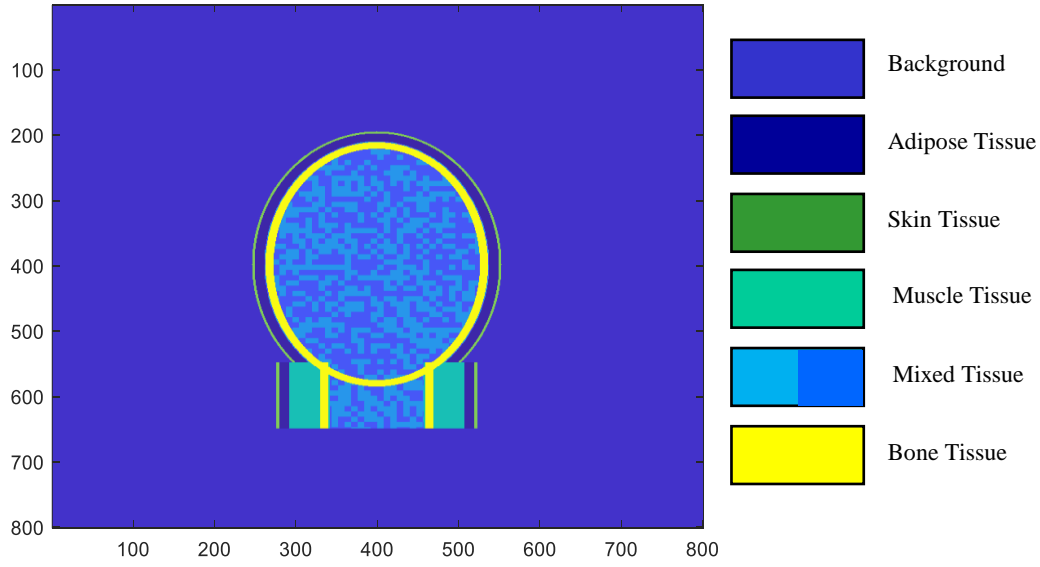


Figure 3. 2: Representation of the central coronal slice of the developed phantom, which includes the skin tissue, adipose tissue, muscle tissue, bone tissue, and mixed tissue.

LNs were also included in the 3D numerical phantoms. Their shape varies between round, oval, or bean-shaped structures, although in this work the LNs were considered oval for the purposes of simplification. In healthy conditions, LNs size ranges from 1.0 to 25.0 mm long, in its major axis. When diseased, the LNs are swollen and bigger than normal LNs due to high concentrations of tumour cells inside them [32]. Two structures can be identified in a LN: its surrounding perinodal adipose tissue, and the LN itself. Literature has shown that the dielectric properties of these two groups differ significantly, therefore two tissues are taken into consideration when developing the representation of LNs in the numerical model [100]. As mentioned before, LNs can be divided into six levels depending on their location. Figure 2.4 shows the frontiers of the head and neck region that were taken into consideration in the 3D numerical model. The six different volumes were obtained with a rough translation of this representation to the 3D head and neck model.

An example of a 3D model which includes all the previously discussed tissues such as skin, muscle, fat, bone and mixed tissue and LNs, both healthy and diseased, is shown in Figure 3.3. In this figure, the coronal plane of the volume modelled which contained the centre of the LNs is considered.

The described methodology used to develop numerical models of the specific tissues within the head and neck region of the human body, was taken into consideration while developing the phantom generator. The later will be the focus of the next section.

Note that I fully developed the described methodology, hence this section also comprises part of the results obtained during this project. The following section includes the remaining part of the obtained results, particularly those which come from the application of the developed methodology.

a)

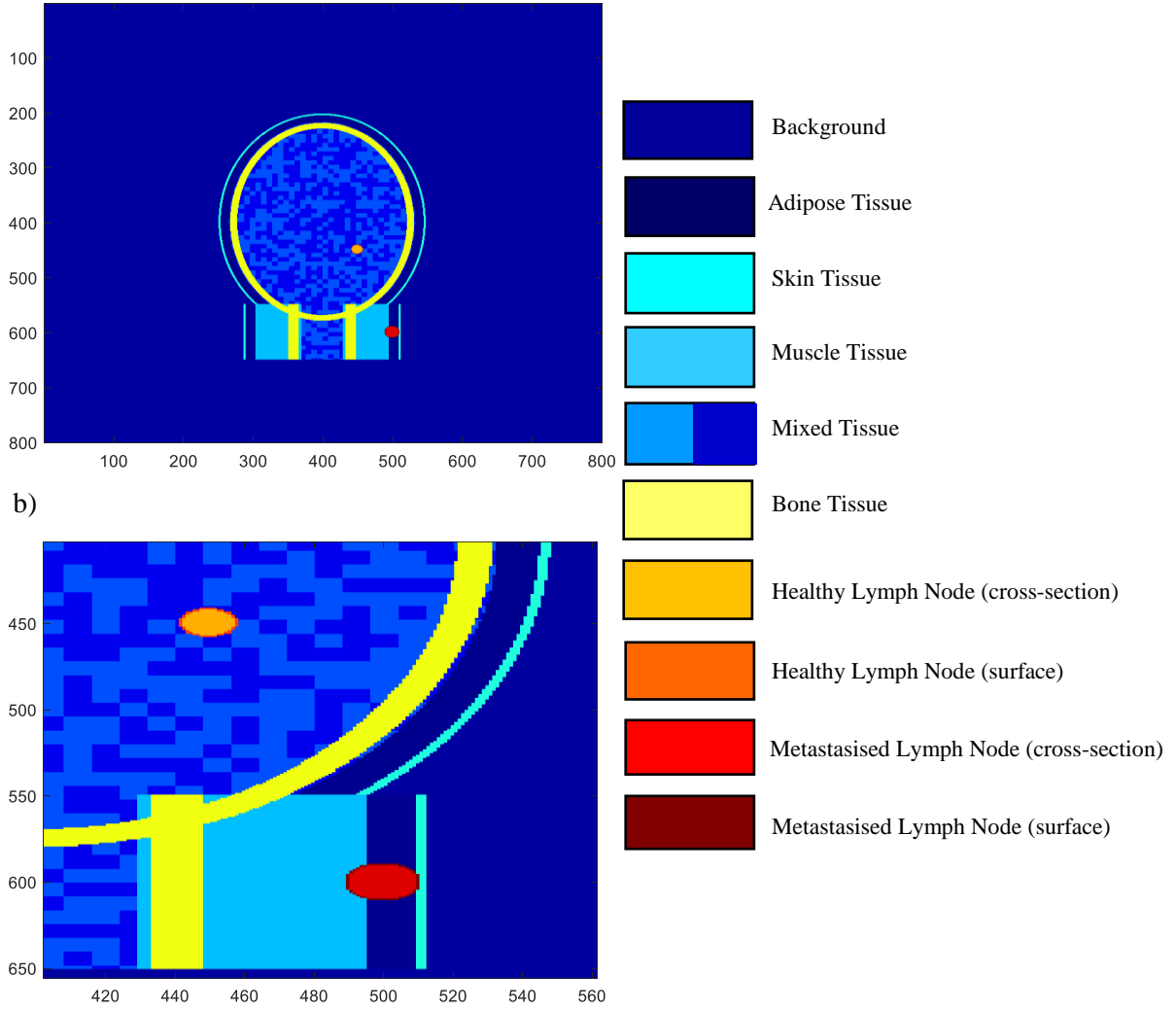


Figure 3. 3: a) Representation of a model which includes all the previously discussed tissues such as skin, muscle, fat, bone and mixed tissue and LNs, both healthy and diseased. b) “Zoom in” of the representation above in order to better visualise the different tissues type of each lymph node.

### 3.3. Results and Discussion

The creation of the first 3D numerical phantoms generator is the first original goal to be achieved during this project. A numerical phantom generator allows the user to create various phantoms of the region of interest, the head and neck region in this study. In addition, it gives freedom of choice regarding the level of complexity of the phantom, the biological structures to be included in the model, and the number and location of CLNs.



### 3.3.1. Numerical Phantom Generator

When creating a new phantom, users are asked several questions in order to personalise their model. The first group of questions concerns the biological tissues to be incorporated in the model. The initial step refers to the addition of subcutaneous adipose tissue (Figure 3.4). This tissue is represented by an ellipsoid-shaped layer. Between all the regions studied in [110], the submandibular region is the one which is located in the area of interest, therefore the subcutaneous adipose tissue thickness of the models was generalised to 6.0 mm.

The following steps concern the inclusion of muscular (Figure 3.5) and bone tissue (Figure 3.6). Some simplifications were performed at this phase since the development of the 3D numerical phantom generator served as a basis for the final objective of this work, the anatomically realistic 3D phantom generator. These simpler models are essential to develop MWI algorithms capable of detecting CLNs. Some examples of the simplifications performed at this phase include: (i) the muscular tissues in the head were neglected as the main structures in this region consist of bone and brain, (ii) only the cranium and vertebrae were represented in the model as bone tissue, (iii) the muscular tissues in the neck which mimic the sternocleidomastoid and trapezius muscle distribution in order to protect the bone tissue are represent by a cylinder, which in turn, surrounds the mixed tissue. For the purpose of this generator no more complexity and details were required since I was only concerned with the representation of the main tissue types observed in the head and neck region of the human body.

The incorporation of the mixed tissue in the model is the fourth step (Figure 3.7). The mixed tissue, which represents the remaining tissues of the head and neck that were not described above, can be further modelled as homogenous or heterogeneous depending on the variability of the dielectric properties the user intends to assign to the model (Figure 3.8).

Finally, the addition of skin tissue is the last step of the first group of questions asked to users (Figure 3.9). Although Chopra *et al.* [109] have demonstrated that the average dermal thicknesses of the head and neck regions, such as anterior and lateral neck and posterior scalp, varies from 1.2 mm to 1.4 mm, the models were chosen to have a constant value of skin thickness. If, on the one hand, the model becomes simpler, on the other hand, the use of an average value removes the real aspect of skin thickness variability.

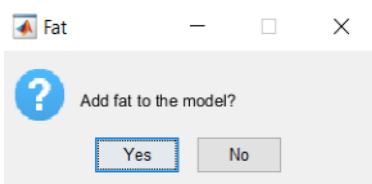


Figure 3. 4: Interface which allows the user to add subcutaneous adipose tissue to the phantom.

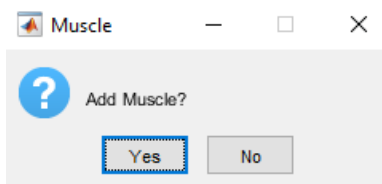


Figure 3. 5: Interface which allows the user to add muscular tissue to the phantom.

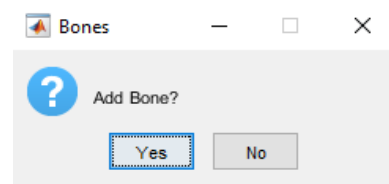


Figure 3. 6: Interface which allows the user to add bone tissue to the phantom.

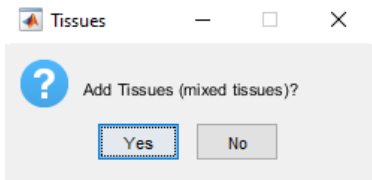


Figure 3. 7: Interface which allows the user to add mixed tissue to the phantom.

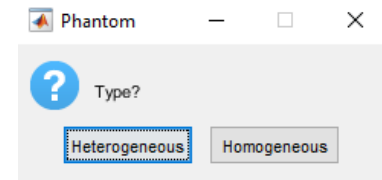


Figure 3. 8: Interface which allows the user to choose the variability of the dielectric propertities of the tissues included into the mixed tissue type.

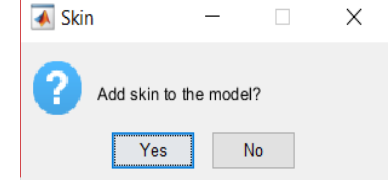


Figure 3. 9: Interface which allows the user to add skin tissue to the phantom.

The second group of questions concerns the LNs (Figure 3.10); their number (maximum of ten in total and five per level – hence we guarantee that they are located in the desired level and do not overlap regardless their size) (Figure 3.11), size, state (healthy/metastasised) and coordinates of its centre (Figure 3.12). As mentioned before, the primary model of the head and neck has already been separated into six different regions that correspond to the six levels of LNs. These regions as well as their frontiers are clearly defined and shown to the users, which allows them to finger point the location where they wish to place the LNs (Figure 3.13). Besides, with this type of methodology, the users can choose whether they prefer the LNs to be close together, or conversely, far apart.

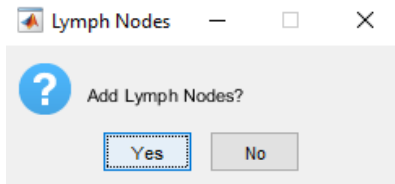


Figure 3.10: Interface which allows the user to add lymph nodes to the phantom.

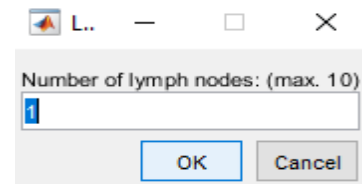


Figure 3.11: Interface which allows the user to add the number of lymph nodes to the phantom.

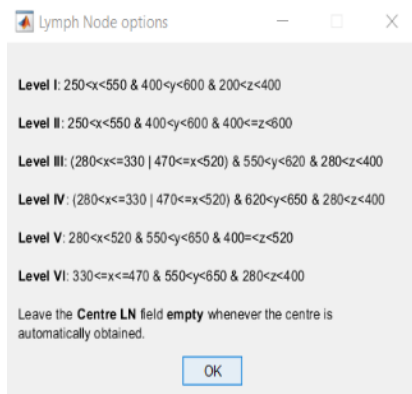


Figure 3.12: Informative note which specifies the frontiers of the six different levels of the lymph nodes.

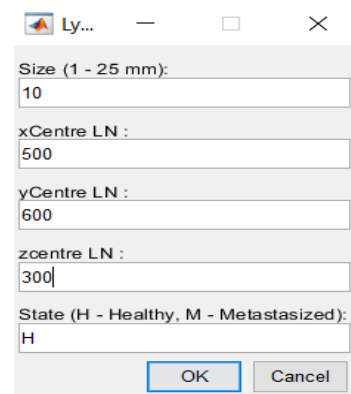


Figure 3.13: Interface which allows the user to choose the size, location and state of a lymph node.

If the user is not interested in specifying the location of the LNs, the phantom generator will automatically assign the locations of the LNs (Figure 3.14). After designing the phantom, the user can choose whether he/she desires to save the phantom (Figure 3.15). In the case of an affirmative answer, the phantom will be saved in a .mat file.

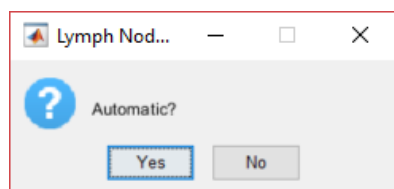


Figure 3.14: Interface which allows the user to choose whether he/she wants to specify the location of the LNs or if he/she prefers the phantom generator to automatically assign positions to the LNs.

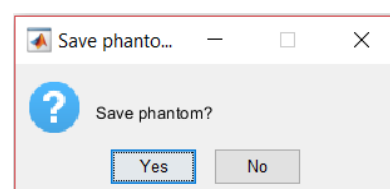


Figure 3.15: Interface which allows the user to save the designed model of the head and neck in a .mat file.

### **3.4. Chapter Conclusions**

In this chapter, details of all the functionalities of the 3D numerical phantom generator, which were developed within the scope of this dissertation, are presented. This generator allows the users to decide the features they wish to project onto the phantom; thus, several combinations of characteristics can be designed in order to approximate the model according to the interests of the researchers. The creation of a generator that allows the personalisation of models of the head and neck of the human body extends their applicability to several fields of research.

The models obtained with the 3D numerical phantom generator result from several approximations to the reality, though with different levels of complexity. In some cases, for example the shape and size of the head and neck, the approximations resulted in numerical structures with high level of similarity to the anthropometry of the body. The representation of the skin tissue in these models was also very satisfactory, although some limitations were highlighted regarding the impossibility of thickness variability. Conversely, other tissues, such as bone and muscle tissue, were represented in these phantoms in a very simplistic way. Other simplifications were also performed, for example: the creation of an artificial tissue (mixed tissue) that gathered all remaining tissues in the head and neck regions (e.g. regions with a variable amount of adipose tissue, connective tissue, muscle and small bones), the approximate definition of the LNs levels, and finally the fixed oval shape of the LNs. Improving these numerical models was not a priority in this work since they were used as a starting point to reach more complex and realistic models that reflected anatomical knowledge. However, future work in this area could include some improvement efforts, such as the determination of more realistic measures, shapes and locations of the biological structures within the cervical region and also, the incorporation of smaller and/or less representative tissues.

In conclusion, although numerical phantoms are a good approximation and starting point for feasibility studies, they only provide limited anatomical realism. Nonetheless, simple numerical phantoms are useful for initial development of technologies as very complex models may hinder initial progress.

In order to address the limited anatomical realism of the numerical phantoms, anthropomorphic models were developed while working in this project.

## Chapter IV – 3D Anthropomorphic Models

The second goal of this project consists of creating a generator of 3D computational anatomically realistic phantoms of the head and neck regions based on the anatomical realistic distribution of tissues observed and detected in MRI exams. The focus of this work is on developing phantoms of this region which will allow the study of CLNs using medical MWI systems. Since I was designing the head and neck phantom development process from scratch, the methodology pipeline was applied to only one MRI exam, although it can be later applied to others MRI exams to increase phantom variability. Nevertheless, the developed phantoms show partial variability since they allow the CLNs positioning in different levels.

This chapter starts with a section describing the datasets studied during this work, and the software utilised to manipulate data and construct the phantom generator.

Section 4.2 details the procedure of building the phantom generator. Firstly, it comprises a description of the process of selecting the MRI exam which will be used for constructing the anatomically realistic models. Then, data normalisation and data cleaning techniques used to enhance image quality, are explained. Some unsupervised clustering algorithms, such as K-means, Hierarchical Cluster Analysis, BIRCH and DBSCAN, applied to group different biological tissues in the MRI exams, are also described in this section. An overview of the developed techniques which have offered the possibility of creating and adding synthetic tissues to the models is present in this section, as the corresponding biological tissues were not correctly segmented after the performance of the clustering algorithms. Finally, the procedure of assigning the biological tissues' dielectric properties to the segmented tissues in the model ends section 4.2, followed by the schematics which summarise the proposed methodology of this dissertation.

The results obtained at each step of the proposed methodology are shown and discussed in section 4.3. Finally, chapter IV closes with the limitations encountered at each step of the designing process of the 3D anthropomorphic phantom generator and some simple conclusions.

### 4.1. Materials

The second part of the project consists of using information and anatomical features provided by digital images to build numerical phantoms of the head and neck region. The phantoms developed in this dissertation are based on MRI exams downloaded from a public archive of medical images of cancer, The Cancer Imaging Archive (TCIA) [113]. In particular, from a “collection” called The Cancer Genome Atlas Head-Neck Squamous Cell Carcinoma (TCGA-HNSC) which includes MRI exams from 16 individuals. Hence different scanner modalities, manufactures and acquisition protocols are available.

I considered multiple protocols such as T1, T1 post contrast, T1 long tau inversion recovery/FLAIR, T1 Turbo Spin-Echo (TSE), T1-weighted FL3D T1 VIBE, T2 Short T1 Inversion Recovery (STIR) and T2 Spectral Attenuation Inversion Recovery (SPAIR). The last two are well known fat-suppression sequences. The features of the MRI exams available in TCGA-HNSC are summarised in Table 4.1. DICOM file format, which is a standard for handling, storing, printing and transmitting information in medical imaging, is the primary file format used by TCIA. In order to visualise and exploit the MRI

data, I used RadiAnt DICOM Viewer, which is a very intuitive software that provides basic tools for image manipulation and measurement.

The manual creation of a mask for later background subtraction, was achieved with Medical Image Segmentation Tool Set (iSEG<sup>®</sup>) software. A high number of software toolkits and toolboxes (e.g. Numpy, Scipy, Scikit-learn from Python<sup>™</sup>, and Statistics and Machine Learning toolboxes from MATLAB<sup>®</sup>) were used for the creation of unsupervised ML algorithms for data segmentation. Furthermore, the open source software platform for medical image informatics, image processing, and three-dimensional visualisation 3D Slicer (version 4.10.1) was used to register different MRI sequences of the same patient.

Table 4. 1: MRI TCGA-HNSC dataset.

| Patient                    | Sequence              | Dimensionality | Acquisition plane | Resolution (mm) |
|----------------------------|-----------------------|----------------|-------------------|-----------------|
| <b>1</b><br>(TCGA-BB-A5HY) | T1 FLAIR              | 2D             | Sagittal          | 0.72 x 0.72 x 4 |
| <b>2</b><br>(TCGA-BB-4228) | T2 with SPAIR (upper) | 2D             | Axial             | 0.72 x 0.72 x 4 |
|                            | T2 with SPAIR (lower) | 2D             | Axial             | 0.72 x 0.72 x 4 |
|                            | T1 post contrast      | 2D             | Axial             | 0.55 x 0.55 x 4 |
| <b>3</b><br>(TCGS-BB-4223) | T1 (upper)            | 2D             | Axial             | 0.89 x 0.89 x 5 |
|                            | T1 (lower)            | 2D             | Axial             | 1.02 x 1.02 x 5 |
| <b>4</b><br>(TCGA-BA-7269) | T1 TSE (upper)        | 2D             | Axial             | 0.57 x 0.57 x 5 |
|                            | T1 TSE (lower)        | 2D             | Axial             | 0.57 x 0.57 x 5 |
|                            | T2 STIR (upper)       | 2D             | Axial             | 1.02 x 1.02 x 5 |
|                            | T2 STIR (lower)       | 2D             | Axial             | 1.02 x 1.02 x 5 |
|                            | FL3D T1 VIBE          | 3D             | Axial             | 0.86 x 0.86 x 2 |
| <b>5</b><br>(TCGA-BA-5557) | T1 TSE                | 2D             | Axial             | 0.57 x 0.57 x 5 |
|                            | T2 STIR               | 2D             | Axial             | 1.02 x 1.02 x 5 |
|                            | FL3D T1 VIBE          | 3D             | Axial             | 0.86 x 0.86 x 2 |

## 4.2. Methodology

The ultimate goal of creating an anatomically realistic phantom generator of the human head and neck region was a very complex process which required multiple intermediate steps. The present section details all the different methodologies attempted in each part of the process. Every decision regarding the construction of the methodology pipeline dictated by the feasibility of 3D printing the resulting models.

Note that I also developed the methodology followed during this part of the dissertation, therefore this section also comprises part of the obtained results. Section 4.3 includes the remaining part of the obtained results, particularly those which come from the application of the developed methodology.

#### 4.2.1. Step 1 - MRI Data Selection

At this point, the anatomical information extracted from MRI exams will be incorporated within the developed models of the head and neck. As my work is focused on using a single MRI exam to create an anatomically realistic model of human head and neck region, the search of the anatomical data stopped as soon as an eligible exam was found. By accessing a public archive in [113], exams of five different subjects were downloaded and examined to check conditions such as: (i) the MRI slices must be parallel to the axial plane as at this plane was easier to identify the structures, (ii) the resolution and signal-to-noise ratio must permit a clear and easy visual identification of the main biological structures<sup>1</sup>. The results of the MRI exam choosing process to create a complete numerical model is discussed in section 4.3.1.

Afterwards, attempts to combine data included in different MRI sequences of the selected patient are also performed as the anatomical information provided by a solo sequence can alone not be sufficient in the construction of an anatomically realistic model. These attempts to combine data using registration techniques are only performed after the determination of the optimal methodology pipeline and the results are analysed and discussed in section 4.3.6.1.

In order to combine the anatomical information across different sequences, registration was used. This process permits the alignment of two or more images with respect to a particular reference image [114]. In this case, I considered the reference images as the MRI sequence with the higher resolution, to preserve as much detail as possible. By using the 3D Slicer software, an affine transformation was performed, in which the lines and parallelism (maps parallel lines to parallel lines) were preserved. Such transformation is obtained by composing a scaling transformation with an isometry, *i.e.* a shape-preserving transformation (in this case, translation in the plane). We use a non-proportional scaling transformation centered at the origin with the form  $(x, y) \rightarrow (ax, by)$ , where  $a, b \neq 0$  are the scaling factors (real numbers) [115]. The scaling factors allow the modification of the original images dimensions to be the same as the reference images. The application of the affine transformation resulted in images with the dimensions and resolution of the reference images, and in the same spatial referential.

The registered and reference images will be exported to MATLAB<sup>®</sup> software where they shall be combined/overlapped. Two different combination processes will be tested in an empirical attempt to quantify the combination of the two images: the addition of the registered and reference images (Test A) and the multiplication of the registered and reference images (Test B). However, both images require previous data cleaning such as background subtraction and filtering, and unsupervised clustering before their combination. The previous steps are all detailed below.

#### 4.2.2. Step 2 - Data Cleaning

The incorporation of medical data in the numerical models required some pre-processing techniques to transform raw data in a more useful and efficient format. In this section, the considered pre-processing steps are presented and detailed.

---

<sup>1</sup> Medical microwave imaging cannot reconstruct an object with resolution lower than 5 mm so any phantom with this resolution as a minimum is adequate.

### i) Data Normalisation

Data normalisation was the first step in the process of data cleaning, which permitted to scale data values in a specific range (in this case, 0.0 to 255.0). The Minimum-Maximum normalisation, in which the maximum value of the original data corresponded to the value 255.0 in the new scale and the minimum value of the original data was replaced by 0.0, was used; the intermediate values were calculated according to Equation (4.1):

$$v' = \frac{v - \min(A)}{\max(A) - \min(A)} (new_{\max(A)} - new_{\min(A)}) + new_{\min(A)} \quad (4.1)$$

where  $v'$  and  $v$  are the new and old values of each pixel respectively;  $A$  is the attribute data, and  $\max(A)$  and  $\min(A)$  are the maximum and minimum values of  $A$ , respectively.  $new_{\max(A)}$  and  $new_{\min(A)}$  are the maximum and minimum values of the new range, respectively [116]. In this case, Equation 4.1 can be given as:

$$v' = \frac{v - \min(A)}{\max(A) - \min(A)} \times 255.0 \quad (4.2)$$

With this step, all the pixels used have values in the same scale.

### ii) Removal of Background

Noise is always present in an MRI image. Background regions can be easily removed by binary masks while preserving the foreground, *i.e.* the body. Therefore, binary masks were manually created using the iSeg software. Firstly, a threshold was applied to the original images, resulting in binary images where the original pixels with values below the threshold were represented with 0's, and the pixels with values above with 1's. This threshold was empirically determined; only one condition was taken into consideration when choosing this value: no pixels outside the body region can be included in the mask. The opposite situation is acceptable as it can be later corrected using the same software. The small gaps in the anatomical region after the application of the threshold were addressed with *Close*, a commonly used morphological operation for image enhancement which allows the connection of objects that are close to each other, *i.e.* smooths the contours, fuses narrow breaks and long thin gulfs, eliminates small holes, and fills gaps on the contours [117]. The final result of this process should be a set of binary images with 1's for all pixels that represent the human body and 0's for the remaining pixels. Finally, by applying the mask to each slice of the original MRI data, the background was removed.

### iii) Filtering Techniques

Four different techniques (detailed in section 2.3.1) aimed at filtering noise and smoothing boundaries in MRI exams, were considered in this study. These techniques include the application of the ideal, Butterworth and Gaussian LP filters, and median filter to the MRI images. Besides testing each filter individually (Option A), filter combinations (Option B) were also applied in order to obtain

the best combination of filters which resulted in better quality images, in other words, images with reduced noise and smoother transitions.

The following pipeline was used: (1) data normalisation and background subtraction of the MRI exam, (2) option A - application of a single filter to the data and, option B - application of the combination of the two best filters (observed in option A) to the data, and (3) application of the K-means algorithm (with  $k = 4$ , for testing purposes) to the processed MRI data.

Step (3) is necessary to visually assess which filter/combination of filters allows the best segmentation of the biological tissues. The choice of the segmentation algorithm (K-means) at this stage was based on previous work developed within the research group. Furthermore, the number of clusters introduced in the K-means are the main groups of tissues expected to be found in the MRI exams (muscle, fat and bone tissue plus the background).

The specifications of the implementation of the filters are detailed below.

### **Ideal LP filter specifications**

The 3D ideal LP filter function, with MATLAB® implementation, only required the  $fc$  parameter, which was normalized to  $[0\ 1]$ . A  $fc$  of 0.6 was used for testing purposes. In the case of good performance of the ideal LP filter, the value of the  $fc$  parameter can be further optimized.

### **Butterworth LP filter specifications**

The digital Butterworth filter transfer coefficients were obtained with the  $[a, b] = \text{butter}(n, \bar{w}_n)$  function from MATLAB®, with  $n = 2$  due the imperceptible ringing effects of order 2 filters.  $\bar{w}_n$  corresponds the cut-off frequency normalized to  $[0\ 1]$ , where 1 corresponds to the Nyquist rate – half the sample rate. A  $\bar{w}_n$  of 50% of its maximum value was chosen for testing purposes. In the case of good performance of the Butterworth LP filter, the value of the  $\bar{w}_n$  parameter can be further optimized. These coefficients along with the input data  $x$  were introduced in  $y = \text{filter}(b, a, x)$  function from MATLAB®, where  $y$  is the filtered data.

### **Gaussian LP filter specifications**

In order to implement the Gaussian filter, the MATLAB® function  $B = \text{imgaussfilt3}(A)$  was used, where  $A$  is the 3D image and  $B$  is the filtered result. This function filters the 3D image  $A$  with a 3D Gaussian smoothing kernel with a standard deviation of 0.5.

### **Median filter specifications**

The median filter was implemented using MATLAB® function  $B = \text{medfilt3}(A)$ , where  $A$  is the input 3D image and  $B$  is the filtered image. This function filters the 3D image  $A$  with a 3-by-3-by-3 filter, which are the neighbourhood dimensions.



### 4.2.3. Step 3 - Unsupervised Clustering

Four different clustering techniques aimed at segmenting the MRI exams were considered in this study. The techniques included: K-means, agglomerative hierarchical, BIRCH and DBSCAN clustering. With these algorithms, the main groups of tissues expected to be clustered were the bone, muscle and fat tissues. Other clusters without an anatomical match were also expected. These should be grouped in one large cluster of body tissue apart from the identifiable main groups. This large cluster will be referred to as mixed tissue, similarly to the tissue of the numerical phantom which represented the mixture of a variable amount of adipose tissue, loose connective tissue, platysma (muscle) and small bones. Hence, the four main groups of tissues expected to be found after MRI clustering include bone, muscle, fat and mixed tissues.

The specifications of the unsupervised clustering algorithms and the clustering quality metrics used in this work are detailed below. Any unsupervised clustering algorithm returns a column vector containing the cluster indices of each point of the entry data. Besides other inputs specified below, the data input of such algorithms must be in a column vector. The inputs of the metrics algorithms are column vectors with the pixel's intensities before the clustering and cluster indices of each data point.

Note that all the clustering quality metrics described in section 2.3.3 and tested in this dissertation express good clustering quality when the clusters are dense and well separated, which means that the objects inside the same cluster should be very close in value and, simultaneously, their values should be distant from the values of the objects of other clusters. However, when analysing the type of the data used in this work (*i.e.* MRI), we understand that it is very likely that the clusters formed in the data are not well separated as voxels' intensity vary within a continuous range of values. Hence, I suspect that the results from the studied metrics do not reflect the quality of the clustering in the MR images studied.

#### K-means clustering specifications

The K-means algorithm was tested in MATLAB®, with `[IDX, C] = kmeans(X, K)` function, which partitions the input data `X` into `K` clusters and returns the vector `IDX` containing the cluster indices of each point, and the `K` cluster centroid locations `C`. By default, `kmeans` function uses the squared Euclidean distance metric.

This algorithm was also tested in Python™, with `KMeans` from `sklearn.cluster` module. The two parameters required for the implementation of this algorithm were the  $k$  number of clusters and the input data.

In both cases, the algorithms required the input and the number of clusters, which were varied from 4 to 7. Clustering quality metrics described in section 2.3.3 were used for  $k$  parameter optimization.

#### Agglomerative hierarchical clustering specifications

The agglomerative hierarchical algorithm was implemented in Python™, therefore `AgglomerativeClustering` was imported from `sklearn.cluster` module. The two parameters required for the implementation of this algorithm were the  $k$  number of clusters and the type of linkage metric. Similarly to K-means, several  $k$ 's, from 4 to 7, were tested in order to obtain the optimal value for this parameter.

## **BIRCH specifications**

The BIRCH algorithm was tested in Python™ using `Birch` imported from `sklearn.cluster` module. The three parameters required for the implementation of this algorithm were the threshold, which limits the distance between the entering sample and the existing subcluster, the number of clusters, and the branching factor, which limits the number of subclusters in a node. The  $k$  number of clusters was set to 7 and the threshold was set to its default value of 0.5.

Additionally, several values for the branching factor, from 2 to 30, were tested in order to choose which one provided better visual separation of the anatomical structures under study. In order to select the optimal branching factor, a clustering evaluation metric was used.

## **DBSCAN specifications**

This algorithm was tested in Python™ using `DBSCAN` imported from `sklearn.cluster` module. The two parameters required for the implementation of this algorithm were the `Eps` and the `MinPts`, which were varied with a coarse grid-search approach from 0.01 to 10 and 10 to 500, respectively. In order to select the optimal combination of parameters, a clustering evaluation metric was used.

## **Silhouette coefficient specifications**

The silhouette coefficient was implemented both in MATLAB®, using the function `silhouette` of the Statistics and Machine Learning Toolbox, and in Python™, using `silhouette_score` imported from `sklearn.metrics` module. The output from the Python™ is the mean value of the silhouette coefficient of each data point and the MATLAB® function returns the silhouette values of all data points. In order to compare the coefficients obtained from MATLAB® and Python™, the average of the MATLAB® output was used.

## **Davies-Bouldin index specifications**

The DBI was implemented in Python™, using `davies_bouldin_score` imported from `sklearn.metrics` module. The output of this metric is the mean value of the DBI of each cluster. Here, the computation of the DBI is simpler compared to the silhouette coefficient, however the distance metric is limited to Euclidean space. Zero is the lowest possible value for DBI; values similar to zero indicate a better partition of the data [97].

## **Calinski-Harabasz index specifications**

The CHI was implemented in Python™, using `calinski_harabasz_score` imported from `sklearn.metrics` module.

#### **4.2.4. Step 4 – Synthetic Tissues Insertion**

Although MRI is a vital tool to screen the body, there are tissues which are easier to identify in these exams rather compared others. The size of the tissues is a decisive factor for its detection. Generally, CLNs are very small biological structures extremely hard to identify in MRI exams, even for trained eyes. Therefore, there is the possibility that the segmentation algorithms are not able to identify clusters corresponding to CLNs.

Moreover, I suspect that the segmentation algorithms applied would not be able to correctly detect and assign the skin tissue to a single cluster over the body surface as this organ has a very thin thickness compared to the MRI resolution and the contrast of the images can make the identification and segmentation of this tissue difficult in its extension.

The synthetic tissue insertion step includes the development of algorithms to manually insert in the anatomically realistic phantoms the synthetic tissues missing or wrongfully identified in the segmented MRI exams provided by the unsupervised clustering step.

##### **Skin insertion**

The algorithm to generate a synthetic layer of skin to outline the body boundary will be included in the phantom generator. Its inputs are the volume of binary masks previously calculated for background subtraction and the expected thickness of the skin layer, which is fixed to 1.4 mm according to [109]. At each slice of the transverse plane, *i.e.* at each imaginary plane that divides the body into superior and inferior parts, this algorithm determines the position where the mask pixels change in value between 0, for background, and 1, for body region. Then, the synthetic layer of skin is introduced at the surface of the body region towards the interior of the body. By applying this algorithm in both directions of the image, a continuous synthetic layer of skin is added over the whole-body surface.

##### **LN insertion**

I used the model of the LNs developed for the 3D numerical phantom generator, detailed in Chapter III, to include synthetic LNs in the anatomically realistic phantoms. Such algorithm allowed the user to choose the number of LNs introduced in the phantom, and their size, location in levels and medical state.

The placement of the LNs into the levels required a thorough study of the anatomy in order to identify, in the MRI scans, all the structures that define the frontiers of the levels. As the limits of the levels vary between slices, the determination of these frontiers is a procedure with several approximations and simplifications.

#### **4.2.5. Step 5 – Dielectric Properties Assignment**

An objective of this dissertation was the creation of anatomically realistic models of the human head and neck, which include the dielectric properties of the tissues within the region under study. Hence, I studied the variation of these tissues' properties. The models created within the scope of this dissertation are compatible with future image studies that use FDTD modelling to model the propagation of the electromagnetic waves in biological tissues, at microwave frequencies.

As Cole-Cole models offer a suitable approach for representing the frequency variation of many biological tissues at frequencies used for medical MWI, they will be implemented. In particular, the 4-Cole-Cole model, which is considered the best fitting technique as it describes the four relaxation mechanisms exhibited by biological tissues in a frequency range of 10Hz to 100 GHz [108]. Initially, to assign dielectric properties to MRI derived models, four dielectric properties curves for permittivity and conductivity were considered: a curve for skin, bone, fat and muscle tissue. In order to account for the dielectric differences within bone, fat and muscle tissue due to physiological processes, a dielectric variation of 5% with respect to the nominal property was incorporated [118] – except for skin. Thus, seven curves of the dielectric properties were obtained: one for the skin tissue, and two curves which limit the lower and upper bound for the bone, fat and muscle tissues. Although the curves cover a large range of frequency, only the range of interest for medical MWI (1-10 GHz) is depicted in Figure 4. 1. The 4-Cole-Cole parameters for each curve are shown in Table C1 of Appendix C [118].

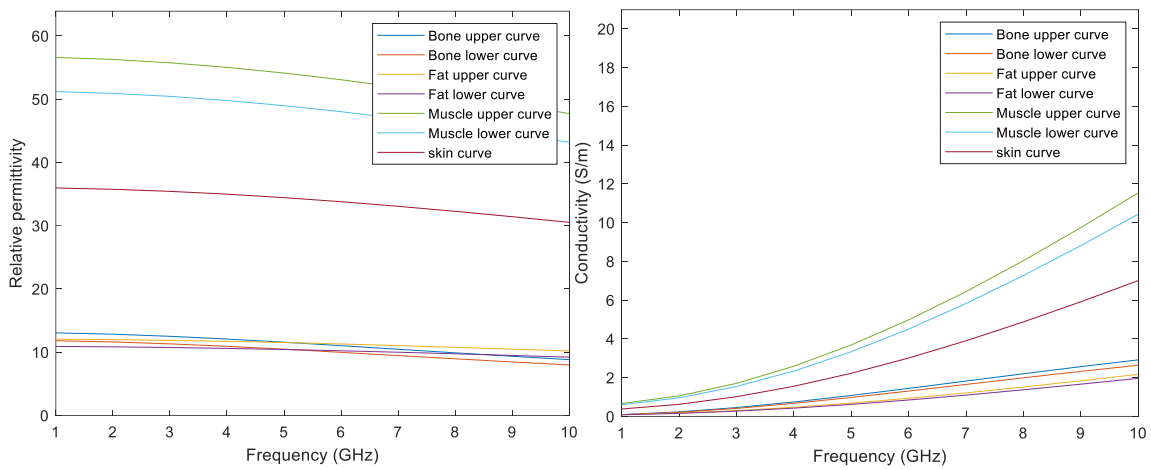


Figure 4. 1: Dielectric properties curves considered to assign the dielectric properties to the tissues in the cervical region, which are represented in the developed models and phantom generator. The graph on the left depicts the permittivity curves, and the graph on the right shows the conductivity curves, for the considered biological tissues. Both curves were obtained by using the 4-Cole-Cole formulation with the parameters given in [118].

Healthy and malignant lymph nodes were modelled according to the values obtained by Ricardo Eleutério in [119] as the 4-Cole-Cole parameters for these tissues are not available elsewhere. The parameters used to model the LNs refer to the Debye model, however we have already observed that the Debye model is a simplification of the Cole-Cole model, hence the Debye parameters were used to define 1<sup>st</sup> pole of the Cole-Cole model and the 2<sup>nd</sup>-3<sup>rd</sup>-4<sup>th</sup> poles were assumed to be null in the 4-Cole-Cole model. The parameters are shown in Table C2 of Appendix C, and Figure 4.2 depicts the four curves of the dielectric properties of the healthy and metastasised LNs, both cross-section and surface. Similarly, this figure only covers the frequency range of interest for medical MWI.

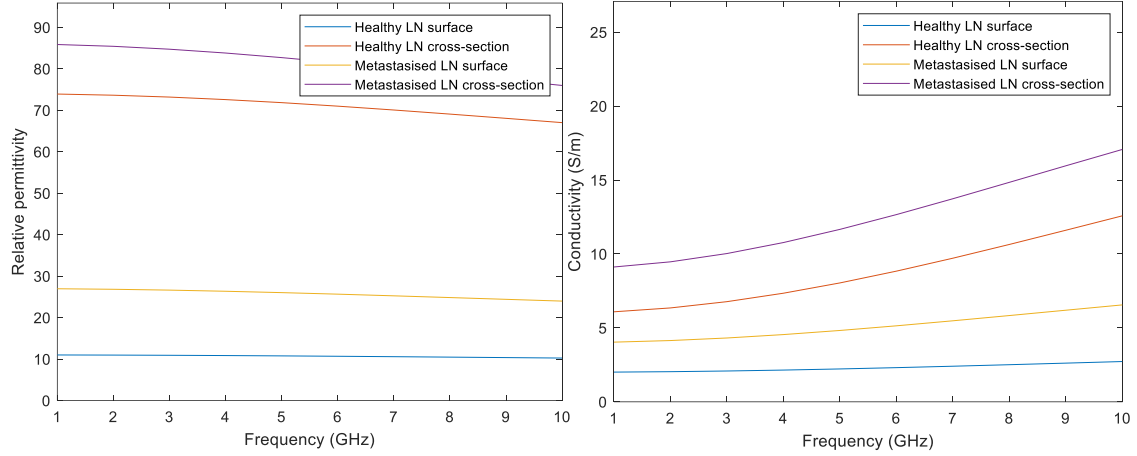


Figure 4. 2: Dielectric properties curves considered to assign the dielectric properties to the LNs which are inserted in the developed models. The graph on the left depicts the permittivity curves, and the graph on the right shows the conductivity curves, for the healthy and unhealthy cross-section and surface of the LNs. Both curves were obtained by using the 4-Cole-Cole formulation with the Debye parameters given by [119]. The missing 4-Cole-Cole parameters were assumed to be null.

The developed algorithm, which allows the assignment of the dielectric properties, provides two matrices, one for each dielectric property, with the same dimensions as the phantom. For each matrix, the voxels contain the dielectric property value, for a user specified frequency, corresponding to each voxel of the anatomically realistic model. In order to obtain this, several steps occur: (1) For each cluster with a segmented tissue, the maximum and the minimum value of the intensity of the original MRI exam is determined, (2) These maximum and minimum intensity voxels are associated with the upper curve and the lower curve of the tissue, respectively, (3) The remaining voxels of the same cluster are linearly mapped to a value between the curves of that tissue. This methodology was inspired by Zastrow *et al.*[120]. As the mixed tissue consists of a mixture of multiple tissues such as adipose, loose connective, muscle and bone tissues, I set the muscular tissue and the adipose tissue curves as the upper and lower curve of this type of tissue, respectively. This way, I was able to cover the dielectric properties variability of all tissues included in this cluster.

#### 4.2.6. Methodology Overview

The methodology developed in this dissertation can be very complex to summarise, therefore Figure 4.3 depicts, in a simplistic way, all the steps of the process and all the techniques tested at each step.

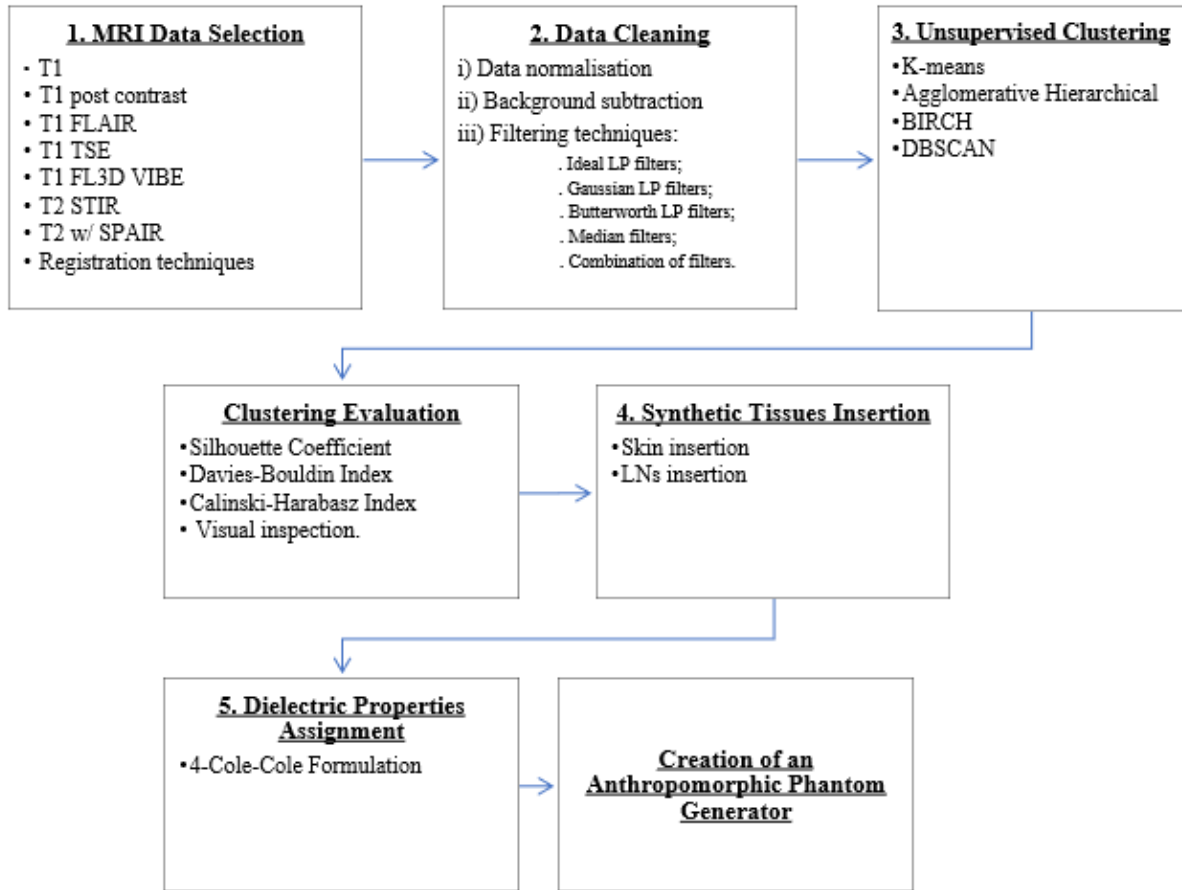


Figure 4. 3: Illustration of the methodology steps followed during this dissertation.

## 4.3. Results and Discussion

Within this section, the results of steps 1 to 5 described above are presented and discussed. For purposes of organization given the several tests performed to build the anthropomorphic 3D phantom generator, the results obtained will be discussed at each step of the process in order to begin an elimination process of tests that underperform until reaching the optimal image processing methodology and machine learning algorithms for clustering. The tailored pipeline will be used in the creation of the final 3D numerical model. This model serves as input to the developed phantom generator of the head and neck region.

### 4.3.1. Step 1 - MRI Data Selection

In this work, I evaluated MRI exams of five different patients whose clinical data was acquired using different protocols. As mentioned in section 4.2.1, MRI exams of the axial plane with a resolution and signal-to-noise ratio which permitted a clear and easy visual identification of the main biological structures, were preferred.

In patient 1, only axial T1 FLAIR exams were available. The exams of this patient were discarded because only the upper region of the head and neck, mainly head, was imaged.

In patient 2, both axial T1 post contrast and axial T2 with SPAIR exams were available. T2 exams are divided in sets of slices from the upper and lower region of the head and neck. Both sets contain slices with the same resolution.

Axial T1-weighted MRI exams were available for patient 3, but the upper and lower region were imaged with different resolutions,  $(0.89 \times 0.89 \times 5)$  mm and  $(1.02 \times 1.02 \times 5)$  mm, respectively. The exams of patient 3 were discarded due to the different resolutions between the upper and lower slices of the head and neck, which would only increase the difficulty in data processing.

Both patient 4 and 5 included exams with axial T1 TSE, axial T1 FL3D VIBE and axial T2 STIR sequences, with a resolution of  $(0.57 \times 0.57 \times 5)$  mm,  $(0.86 \times 0.86 \times 2)$  mm and  $(1.02 \times 1.02 \times 5)$  mm, respectively.

Patients 2, 4 and 5 were compared, with preference to choose the images with the highest resolution in all anatomical planes. Through comparison, I observed that the differences of resolution in sagittal and coronal planes between all scans are not as significant as the differences of resolution in the axial plane. Therefore, T1 FL3D VIBE sequences have been chosen over the others given their significant higher resolution in the axial plane. As T1 FL3D VIBE sequences of patients 4 and 5 have the same resolution, a visual inspection to choose the exam from which it was possible perceive more anatomical information was performed. Based on the scans shown in Figure 4.4, I chose to use the T1 FL3D VIBE scans of patient 5 to develop the phantom generator, because it was easier to identify the biological structures in the exams of this patient rather than patient 4.

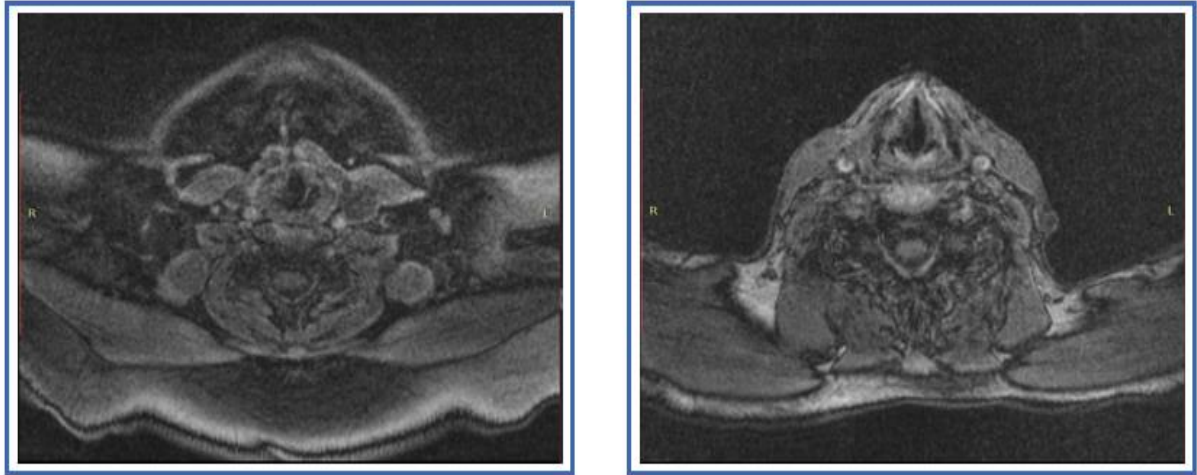


Figure 4. 4: Scans of patients 5 and 4, on the left and right, respectively. In both figures, the axial plane of the cricoid cartilage was considered, for comparison purposes.

The MRI exam chosen to represent the anatomically realistic model consists of 96 axial slices with  $240 \times 256$  pixels, with 16-bit grayscale format. The region of interest is comprised between slices 23 and 80, therefore only 58 axial slices will be considered in this dissertation.

The size of the voxels corresponds to the resolution of the 3D data, hence, the original-shaped voxels from the chosen MRI exam have a shape of a quadrangular prism, with 4 rectangular surfaces with dimensions  $(0.86 \times 2)$  mm, and squares of size  $(0.86 \times 0.86)$  mm in the base. Thus, the chosen exam has a resolution of  $(0.86 \times 0.86 \times 2)$  mm.

The original-shaped voxels have a z-dimension larger than the double of its x- and y-dimension, hence the anatomical structures were represented with half of their real volume due to the elongated (in the z axis) shape of the voxels. In order to change the shape of the voxels, each one was divided into two almost cubic voxels with size  $(0.86 \times 0.86 \times 1)$  mm - the pseudo-cubic transformed voxels.

Hence, the performance of the segmentation algorithms in 2D images (the axial slices of the 3D data with pixels of size  $0.86 \times 0.86$  mm) and in 3D data with original-shaped voxels and pseudo-cubic transformed voxels was compared in Data Cleaning step.

#### **4.3.2. Step 2 – Data Cleaning**

Data cleaning steps i and ii normalise the values of the data from 0 to 255 and change the values of the background region to 0.

In order to determine the filter or the combination of filters that optimize the image processing methodology, a test was designed to compare the results from K-means clustering after the application of different filtering techniques (step iii - detailed in section 4.2.2).

##### **Option A**

In Option A, all filters mentioned in 2.3.1 (*i.e.* ideal, median, Butterworth and Gaussian) were tested, using the following pipeline: (1) data normalisation and background subtraction of the original MRI data, (2) application of a single filter to the data, and (3) application of the K-means algorithm (with  $k = 4$ ) to axial slices of the 3D data and to the whole 3D data with both original-shaped voxels and pseudo-cubic transformed voxels.

With Option A, I determined which filters provide the best results in terms of removing noise and smoothing the edges' sharp transitions of the data. Besides, I was also able to assess the performance of the K-means algorithm in segmenting slice per slice versus segmenting the whole volume of the 3D MRI data with original-shaped voxels and pseudo-cubic transformed voxels. The results of Option A are shown in Figures 4.5 – 4.8.



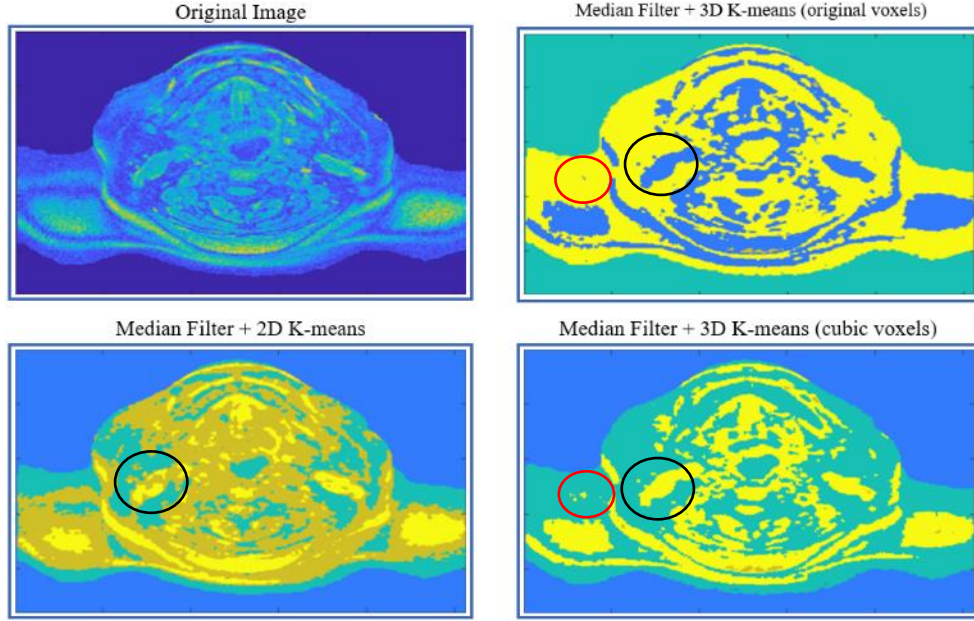


Figure 4. 5: Axial slice of the normalised MRI exam after background subtraction is represented at the top left. Results obtained (the same axial slice is shown) after applying the median filter and a 2D K-means segmentation of the axial slice (bottom left), 3D K-means segmentation of the original-shaped voxels (top right) and the 3D K-means segmentation of pseudo-cubic transformed voxels (bottom right). The right sternocleidomastoid muscle is located within the black circles and the red circles indicates areas with small-sized granularities.

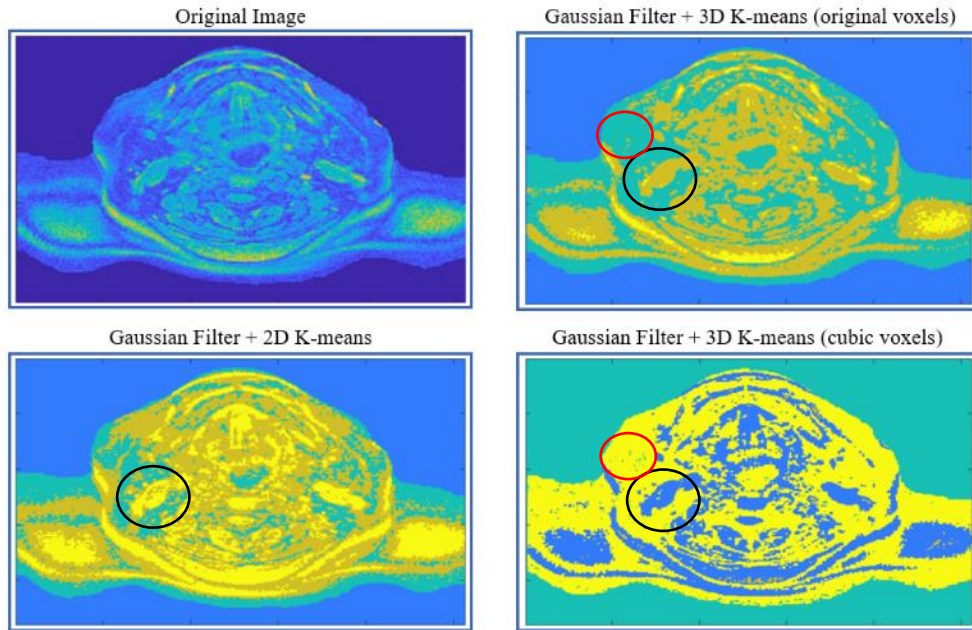


Figure 4. 6: Axial slice of the normalised MRI exam after background subtraction is represented at the top left. Results obtained (the same axial slice is shown) after applying the Gaussian LP filter and a 2D K-means segmentation of axial slices (bottom left), 3D K-means segmentation of the original-shaped voxels (top right) and 3D K-means segmentation of the pseudo-cubic transformed voxels (bottom right). The right sternocleidomastoid muscle is located within the black circles and the red circles indicates areas with small-sized granularities.

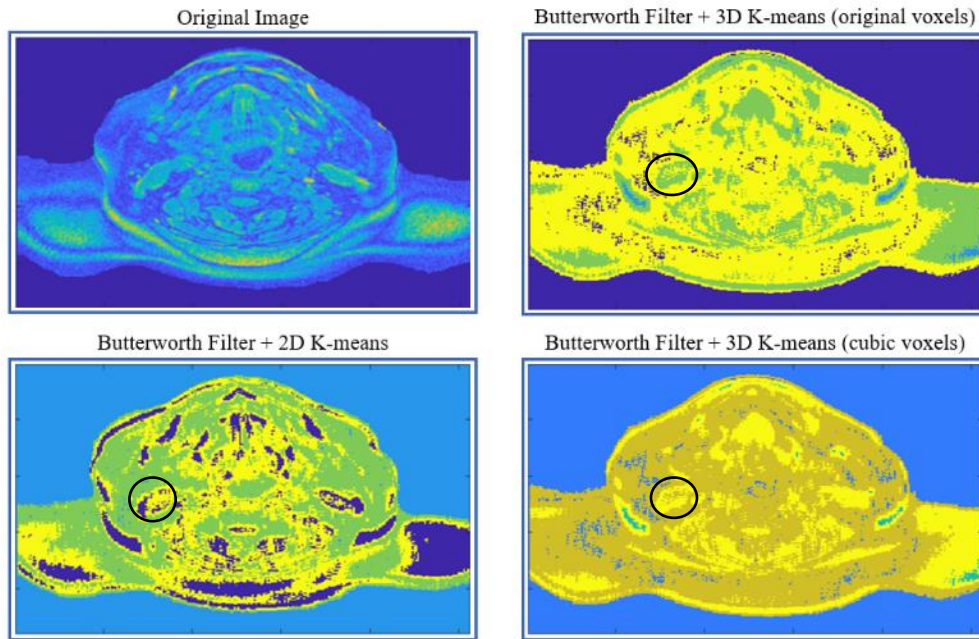


Figure 4. 7 : Axial slice of the normalised MRI exam after background subtraction is represented at the top left. Results obtained (the same axial slice is shown) after applying the Butterworth LP Filter ( $n=2$ ) and a 2D K-means segmentation of axial slices (bottom left), 3D K-means segmentation of the original-shaped voxels (top right) and 3D K-means segmentation of the pseudo-cubic transformed voxels (bottom right). The right sternocleidomastoid muscle is located within the black circles.

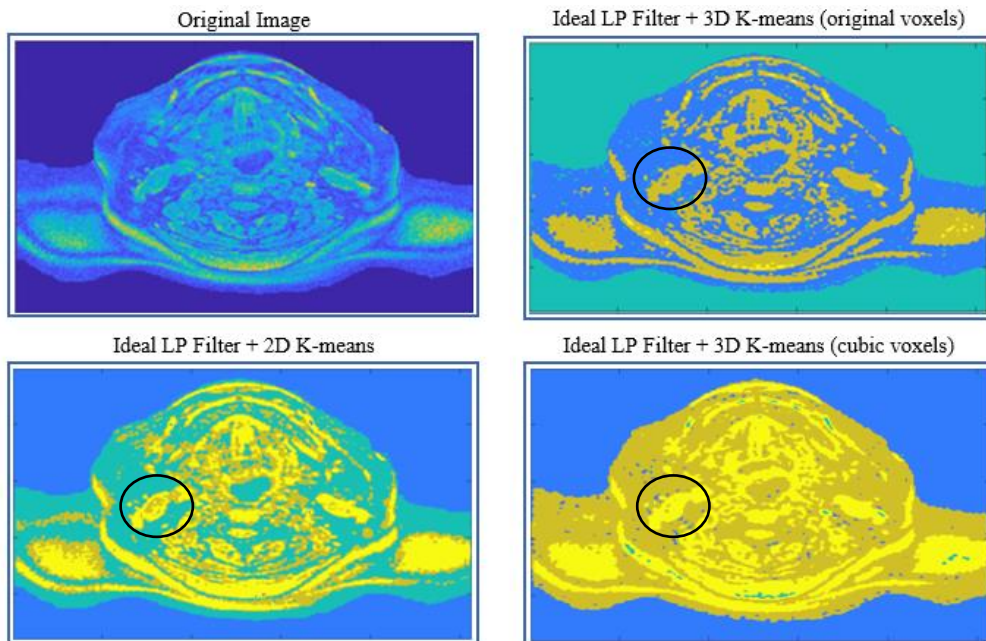


Figure 4. 8: Axial slice of the normalised MRI exam after background subtraction is represented at the top left. Results obtained (shown in the same axial slice) after applying the ideal LP filter and a 2D K-means segmentation of axial slices (bottom left), 3D K-means segmentation of the original-shaped voxels (top right) and 3D K-means segmentation of the pseudo-cubic transformed voxels (bottom right). The right sternocleidomastoid muscle is located within the black circles.

Regarding the performance of the K-means algorithm in segmenting slice per slice versus segmenting the whole volume of the 3D MRI data with original-shaped and pseudo-cubic transformed voxels, I observed more irregular edges and a higher number of clusters without anatomical correspondence (as observed in Figures 4.5 – 4.8 with a black circle over the right sternocleidomastoid muscle) when the algorithm was applied to slices rather than the whole 3D dataset. Therefore, the methodology pipeline should be applied to the whole 3D dataset.

Blurring and ringing properties are characteristics of ideal LP filters, whose effects intensify as the amount of high frequency content removed increases. In order to eliminate the small-sized granularities present in the images in Figure 4.8, a low cut-off frequency should be considered. Although a low cut-off frequency allows to smooth the edges, ringing artifacts would also be added to the images. Since a good balance between these characteristics was not achieved, the ideal LP filter was excluded from the methodology pipeline.

Results from the filtering test with Option A demonstrated both severe blurring and presence of numerous small-sized granularities in the case of the Butterworth LP filter, Figure 4.7. The granularities resulting from Butterworth LP filtering could be minimised by removing the high frequency content, but the resulting blurring of the structures causes loss of anatomical information. Therefore, the Butterworth LP filters were excluded from the methodology pipeline.

Conversely, median LP filters were proved to be best for smoothing edges and Gaussian LP filters were very effective in removing noise, as shown in Figures 4.5 and 4.6, respectively. Besides, the K-means segmentation algorithm applied after these filtering techniques provided the separation of large structures with less fine detail, which is preferable for 3D printing. Note that to 3D print, anatomical structures must fit with one another, otherwise they become “loose” after printing takes place.

The visual comparison between the results from the segmentation of 3D MRI data with the original-shaped voxels and the pseudo-cubic transformed voxels allowed to conclude that, in the second case, additional granularities were being added (as observed in Figures 4.5 and 4.6 within red circles). This can be attributed to the fact that the process of doubling the number of slices effectively results in enlarging the clusters in the axial direction. Very small-sized clusters that would have been not perceptible before, especially among pixels that correspond to the same tissue, are now not negligible and can be easily seen in the images. Noisy points that were not completely removed by the filters can end up in these observable small-sized clusters. Besides, the doubling of the data implies the increase of computational cost. Consequently, only the original-shaped 3D MRI data will be used in future tests.

## **Option B**

From the filtering test with Option A, I concluded that both median and Gaussian LP filters provided improved results in noise removal and edge smoothing compared to ideal and Butterworth LP filters. Option B allows the comparison between the performance of the above-mentioned single filters and their combination. The following pipeline was used: (1) data normalisation and background subtraction of the 3D MRI data with the original-shaped voxels, (2) application of Gaussian or median LP filters, and their combination, and finally, (3) application of the K-means clustering algorithm (with  $k = 4$ ) in the 3D data with original-shaped voxels. Figure 4.9 depicts the obtained results.



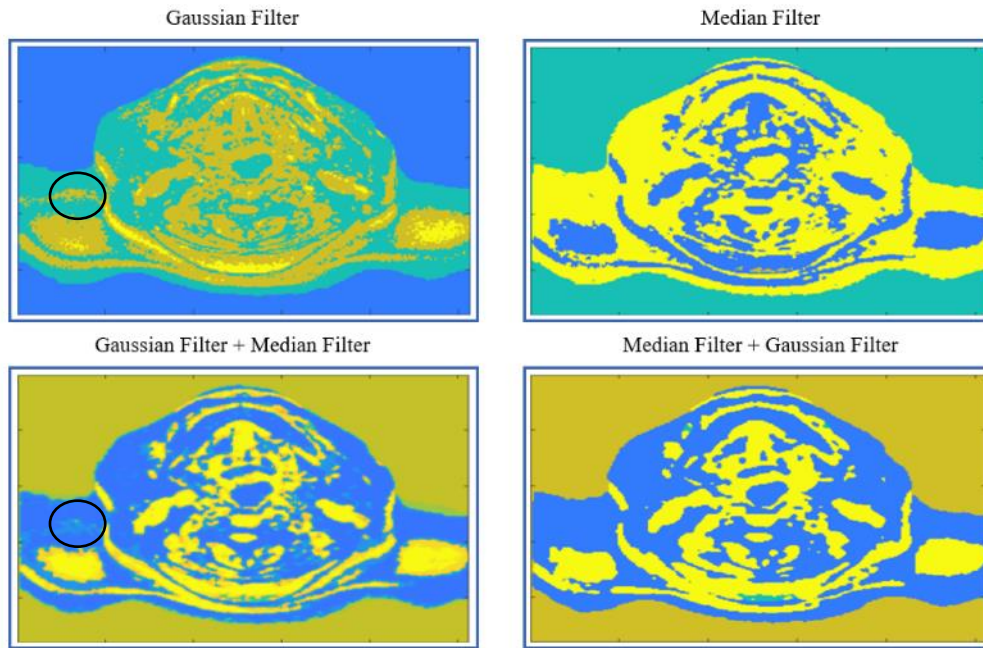


Figure 4. 9: Results of the filtering test with Option B – the combination of the best filters yielding from Option A. Application of the Gaussian and median filters alone, and the combination of the Gaussian filter followed by the median and the median filter followed by the Gaussian filter, from left to right and top to bottom, respectively. The black circles indicate regions with small-sized granularities.

The application of the Gaussian filter and the combination of Gaussian filter followed by median filter resulted in small-sized granularities (for example, as observed in Figure 4.9 within the black circles), which are not well-suited for 3D printing. Consequently, these alternatives were dismissed from the data processing pipeline. The combination of the median filter followed by the Gaussian filter resulted in smoother edges and less small-sized clusters, when compared to the application of the median filter alone. Therefore, the combination of the median filter followed by the Gaussian filter was included in the data processing pipeline as it allowed the best anatomical information retrieval and a printer-friendly model.

### 4.3.3. Step 3 - Unsupervised Clustering

As pre-processing data methodology was discussed and established, the following step concerns the segmentation of the MRI data in a more meaningful representation, *i.e.* grouping the data objects with similar characteristics, which hopefully will translate into groups of biological tissues. The performance of four different algorithms were tested in the 3D data: K-means, Agglomerative Hierarchical, BIRCH, and DBSCAN.

#### DBSCAN:

Due to memory constraints/errors in MATLAB®, DBSCAN algorithm was tested in an axial slice of the 3D data, in Python™. The two parameters required for the implementation of this algorithm were the Eps and the MinPts, which were varied in a search-grid search from 0.01 to 10 and 10 to 500. A grid search of both parameters was performed in order to find the combination which provided better

separation of the anatomical structures. The results showed that for  $Eps \leq 0.2$ , the resulting number of clusters varied from 1 to 187, with the highest number of clusters related to the smaller values of the MinPts parameter. For  $Eps > 0.2$ , the resulting number of clusters varied from 2 to 4, over the entire range of MinPts (10 – 500). After the application of the DBSCAN, the silhouette coefficient was calculated for each combination of parameters. In theory, the highest the score of the metric, the better the segmentation results.

The highest value of the cluster quality metric silhouette ( $s = 0.983$ ) was obtained for the combination of  $Eps = 0.2$  and  $MinPts = 30$ , which resulted in 162 clusters. For a number of clusters similar to the number of the main biological tissues found in the head and neck region obtained with  $Eps = 0.05$  and  $MinPts = 415$ , the value of the silhouette metric was 0.222. The results of DBSCAN algorithm for each case are shown in Figure 4.10.

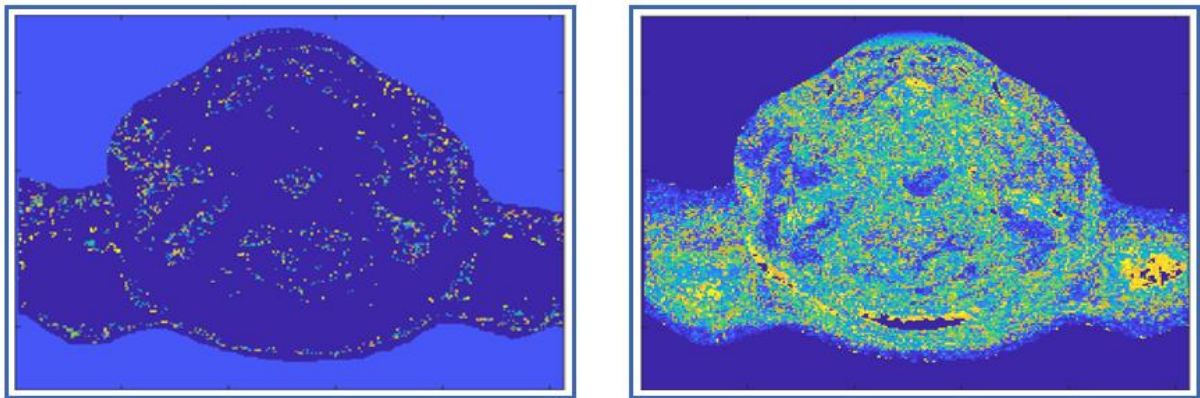


Figure 4. 10: DBSCAN clustering results of a slice of the 3D MRI data: 6 and 162 clusters, from left to right.

For DBSCAN clustering method two different scenarios were assessed: an option in which the chosen number of clusters is similar to the number of the main tissues found in the human head and neck: 6 clusters, and the case for which the best score of the metric was obtained. In the first case, the results of the segmentation do not allow the extraction of any kind of anatomical information whereas the second scenario shows shapes of some known anatomical structures, although the image contains a vast number of small-sized clusters that have no clear anatomical meaning. Therefore, DBSCAN method is not suitable for segmenting MRI scans of the cervical region nor for 3D printing.

If we revisit the definition of DBSCAN in section 2.3.2, it is based on a density-based algorithm which separates dense regions from sparse regions of data points. In the case of the MRI data, DBSCAN is not focused on the density of the regions but on the intensity of the pixels. The histogram of the MRI data used in this work is shown in Figure 4.11. It divides the range of intensity values of the voxels in several series of intervals, on the horizontal axis, and counts the number of voxels which fall into each interval. Thus, we can observe that the MRI data comprise a continuous range of voxels intensity and the number of voxels monotonically decreases for higher values of intensity. As the histogram does not exhibit a behaviour of large amounts of voxels around specific values of intensity, alternated with low amounts of voxels in the in-between intensities, density-based methods can hardly find new clusters apart from the clusters corresponding to background and foreground. For this reason, I believe that DBSCAN is not appropriate to segment the MRI data.

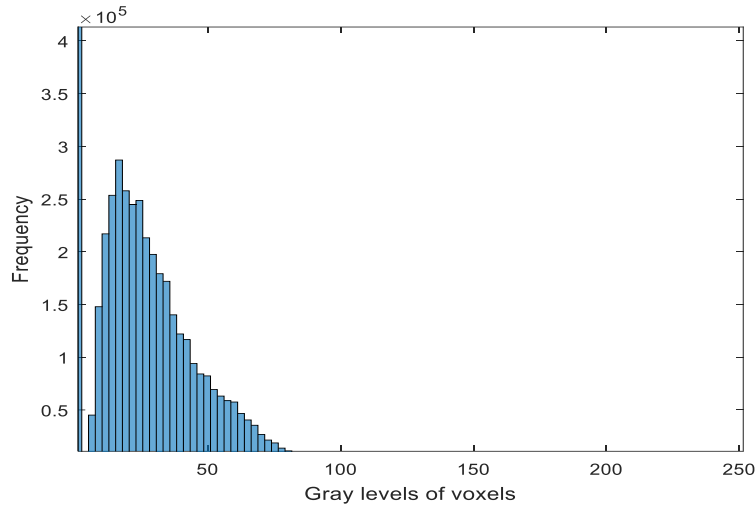


Figure 4. 11: Histogram of the gray levels of MRI data after normalisation and background subtraction.

### **BIRCH:**

For testing purposes, the BIRCH algorithm was tested in an axial slice of 3D data, in Python™. The three parameters required for the application of this algorithm were the branching factor, the number of clusters, and the threshold, where the last two parameters were set to 7 and 0.5, respectively.

As the threshold parameter represents the maximum radius of a subcluster, a low value for this parameter promotes the creation of a higher number of subclusters, which can potentially be later corrected with manual combination of clusters according to the knowledge of the anatomical region under study. The number of clusters used for this algorithm was a little higher than the expected five groups (background, muscle, adipose, bone and mixed tissue) resulting in the subsequent combination of clusters. The opposite strategy may lead to large clusters that include multiple tissue types.

Several values for the branching factor, from 2 to 30, were tested in order to choose the one which provided better visual separation of the anatomical structures. In order to select which branching factor to use, the silhouette coefficient was calculated for each. The highest value of the silhouette metric ( $s = 0.707$ ) was obtained for a branching factor of 6. The resultant segmented image with 7 clusters included small granularities, which are not suitable for 3D printing, and multiple clusters with irregular edges that represent the same biological tissue. For example, in Figure 4.12 (on the left), the olive green and the dark blue clusters are both muscle tissue and the small-sized yellow clusters within the aqua-green clusters represent adipose tissue (as observed within the red circle). Combinations of these clusters were performed, which resulted in the segmented image on the right of the Figure 4.12. However, the results are not quite satisfactory since there is little anatomical information that can be extracted from that image.

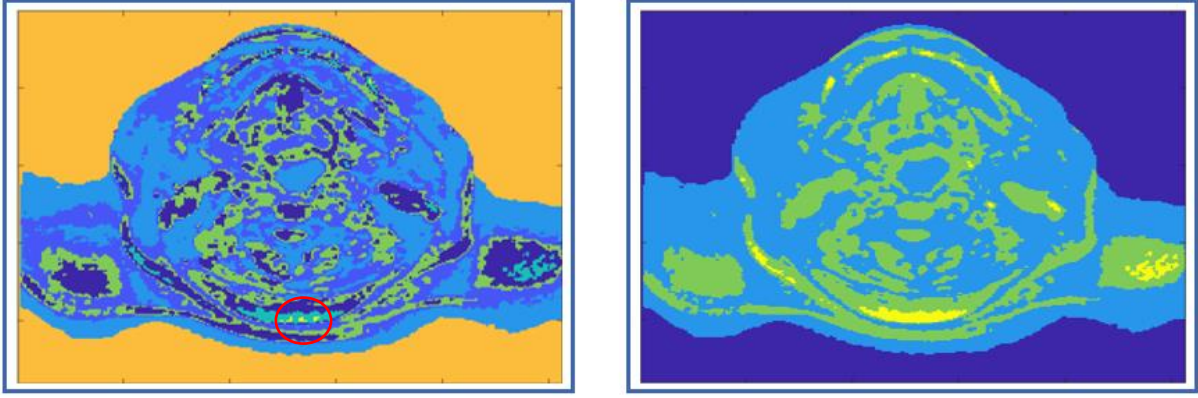


Figure 4. 12: Segmented image ( $k = 7$ ) after the application of the BIRCH clustering algorithm, on the left. Final image ( $k = 4$ ) resulting from the manual combination of clusters that likely represent the same tissue type, on the right.

A secondary approach to improve the results consisted on applying the BIRCH algorithm with the same initial parameters as before, except the number of clusters, which was increased to 10. The increase of the number of clusters will prevent different tissues from being included in the same cluster but will also separate in different clusters tissues with the same biological nature. However, this was corrected with manual combination of clusters based on anatomical knowledge. The primordial segmented image and the altered segmented image was shown in Figure 4.13.

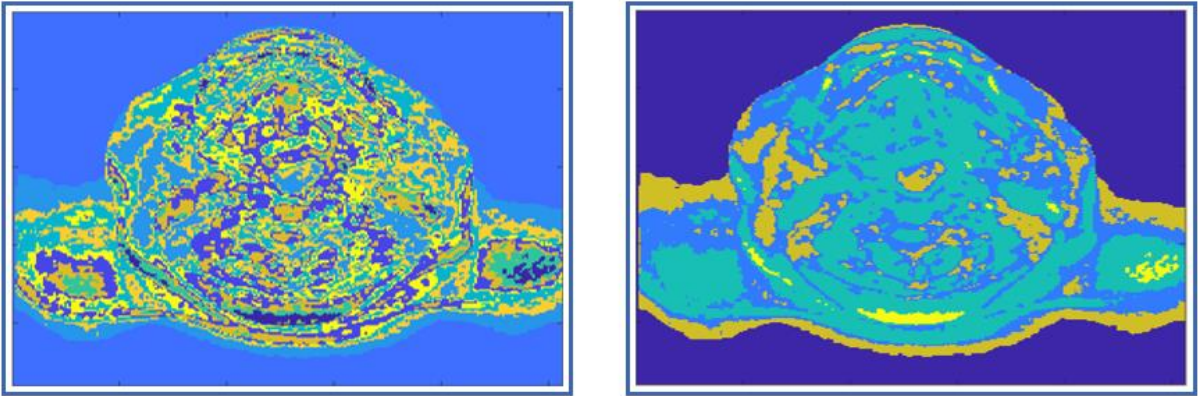


Figure 4. 13: Segmented image ( $k = 10$ ) after the application of the BIRCH clustering algorithm, on the left. Final image ( $k = 5$ ) resulting from the manual combination of clusters that represent the same tissue type, on the right.

Despite obtaining a higher number of clusters after using the combination strategy in the initial segmented images with  $k = 10$  compared to the initial segmented images with  $k = 7$ , the 5 final clusters showed on the right image of Figure 4.13 do not have explicit anatomical meaning. Besides, the presence of several granularities, which are an obstacle for 3D printing, prevents the BIRCH algorithm to become the chosen technique for segmenting the head and neck MRI scans.

BIRCH algorithm is designed to identify sparse and dense regions, and hence discover the overall distribution patterns or the correlations among data points, *i.e.* it takes advantage of the fact that data space is generally not uniformly occupied, and hence not every data point is equally important for clustering purposes [121]. As shown in the histogram of Figure 4.11, the MRI data does not have density



varying regions (*i.e.* large amounts of voxels around specific values of intensity, alternated with low amounts of voxels in the in-between intensities), thus BIRCH algorithm is not well-suited for segmenting the MRI images.

The BIRCH algorithm was also tested in the whole volume of the MRI data, for  $k = 7$  and  $k = 10$  with a branching factor of 6 and a threshold of 0.5, but the results were similar to the ones obtained from the application of this algorithm to the axial slices of the 3D MRI data. Due to space constraints, the results obtained are not presented in this dissertation.

### **Agglomerative Hierarchical:**

Due to memory errors in MATLAB®, this algorithm was tested in an axial slice of the 3D data in Python™. The two parameters required for the implementation of this algorithm were the  $k$  number of clusters and the type of linkage metric. The usage of the Ward linkage is common to multiple studies of MRI clustering using the hierarchical method [122] [123] [124], hence, I chose to work with this linkage metric.

Several values of  $k$  were tested in order to obtain the optimal value for this parameter. The variation of  $k$  was set in the range of values from  $k = 4$  to  $k = 7$ . The minimum value of the  $k$  parameter is the minimum number of tissues expected to be found (background, muscle, bone and fat tissues), and the maximum value corresponds to a value that allows a finer separation of tissues, which can be later manually combined into more anatomical meaningful clusters. For  $k > 7$ , the segmented images showed excessive details which hinder the segmentation of well-known anatomical structures. The optimal value of  $k$  was achieved through the determination of the silhouette coefficient for each case. The obtained segmented images and the values of the metric, for each case, are depicted in Figure 4.14 and Table 4.2, respectively. Images from the scenarios a) to d) correspond to  $k$  values from 4 to 7, respectively.

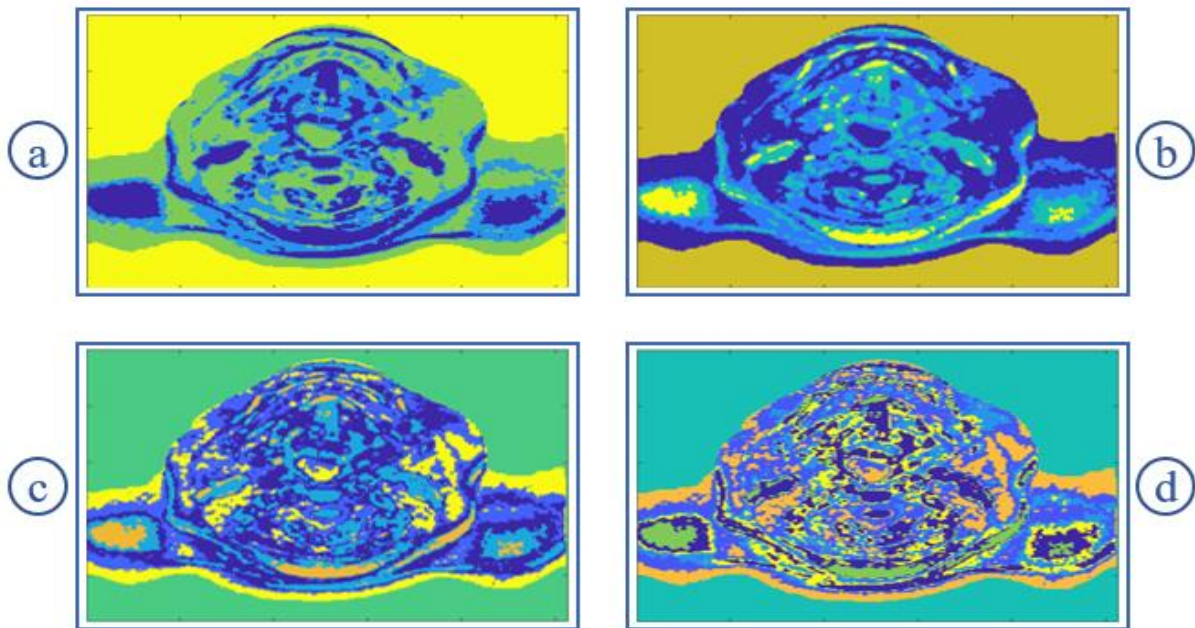


Figure 4. 14: Segmented images after the application of the agglomerative hierarchical clustering algorithm, with different  $k$  numbers of cluster. a)  $k = 4$ , b)  $k = 5$ , c)  $k = 6$  and d)  $k = 7$ .



Table 4. 2: Values of the silhouette coefficient calculated for each segmented image obtained from Agglomerative Hierarchical clustering with varying  $k$  number of clusters from 4 to 7.

| Scenario | $k$ | Silhouette Coefficient |
|----------|-----|------------------------|
| a)       | 4   | 0.238                  |
| b)       | 5   | 0.109                  |
| c)       | 6   | 0.117                  |
| d)       | 7   | 0.116                  |

Visual examination of the segmented images resulting from the application of agglomerative hierarchical clustering in Figure 4.14, and consequent anatomical information retrieval were very promising, however the values of the metric in Table 4.2 disagree with these as they fall very far from the score of 1.

Given the inconclusive results of the silhouette coefficient in Table 4.2, other metrics designed to evaluate the clustering quality of unsupervised methods, such as the Davies-Bouldin and Calinski-Harabasz indexes, were calculated and presented in Table 4.3, so that these could help determine the optimal  $k$ .

Table 4. 3: Values of the silhouette coefficient, and Davies-Bouldin and Calinski-Harabasz indexes calculated for each segmented image from scenario a) to d), obtained from Agglomerative Hierarchical clustering with varying  $k$  number of clusters from 4 to 7, respectively. The value of each metric corresponding to the best clustering according to each clustering evaluation method, is highlighted.

| Scenario | $k$ | Silhouette Coefficient | Davies-Bouldin Index | Calinski-Harabasz Index |
|----------|-----|------------------------|----------------------|-------------------------|
| a)       | 4   | <b>0.238</b>           | 0.459                | 418 616.9               |
| b)       | 5   | 0.109                  | <b>0.448</b>         | 487 504.5               |
| c)       | 6   | 0.117                  | 0.449                | 565 026.4               |
| d)       | 7   | 0.116                  | 0.463                | <b>694 988.4</b>        |

If we revisit the definition of the silhouette coefficient in section 2.3.3, we infer that a silhouette coefficient of one is obtained when the clusters are compact and far away from the other clusters, conversely, negative scores indicate overlapping clusters [125]. A zero value of this metric indicates that the clusters are extremely close to each other, but without overlapping. Table 4.2 results of the silhouette coefficients consist of values near zero, which indicate clusters extremely close to each other, in other words, the values of the pixels intensity between clusters do not vary abruptly. As discussed before, the MRI data comprises a vast range of continuous values, thus the clusters obtained after segmentation are not dense nor well-separated and consequently, the scores of the silhouette coefficient, which are focused on measuring cluster cohesion and separation [126], do not reflect the quality of the clustering of the MRI data used in this study. As in the silhouette coefficient, both Davies-Bouldin and Calinski-Harabasz indexes compute distances of intra-cluster diversity and inter-cluster diversity, which translates into how dense and well-separated the clusters are, respectively. Hence, a good separation of different biological tissues is not reflected in the indexes of these above-mentioned metrics. In conclusion, the optimal  $k$  was chosen by an empirical visual assessment of the amount of biological

information given by each segmented image on Figure 4.14. For  $k \geq 6$ , excessive detail grouped in clusters does not allow an easy identification of the biological tissues, and for  $k = 4$ , different tissues were merged as one, such as the muscular and adipose tissue. Thus,  $k = 5$  was the chosen optimal number of clusters.

Although agglomerative hierarchical clustering provided improved segmented images, this algorithm resulted in unreasonable computational costs - 8h per axial slice which would account for ~32 days to cluster the initial volume (Intel® Core™ i7-3630QM and 16.0 GB). Hence, impractical for studies such as the one carried out, which implies several tests to determine the best sequence of steps that result in well segmented MRI images.

Segmenting slice per slice versus segmenting the volume as a whole adds the difficulty of manually having to correlate the clusters assigned with a specific cluster number in one slice, with a different number in the consecutive slices. In conclusion, the hierarchical methods are not feasible for segmenting the MRI data.

### **K-means:**

The K-means algorithm was tested in the whole 3D dataset, both in MATLAB® and Python™. As the results and the computational costs were very similar, I chose to work with the MATLAB® software as the majority part of my research group's work was developed using this software.

The variation of  $k$  was set in the range of values from  $k = 4$  to  $k = 7$ . The minimum value of  $k$  in the range is the minimum number of tissues expected to be found in the segmented images (background, muscle, bone and fat tissues) and the maximum value is the maximum number of clusters which allow a finer separation of the tissues, which can be later manually combined into more anatomical meaningful clusters. The resulting segmented images from a) to d), are represented in Figure 4.15.

The optimal  $k$  was determined by the values of the clustering quality metrics, such as the silhouette coefficient and the Davies-Bouldin and Calinski-Harabasz indexes. These results are shown in Table 4.4.

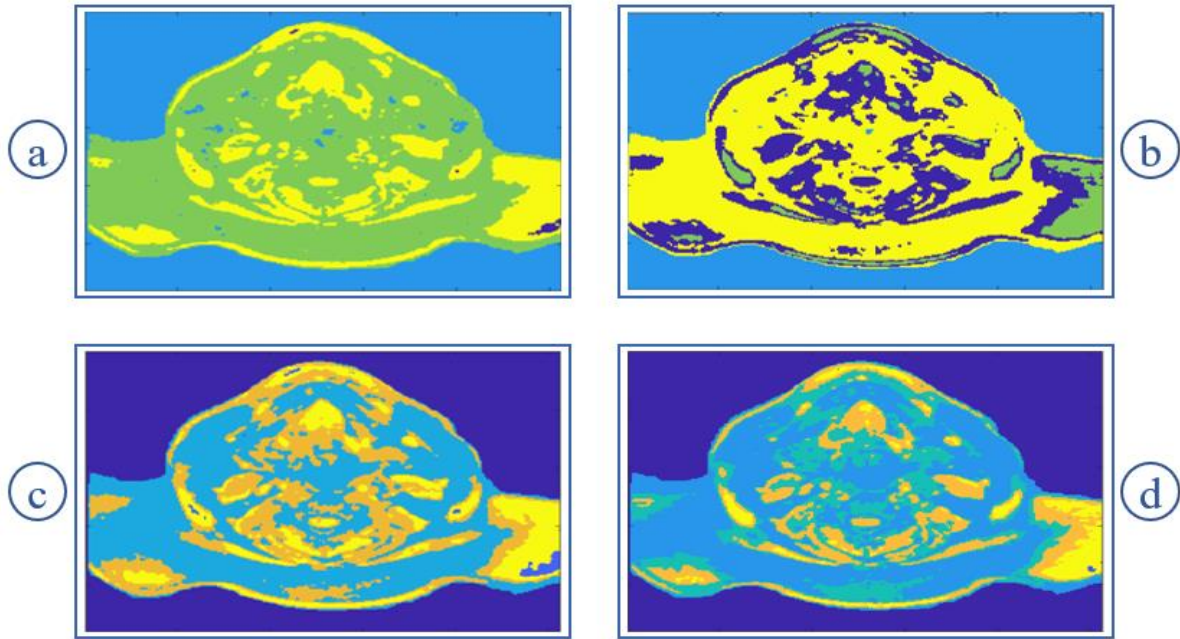


Figure 4. 15: Segmented images after the application of the K-means clustering algorithm, with different  $k$  numbers of cluster. a)  $k=4$ , b)  $k=5$ , c)  $k=6$ , and d)  $k=7$ .

Table 4. 4: Values of the silhouette coefficient, and Davies-Bouldin and Calinski-Harabasz indexes calculated for each segmented image from scenario a) to d), obtained from Agglomerative Hierarchical clustering with varying  $k$  number of clusters from 4 to 7, respectively. The value of each metric corresponding to the best clustering according to each clustering evaluation method, is highlighted.

| Scenario | $k$ | Silhouette Coefficient | Davies-Bouldin Index | Calinski-Harabasz Index |
|----------|-----|------------------------|----------------------|-------------------------|
| a)       | 4   | 0.802                  | <b>8.364</b>         | 46 964.7                |
| b)       | 5   | 0.804                  | 11.432               | <b>48 447.8</b>         |
| c)       | 6   | <b>0.805</b>           | 12.329               | 36 470.9                |
| d)       | 7   | 0.804                  | 26.839               | 29 331.6                |

As discussed before, a good separation of different biological tissues is not reflected in the results of the above-mentioned metrics. Hence, the optimal  $k$  which provided the best biological information retrieval was chosen by the visual inspection of the segmented images. From Figure 4.15, little valuable anatomical information is present in a) and multiple details that hinder the extraction of relevant anatomical information are present in d). A thorough visual analysis of several slices was performed for  $k = 5$  and  $k = 6$ . The results are depicted in Figure 4.16.

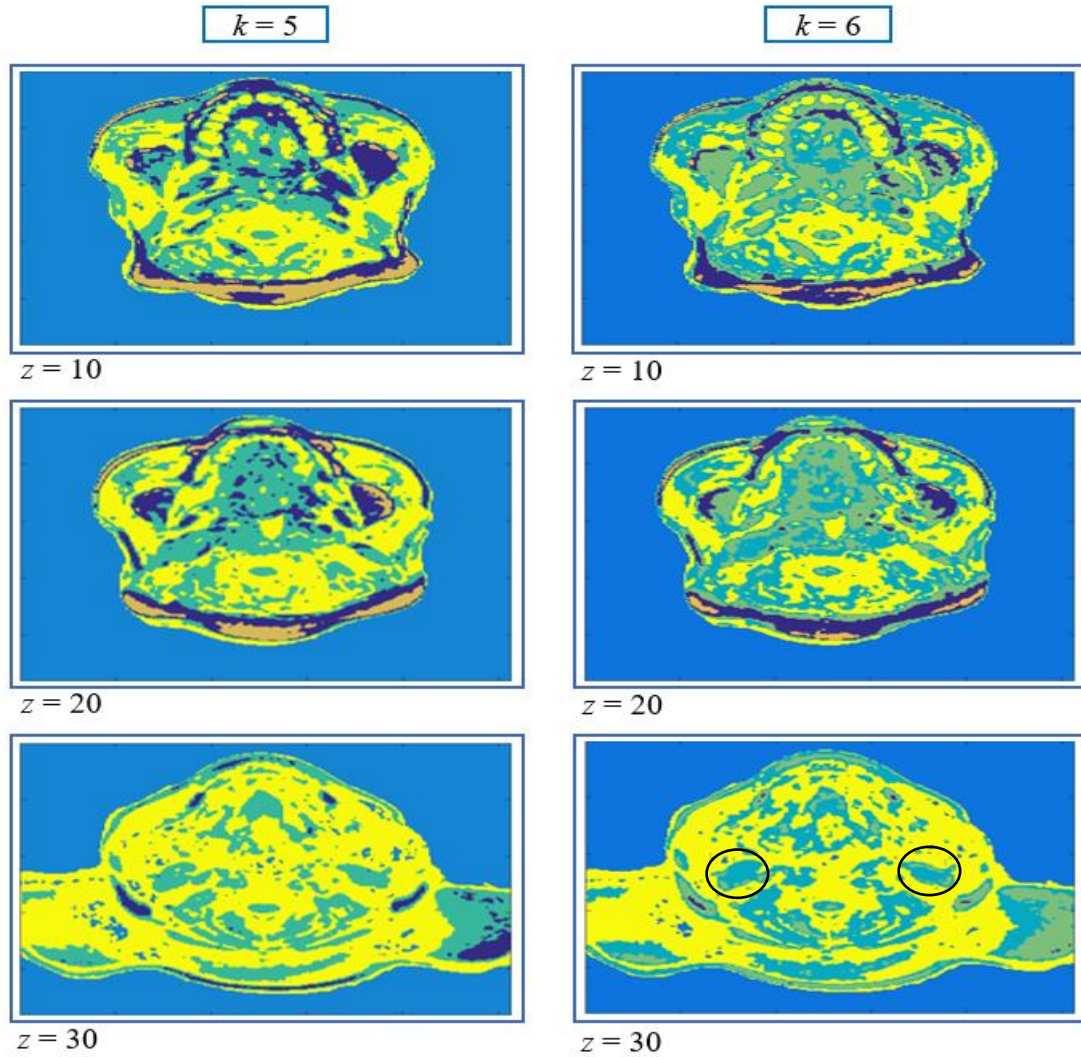


Figure 4. 16: Segmented images after the application of the K-means clustering algorithm, with  $k=5$ , on the left column, and  $k=6$  on the right. Several slices were studied,  $z=10$ ,  $20$  and  $30$ , from top to bottom, respectively.

The anatomical knowledge provided by the segmented images in which data is partitioned into five and six groups is comparable, however, for  $k=6$ , additional details produce a more complex image. For instance, the muscle tissue (sternocleidomastoid muscle) is represented by two different clusters, as observed within the black circle. Instead of adding valuable information, these details mask and make the interpretation of the main biological structures in the image difficult, and consequently their 3D printing. Therefore, I chose to work with  $k=5$ .

In conclusion, the K-means algorithm with  $k=5$  clusters was the segmentation algorithm chosen to extract anatomical features from the MRI exams of the head and neck regions. The data processing pipeline developed and optimized to provide the best anatomical information retrieval and 3D printing conditions is depicted in Figure 4.17.

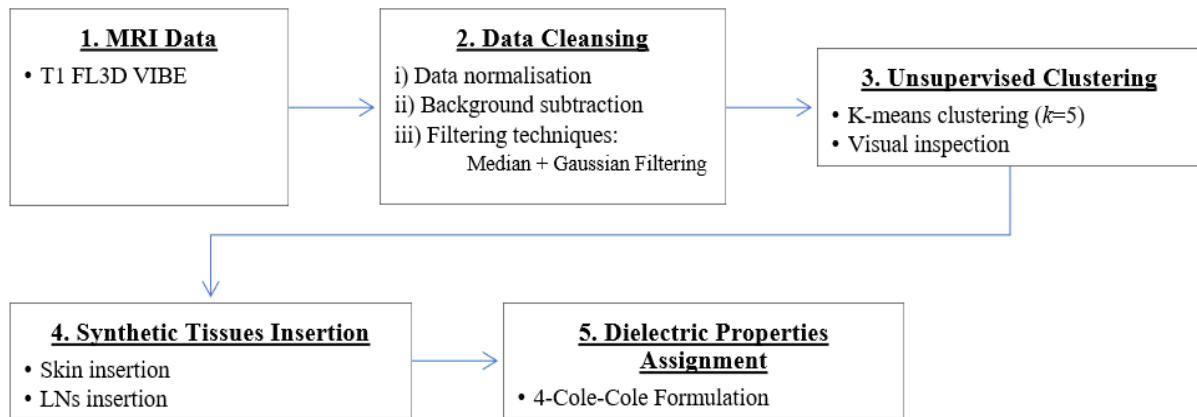


Figure 4. 17: Final data processing pipeline used to build realistic models of the head and neck region.

#### 4.3.4. Step 4 – Synthetic Tissues Insertion

After the application of the chosen segmentation algorithms some difficulties were encountered: (1) the skin tissue was not identified in one single cluster, instead several portions of skin were identified in multiple clusters and (2) the LNs, which were not easily visible in the original exams, were also not detected by the segmentation algorithms.

Problems (1) and (2) were solved with the implementation of the algorithms detailed in section 4.2.4, which allowed to solve these in an artificial manner. Specifically, these algorithms provided the creation of synthetic tissues, representing skin and LNs, which were introduced in the anatomically realistic model generated so far. Features of the tissues - such as the size, location in levels, and medical state of the LNs – can be chosen by the user. In Figure 4.18, a skin layer of a thickness of 1.4 mm is represented on the left, and two LNs in red and brown, with 1.5 mm in the major axis, healthy and located in level II, and 2.0 mm in the major axis, metastasized and located in level V, respectively, are shown on the right.

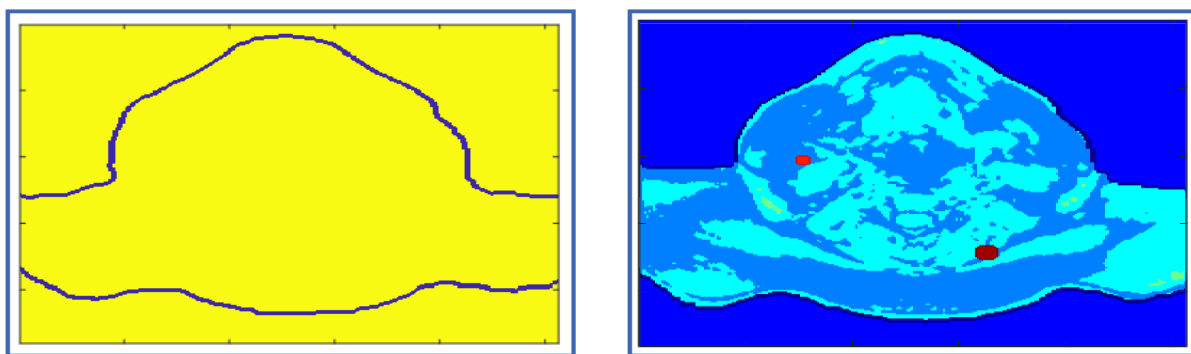


Figure 4. 18: Skin insertion algorithm created from the binary mask on the left; the blue line is the skin layer around the body. Results of the application of the LNs insertion algorithm on the right; healthy LN represented in red and metastasised LN in brown.

The step for inclusion of synthetic tissues is vital in increasing the realism/complexity of the anatomically realistic model.

#### 4.3.5. Step 5 - Dielectric Properties Assignment

The assignment of the dielectric properties step results in two matrices with the same dimensions as the model, one to store the relative permittivity and another to store conductivity, for a chosen frequency. In these matrices, each voxel, which contains the value of the dielectric property for a user-specified frequency, corresponds to the same voxel in the anatomically realistic model. Hence, the resulting matrices from this step can be viewed as 3D maps with the variation of the tissues' dielectric properties.

The matrices of the dispersion of the dielectric properties of the biological tissues within the head and neck generated in this work are compatible with FDTD modelling, which can help simulate medical MWI prototypes for screening CLNs in the head and neck regions.

#### 4.3.6. Development of the Anthropomorphic Model

The final data processing pipeline was applied to the MRI data in order to build the anthropomorphic model for the head and neck region. The results are presented in Figure 4.20, on the left. Here, the following are observed: (1) there are some small green granularities present in the orange cluster and (2) both light blue and yellow clusters represent muscle tissue. This visual inspection allowed the comprehension of the biological meaning of the data. In (1), small granularities clustered inside large clusters without anatomical meaning represent noise, and in (2), the two clusters represent the same biological tissue.

In order to address both issues, I manually merged together the clusters in Figure 4.19 (on the right). By doing this, noise and extra details, which could ultimately hinder 3D printing, were removed.

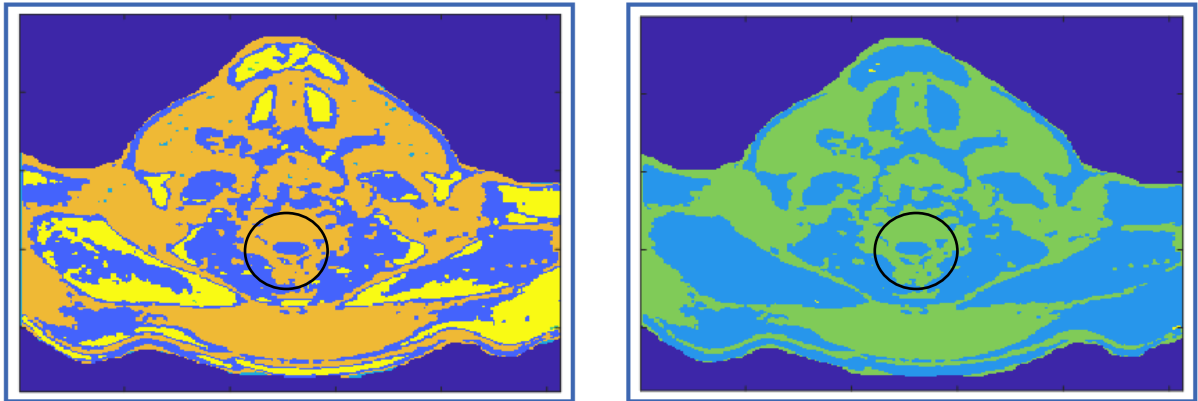


Figure 4. 19: Segmented image resulting from the application of the final data processing pipeline to the MRI exam, on the left. Final image after the merger of clusters, on the right. The black circles mark bone tissue (a vertebra).

### Registration

Both images in Figure 4.19 show that some tissues are not clearly clustered. For instance, bone tissue (vertebra observed within the black circles in Figure 4.19) is clustered with mixed tissue, and the mixed tissue itself clusters several types of biological tissues as explained before. Hence, additional tests were performed to ensure that all the relevant anatomical features were extracted from MRI exams.

Registration was pursued to combine different anatomical information provided by two separate MR sequences from the same patient. For the chosen patient, STIR T2-weighted ( $1.02 \times 1.02 \times 5.5$ ) mm and TSE T1-weighted ( $0.57 \times 0.57 \times 5.5$ ) mm images were available. Registration was tested using TSE T1- and STIR T2-weighted sequences due to their ability to highlight different elements of the body, and their equal resolution in zz. The T1-weighted exam served as reference image due to its finer resolution when compared to the T2-weighted exam, which allowed minimising information loss with the registration.

In step 1, the 3D Slicer software was used to generate the alignment transform and obtain the registered volume of STIR T2-weighted images matching the size and resolution of the reference images (Figure 4.20(1)).

Step 2 consisted of performing data cleaning and unsupervised clustering – using the methodology pipeline previously studied in this work – for both original T1-weighted images and registered T2-weighted images, in MATLAB® (Figure 4.20(2)).

Finally, step 3 included the combination of segmented images from the two sequences (segmented original T1 and segmented registered T2), by means of addition (Test A) or multiplication (Test B), in MATLAB® (Figure 4.20(3)), in an empirical attempt to quantify the combination of the segmented original and registered images.



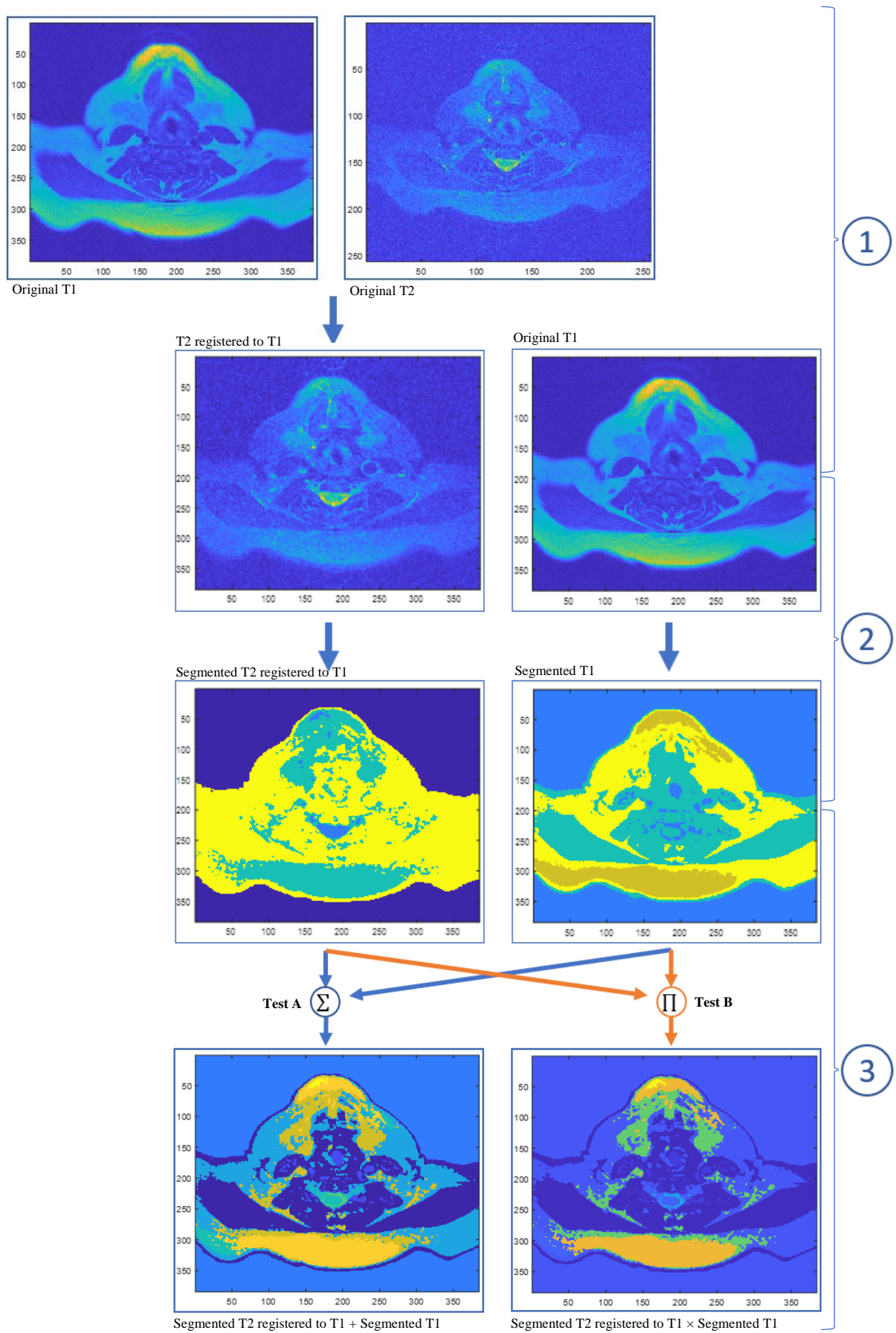


Figure 4. 20: Pipeline with the methodology of the combination process of MRI images of patient 5 acquired using different sequences, and the results obtained at step 1, 2, and 3.



The segmentation of the T1-weighted images with K-means algorithm with  $k = 5$  (Step 2), resulted in images with clusters numbered from 1 to 5. The same occurred with the application of this K-means algorithm to the registered T2-weighted images. Table 4.5 shows the combination from adding the cluster numbers from the segmented T1-weighted images (e.g. row), with the cluster numbers from the segmented registered T2-weighted images (e.g. column) and Table 4.6 provides the combination from multiplying the cluster numbers from the segmented T1-weighted images (e.g. row), with the cluster numbers from the segmented registered T2-weighted images (e.g. column).

Table 4. 5: Results from the combination of clusters by means of addition. The numbers in the rows and columns correspond to the cluster numbers from the segmented T1- and T2-weighted images.

| (+) | 1 | 2 | 3 | 4 | 5  |
|-----|---|---|---|---|----|
| 1   | 2 | - | - | - | -  |
| 2   | 3 | 4 | - | - | -  |
| 3   | 4 | 5 | 6 | - | -  |
| 4   | 5 | 6 | 7 | 8 | -  |
| 5   | 6 | 7 | 8 | 9 | 10 |

Table 4. 6: Results from the combination of clusters by means of multiplication. The numbers in the rows and columns correspond to the cluster numbers from the segmented T1- and T2-weighted images.

| (×) | 1 | 2  | 3  | 4  | 5  |
|-----|---|----|----|----|----|
| 1   | 1 | -  | -  | -  | -  |
| 2   | 2 | 4  | -  | -  | -  |
| 3   | 3 | 6  | 9  | -  | -  |
| 4   | 4 | 8  | 12 | 16 | -  |
| 5   | 5 | 10 | 15 | 20 | 25 |

The analysis of Table 4.5 showed that the combination by means of addition of the segmented images generated by Step 2 resulted in the creation of 9 different clusters with cluster numbers varying linearly from 2 to 10 with a step of 1. Also, it is also demonstrated that different combinations of cluster numbers can result in a new cluster number after the combination process. For instance, the combinations of the cluster numbers  $5 + 1$ ,  $4 + 2$  and  $3 + 3$  (marked with blue circles in Table 4.5) create the same cluster with the number 6. In other words, voxels within cluster 6 can be obtained after the combination of different clusters corresponding to different types of biological tissues, therefore the resulting clusters from this combination process can compromise future anatomically related conclusions.

Table 4.6 shows the creation of 14 clusters after the combination by means of multiplication of the segmented images provided by Step 2. In this case, the resulting cluster numbers varied from 1 to 25 non-linearly. Initially the number of the clusters are close to each other, e.g. 1, 2, 3, 4, 5 and 6, but then consecutive larger differences between the cluster numbers appear, e.g. 8, 10, 12, 15, 16, 20 and 25. Therefore, the colours observed in the images resulting from Step 3 can artificially give the perception of better segmented tissues in the multiplication case, given the distinct colours used to represent these clusters.

Besides, for both Test A and B, the number of a cluster is randomly assigned to it, therefore there is no correspondence between the cluster number and the intensity of the MRI voxels within that cluster. Hence, the colours assigned to each cluster can also make the interpretation of the segmented images harder.

In conclusion, the images obtained from these combination techniques were dismissed and solely the previously selected MRI data (T1 FL3D VIBE scans of patient 5 with resolution  $0.86 \text{ mm} \times 0.86 \text{ mm} \times 2 \text{ mm}$ ) was used.

#### 4.3.7. 3D Anthropomorphic Phantom Generator

The result of the above detailed procedure of data processing is a matrix of cluster numbers, in which each voxel contains the cluster number corresponding to the biological tissue type present in that voxel. At this stage, the biological tissue types present in the model are the ones which can be directly extracted from the segmented MRI exam after section 4.3.6 - such as fat, muscle and mixed tissue. This means that the default model includes fat, muscle and mixed tissues. The matrix of labels, the matrix of the binary masks to remove the background and the original MRI exams are the inputs of the phantom generator.

The 3D anthropomorphic phantom generator developed in this dissertation is very versatile in the way that it covers all the spectrum resulting in extremely simple or complex models of the head and neck region. Its simplest form occurs when the generated anatomically realistic phantom consists of only the interior of the body (without skin) with only one tissue - mixed tissue – with the average dielectric properties of the main tissues within this region. Increasing the complexity of the generated phantoms includes the insertion of more types of tissue, according to the level of complexity required for the development of a specific medical MWI equipment.

Similarly to the model/phantom generator in Chapter III, users can personalise their model by means of answering a series of questions. The first group of questions concerns the biological tissues to be incorporated in the model. As the starting model already includes biological tissues such as fat and muscle, the phantom generator allows the removal of these tissues in order to simplify the model. This simplification consists of turning the undesirable tissues into mixed tissue. The initial step refers to the addition of subcutaneous adipose tissue to the model (Figure 4.21). In this case, if the answer is affirmative, the cluster numbers of the voxels included in the fat cluster maintain their value, otherwise these values are replaced by the cluster number of the mixed tissue. The following step concerns the inclusion of skin tissue in the model (Figure 4.22). If affirmative, a function will create a layer of skin with 1.4 mm of thickness that surrounds the body region. The incorporation of the muscular tissue in the model is the third step (Figure 4.23). If affirmative, the cluster numbers of the voxels included in the muscle cluster maintain their value, otherwise these values are replaced by the cluster number assigned to the mixed tissue.

The second group of questions, concerning the LNs, is similar to the one used in the numerical phantom generator of Chapter III, shown in Figure 4.24. Their number is chosen in an interface (maximum of twelve in total and six per level – hence we guarantee that they are located in the desired level and do not overlap regardless their size) presented in Figure 4.25. As before, the regions of the LNs levels as well as their frontiers are clearly defined and shown to the users, which allows them to indicate the location to introduce the LNs (Figure 4.26). Finally, their size, state (healthy/metastasised) and coordinates of its the centre is chosen in the interface depicted in Figure 4.27. With this type of methodology, users can choose whether they prefer the LNs to be close together, or conversely, far apart.

The final group of questions concerns the association of the MRI voxel's intensity to the dielectric properties of the biological tissues. A matrix whose voxels contain the values of dielectric properties of the corresponding biological tissue is produced. In order to complete the matrix of the dielectric properties, the user is asked to choose a frequency value so that the algorithm is able to determine the maximum, minimum and the linearly interpolated intermediate values of the dielectric properties for each tissue type, at the chosen specific frequency (Figure 4.28).

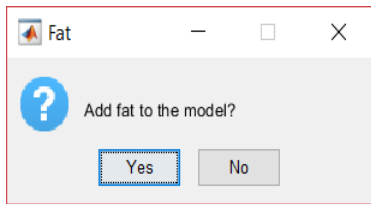


Figure 4. 21: Interface which allows the user to add subcutaneous adipose tissue to the realistic phantom.

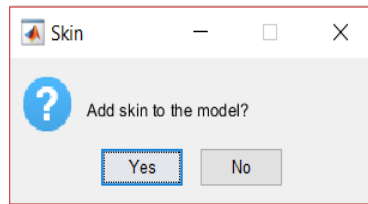


Figure 4. 22: Interface which allows the user to add skin tissue to the realistic phantom.

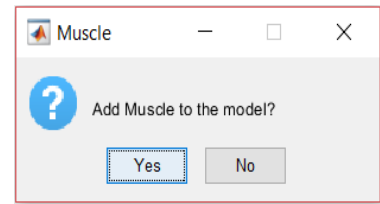


Figure 4. 23: Interface which allows the user to add muscular tissue to the realistic phantom.

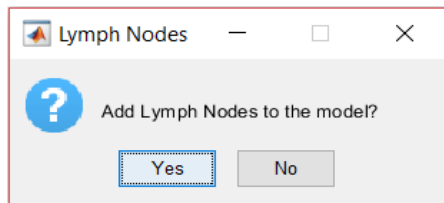


Figure 4. 24: Interface which allows the user to add lymph nodes to the realistic phantom.

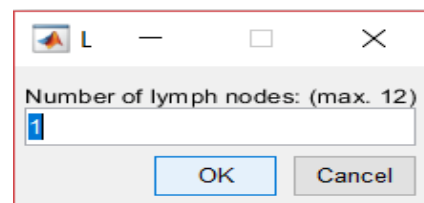


Figure 4. 25: Interface which allows the user to add the number of lymph nodes to the realistic phantom.

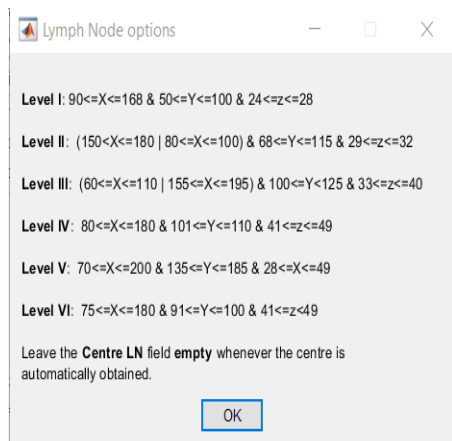


Figure 4. 26: Informative note which specifies the frontiers of the six different levels of the lymph nodes.

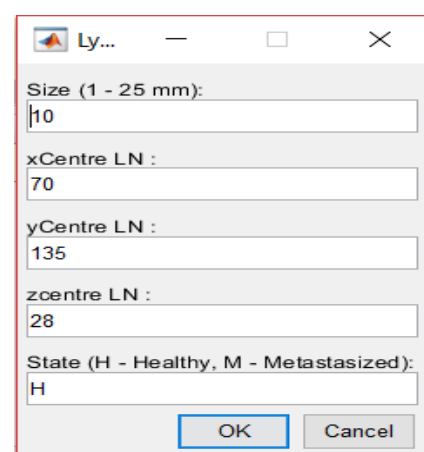


Figure 4. 27: Interface which allows the user to choose the size, location and state of a lymph node.

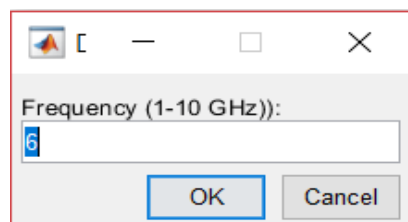


Figure 4. 28: Interface which allows the user to choose the frequency value at which the algorithm should interpolate the dielectric properties values of the biological tissues.

If the user is not interested in specifying the location of the LNs, the phantom generator will automatically assign default locations (Figure 4.29). After designing the phantom, the user can choose to save the phantom (Figure 4.30). In this case, the following models: i) before segmentation, ii) after segmentation and tissue selection, and iii) the matching dielectric properties matrices will be saved in .mat files. The dielectric properties matrices have the same dimensions as the MRI exam, since each voxel of the MRI exam corresponds to the relative permittivity and conductivity values, at a chosen frequency, in the matrix of permittivity and conductivity, respectively.

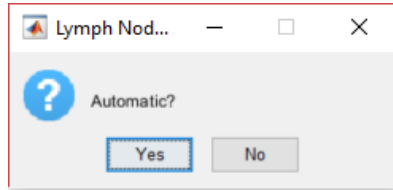


Figure 4. 29: Interface which allows the user to choose whether he/she wants to specify the location of the LNs or if he/she prefers the phantom generator to automatically assign positions to the LNs.

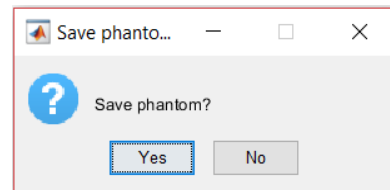


Figure 4. 30: Interface which allows the user to save the phantom.

For printing purposes, the final phantom (model after the segmentation) will have its original-shaped voxels resized to cubic-shaped voxels so that a physical model is not shrunk in the z-direction due to the original resolution of the MRI exams, and will be saved in STL format.

## 4.4. Chapter Conclusions

The creation of anthropomorphic models of the head and neck region was detailed in this chapter. Here, every step from the building process of such models and the 3D anatomically realistic phantom generator, is described. As before, the generator was designed to allow the creation of head and neck models.

The anatomical data incorporated in the model (T1 FL3D VIBE exams from patient 5) was chosen over the others given its significant higher resolution in the axial plane and easy visual identification of the biological structures.

Both ideal and Butterworth filters resulted in clustering with several small-sized granularities, which ultimately compromise 3D-printed phantoms. Median filters were proved the best for smoothing edges and Gaussian filters were effective in removing noise. The combination of the last two was found to be the best approach for data pre-processing since they tackle different problems and combined, they allow the best anatomical information retrieval.

No useful segmentation was obtained from DBSCAN and BIRCH algorithms. In the first case, the algorithm was not capable of grouping data points in large clusters with anatomical meaning, instead, only small and very sparse clusters were found. Hence, the DBSCAN algorithm for clustering was excluded from the methodology pipeline. The results of BIRCH showed severe loss of anatomical

information for  $k \leq 4$ , but several noisy small-sized granularities and clusters without explicit anatomical meaning for  $k \geq 5$ . Neither option is appropriate to be used to build the model, thus, BIRCH algorithm was excluded from the methodology pipeline. Despite providing clustering with anatomical meaning, HCA algorithms used unreasonable computational costs - 8h per axial slice which would account for ~32 days to cluster the initial full volume (Intel® Core™ i7-3630QM and 16.0 GB). Finally, K-means clustering was the adopted algorithm given its speed and good clustering quality. In order to determine the optimal  $k$ , three different metrics were calculated. Results showed that good values of metrics did not imply good anatomical information retrieval, for the dataset used in this project – this was observed empirically. As a result, visual inspection and comparison to prior anatomical knowledge were empirically used to assess the segmentation quality.

As skin tissue and LNs were not correctly segmented in the models after the segmentation procedure, algorithms which allowed the manual insertion of such tissues, were developed. Despite increasing the variability of the models by choosing the location of the LNs within the levels, size and medical state, their shape and direction (horizontal, vertical, oblique) were fixed for purposes of simplification. In the future, the combination of the anatomical information from the MRI exams with the information from other modalities, such as CT images, may be fruitful for the identification of the location of the LNs, which ultimately would allow an automatic segmentation of these tissues without having to manually insert them.

Synthetic skin tissue was also added to the models as this tissue was not correctly segmented by the unsupervised clustering algorithms. In the model, a fixed thickness for skin tissue was chosen for simplification purposes. Future work should improve the realism of the models created by the phantom generator.

During the construction of the head and neck models, users are asked several questions in order to personalize each model. The first group of questions concerns the tissues they wish to include in the model, the second group of questions concerns the LNs and their features and the third group concerns the association of the MRI voxel's intensity to the dielectric properties of the biological tissues. When finalised, users can save their phantom in .mat files and STL file format for printing.

## Chapter V – Conclusions and Future work

The objective of this project was twofold: firstly, it aimed at developing a phantom generator of 3D computational models for the head and neck region with different levels of complexity, and secondly, it focused on creating a realistic anthropomorphic phantom generator derived from MRI exams, using anatomical knowledge, ML techniques, and realistic dielectric properties of biological tissues. For both cases, the ultimate goal – beyond the scope of this project – consists of later using the developed phantoms to assess the feasibility of a MWI prototype system in imaging and diagnosing CLNs, as there is a significant diagnostic blind-spot regarding mass screening of LNs in the case of head and neck cancers.

The 3D numerical phantom generator developed in this project allows the creation of 3D computational models of the head and neck region, with varying levels of complexity to match the interests of the researchers, and consequently, it extends the applicability of the numerical models to several fields of research. The process of creating a model consists of a sequence of steps which allow the incorporation of biological tissues, such as skin, muscle, fat and bone tissue, in the model. LNs can also be included and their number, size, location and medical condition (*i.e.* whether or not they are metastasised) are defined by the user.

Although the level of realism provided by the developed 3D numerical models was limited, these models have an utmost importance in the initial process of MWI prototype development as they fairly represent the general features of the human anatomy, and more complex models may hinder initial progress in the development of an MWI tailored to image the head and neck regions. Hence, the numerical models developed in this project were used as a starting point to reach more complex and realistic models.

Future work in this area could include some improvement efforts, such as the determination of more realistic measures, shapes and locations of the biological structures within the cervical region and also, the incorporation of smaller tissues.

The second part of this work aimed at creating a generator of 3D computational anatomically realistic phantoms of the head and neck region based on MRI segmented data. A methodology pipeline was designed and optimized in order to obtain a model as realistic as possible for later 3D printing.

The methodology pipeline consisted of: (1) MRI data selection which is an extremely important step to assure that the model accurately represents the head and neck anatomy. High resolution exams with low noise levels, which provide easy visual identification of the anatomical structures, are vital for this project. (2) Data cleaning steps allowed the background subtraction, removal of noise, smoothing of sharp edges in the boundaries of the tissues, and elimination of small-sized granularities which make the segmentation process difficult. (3) Different unsupervised clustering algorithms, such as K-means, Agglomerative Hierarchical, BIRCH and DBSCAN, were tested, and the K-means partitioning method (with a  $k = 5$ ) excelled against the others in its fast computation and results with explicit anatomical meaning. The optimization of this algorithm was performed by an empirical visual assessment of the amount of anatomical information given the segmented images as the tested intrinsic metrics, such as the silhouette coefficient, Davies-Bouldin and Calinski-Harabasz indexes, did not reflect a good separation of different biological tissues.

The developed phantom generator uses as input the results from the methodology pipeline to create anatomically realistic phantoms of the head and neck. The default anatomically realistic model includes few biological tissues, such as muscle, adipose and mixed tissues. Users choose which tissues they desire

to include in the phantoms by answering a sequence of questions regarding the pre-existing tissues in the phantom, and new synthetical tissues which can be included, such as skin and LNs. Similarly to the 3D numerical phantom generator, the LNs number, location and medical condition in the 3D anthropomorphic phantom generator are defined by the user. Finally, the dielectric properties of the biological tissues, for a user specify frequency, are assigned to the MRI voxel's intensity. After the phantom creation process, the models before segmentation and after the inclusion of all tissue can be saved in .mat files along with the matrices of the corresponding dielectric properties.

In all the considered unsupervised clustering algorithms, each data point belonged to one cluster only. This strict requirement can lead to an erroneous segmentation, especially when considering continuous data values (MRI intensities) such as those in the project. Although K-means segmentation provided very good and realistic results, I propose that future work should include the study of more advanced unsupervised segmentation algorithms, such as probabilistic model-based cluster analysis, which can be computed using the Expectation-Maximization Algorithm. In these models, fuzzy/flexible clusters allow the objects to participate in multiple clusters. Each one of these probabilistic clusters is mathematically represented by a probability density function. At the end, the goal is to infer from the data the set of probabilistic clusters that is most likely to generate the data.

In the context of future work, semi-supervised methods appear to be also a viable option to segment the head and neck MRI exams as the validation of the results provided by the studied unsupervised methods requires users with great anatomical knowledge of the region under test. Semi-supervised methods fall between unsupervised and supervised methods; therefore, they make use of a small amount of labelled data (in this case, manual segmentation provided by physicians) with a large amount of unlabelled data (MRI exams). Thus, these methods should entail great potential as the manual segmentation would be particularly valuable to validate the automatic segmentation of the main tissues and in the identification of LNs.

## References

- [1] International Agency for Research on Cancer, "World Health Organization, GLOBOCAN 2018: Estimated Cancer Incidence, Mortality and Prevalence Worldwide in 2018," [Online]. Available: <http://gco.iarc.fr/>. [Accessed October 2018].
- [2] S. Remmert, M. Rottmann, M. Reichenbach, K. Sommer and H. Friedrich, "Lymphknotenmetastasierung bei kopf-hals-tumoren (Lymph node metastasis in head-neck tumors)," *Laryngo-Rhino-Otologie*, vol. 80, no. 1, pp. 27-35, 2001.
- [3] N. Patani, M. Dwek and M. Douek, "Predictors of axillary lymph node metastasis in breast cancer: a systematic review," *Eur. J. Surg. Oncol.*, vol. 33, no. 4, pp. 0748-7983, 2007.
- [4] M. Sapienza, M. Tavares, I. Endo, G. Neto, M. Lopes, S. Nakagawa, F. Belfort, J. Soares Jr, S. Lewin and M. Marone, "The role of sentinel node mapping in malignant melanoma: experience with 99mTc-phytate and a review of the literature," *An. Bras. Dermatol.*, vol. 79, no. 2, pp. 181-191, 2004.
- [5] S. Exposto, *Personal communication*, 2014.
- [6] S. G. Komen, "Facts for Life: Axillary Lymph Node," 2009. [Online]. Available: [http://ww5.komen.org/uploadedfiles/Content\\_Binaries/806-392a.pdf](http://ww5.komen.org/uploadedfiles/Content_Binaries/806-392a.pdf).
- [7] H. Rahbar, S. Partridge, S. Javid and C. Lehman, "Imaging axillary lymph nodes in patients with newly diagnosed breast cancer," *Curr. Probl. Diagn. Radiol.*, vol. 41, no. 5, pp. 149-158, 2012.
- [8] Macmillan Cancer Support, "Surgery for head and neck cancer," [Online]. Available: <http://www.macmillan.org.uk/>.
- [9] Cancer Research UK, "Lymphoedema after breast cancer treatment," [Online]. Available: <https://www.cancerresearchuk.org/>.
- [10] A. Srinivasan, S. Mohan and S. Mukherji, "Biologic imaging of head and neck cancer: the present and the future," *AJNR Am. J. Neuroradiol.*, vol. 33, no. 4, pp. 586-594, 2012.
- [11] J. Liu and S. G. Hay, "Prospects for microwave imaging of the lymphatic system in the axillary," in *2016 IEEE-APS Topical Conference on Antennas and Propagation in Wireless Communications (APWC)*, Cairns, QLD, 2016.
- [12] P. Zbaren, M. Becker and H. Laeng, "Pretherapeutic staging of hypopharyngeal carcinoma. Clinical findings, computed tomography, and magnetic resonance imaging compared with histopathologic evaluation.," *Arch. Otolaryngol. Head Neck Surg.*, vol. 123, pp. 908-913, 1997.
- [13] S. Ng, Y. Tzu-Chen, J. Chang, S. Chan, S. Ko, H. Wang, L. Lee, C. Kang, A. Wong and C. Liao, "Prospective study of [18F]fluorodeoxyglucose positron emission tomography and computed tomography and magnetic resonance imaging in oral cavity squamous cell carcinoma with palpably negative neck," *J. Clin. Oncol.*, vol. 24, no. 27, pp. 4371-4376, 2006.



- [14] B. Branstetter, T. Blodgett, L. Zimmer, C. Snyderman, J. Johnson, S. Raman and C. Meltzer, "Head and neck malignancy: is PET/CT more accurate than PET or CT alone?," *Radiology*, vol. 235, no. 2, pp. 580-586, 2005.
- [15] E. Troost, D. Schinagel, J. Bussink, O. Boerman, A. van der Kogel, W. Oyen and J. Kaanders, "Innovations in radiotherapy planning of head and neck cancers: role of PET," *J. Nucl. Med.*, vol. 51, no. 1, pp. 66-76, 2010.
- [16] A. Malich, T. Boehm, M. Facius, H. Mentzel, M. Fleck, J. Boettcher, R. Anderson and W. Kaiser, "Use of electrical impedance scanning in the differentiation of sonographically suspicious and highly suspicious lymph nodes of the head-neck region," *Eur. Radiol.*, vol. 12, no. 5, pp. 1114-1120, 2002.
- [17] D. M. Pozar, *Microwave Engineering*, 4th Edition ed., John Wiley & Sons, 2011.
- [18] Z. Wang, E. Lim, Y. Tang and M. Leach, "Medical applications of microwave imaging," *Sci. World J.*, pp. 1-7, 2014.
- [19] E. Fear, J. Bourqui, C. Curtis, D. Mew, B. Docktor and C. Romano, "Microwave breast imaging with a monostatic radar-based system: a study of application to patients," *IEEE Trans. Microw. Theory Tech.*, vol. 61, no. 5, pp. 2119-2128, 2013.
- [20] E. Porter, K. Duff, M. Popovic and M. Coates, "Investigation of time-domain microwave radar with breast clinic patients," in *2016 10th European Conference on Antennas and Propagation (EuCAP)*, Switzerland, 2016, pp. 1-3.
- [21] E. Fear, "Microwave imaging of the breast," *Technol. Cancer Res. Treat.*, vol. 4, no. 1, pp. 69-82, 2005.
- [22] F. Yang, L. Sun, Z. Hu, H. Wang, D. Pan, R. Wu, X. Zhang, Y. Chen and Q. Zhang, "A large-scale clinical trial of radar-based microwave breast imaging for Asian women: phase I," in *2017 IEEE International Symposium on Antennas and Propagation USNC/URSI National Radio Science Meeting*, San Diego, CA, USA, 2017, pp. 781-783.
- [23] A. Preece, I. Craddock, M. Shere, L. Jones and H. Winton, "MARIA M4: clinical evaluation of a prototype ultrawideband radar scanner for breast cancer detection," *J. Med. Imaging*, vol. 3, no. 3, pp. 033502.1-7, 2016.
- [24] Micrima Limited, "Micrima - Evolving Medical Imaging," 2018. [Online]. Available: <http://micrima.com/>.
- [25] R. Conceição, L. Oliveira, B. Banks and E. Fear, "Development of axilla phantoms to aid breast cancer staging via sentinel lymph node detection," in *The 8th European Conference on Antennas and Propagation*, The Hague, The Netherlands, 2014.
- [26] R. Eleutério, A. Medina and R. Conceição, "Initial study with microwave imaging of the axilla to aid breast cancer diagnosis," in *USNC-URSI Radio Science Meeting (Joint with AP-S Symposium)*, Memphis, TN, USA, 2014.

- [27] R. Eleutério and R. Conceição, "Initial study for detection of multiple lymph nodes in the axillary region using microwave imaging," in *9th European Conference on Antennas and Propagation (EuCAP)*, Lisbon, Portugal, 2015.
- [28] K. Van de Graaff, *Human Anatomy*, 6th edition ed., Boston, MA: McGraw-Hill Companies, 2002.
- [29] A. Vasavada, J. Danaraj and G. Siegmund, "Head and neck anthropometry, vertebral geometry and neck strength in height-matched men and women," *J. Biomech.*, vol. 41, pp. 114-121, 2008.
- [30] S. Stranding, N. Anand, R. Birch, P. Collins, A. Crossman, M. Gleeson, G. Jawaheer, A. Smith, J. Spratt, M. Stringer, R. Tubbs, R. Tunstall, A. Wein and C. Wigley, *Gray's Anatomy: The Anatomical Basis of Clinical Practice*, 41st edition ed., Elsevier, 2016.
- [31] M. Fehrenbach and S. Herring, *Illustrated Anatomy of the Head and Neck*, 5th Edition ed., Saunders Elsevier, 2016.
- [32] R. Seeley, P. Tate and T. Stephens, *Anatomy and Physiology*, 8th Edition ed., McGraw-Hill Higher Education, 2007.
- [33] National Cancer Institute, "What is Cancer?," [Online]. Available: <https://www.cancer.gov/>. [Accessed July 2019].
- [34] P. van der Riet, H. Nawroz, R. Hruban, R. Corio, K. Tokino, W. Koch and D. Sidransky, "Frequent loss of chromosome 9p21-22 early in head and neck cancer progression," *Cancer Res.*, vol. 54, no. 5, pp. 1156-8, 1994.
- [35] P. Cairns, T. Polascik, Y. Eby, K. Tokino, J. Califano, A. Merlo, L. Mao, J. Herath, R. Jenkins, W. Westra, J. Rutter, A. Buckler, E. Gabrielson, M. Tockman, K. Cho, L. Hedrick, G. Bova, W. Isaacs, W. Koch, D. Schwab and D. Sidransky, "Frequency of homozygous deletion at p16/CDKN2 in primary human tumours," *Nature Genet.*, vol. 11, no. 2, pp. 210-2, 1995.
- [36] M. Hollstein, D. Sidransky, B. Vogelstein and C. Harris, "p53 mutation in human cancers," *Science*, vol. 253, no. 5015, pp. 49-53, 1991.
- [37] K. Somers, M. Merrick, M. Lopez, L. Incognito, G. Schechter and G. Casey, "Frequent p53 mutations in head and neck cancer," *Cancer Res.*, vol. 52, no. 21, pp. 5997-6000, 1992.
- [38] P. Jares, P. Fernández, E. Campo, A. Nadal, F. Bosch, G. Aiza, I. Nayach, J. Traserra and A. Cardesa, "PRAD-1/cyclin D1 gene amplification correlates with messenger RNA overexpression and tumor progression in human laryngeal carcinomas," *Cancer Res.*, vol. 54, no. 17, pp. 4813-7, 1994.
- [39] M. Walden and N. Aygun, "Head and neck cancer," *Semin. Roentgenol.*, vol. 48, no. 1, pp. 75-86, 2013.
- [40] A. Agiris and C. Eng, "Epidemiology, staging, and screening of head and neck cancer," *Cancer Treat. Res.*, vol. 114, pp. 15-60, 2003.

- [41] J. Brennan, J. Boyle, W. Koch, S. Goodman, R. Hruban, Y. Eby, M. Couch, A. Forastiere and D. Sidransky, "Association between cigarette smoking and mutation of the p53 gene in squamous-cell carcinoma of the head and neck," *N. Engl. J. Med.*, vol. 332, no. 11, pp. 712-7, 1995.
- [42] J. Muscat and E. Wynder, "Tobacco, alcohol, asbestos, and occupational risk factors for laryngeal cancer," *Cancer*, vol. 69, no. 9, pp. 2244-51, 1992.
- [43] L. Brown, T. Mason, L. Pickle, P. Stewart, P. Buffer, K. Burau, R. Ziegler and J. Fraumeni Jr, "Occupational risk factors for laryngeal cancer on the texas gulf coast," *Cancer Res.*, vol. 48, no. 7, pp. 1960-4, 1988.
- [44] J. Pierce, K. Messer, M. White, D. Cowling and D. Thomas, "Prevalence of heavy smoking in California and the United States, 1965-2007," *JAMA*, vol. 305, no. 11, pp. 1106-1112, 2011.
- [45] B. Robu and P. Cole, "Declining mortality from smoking in the United States," *Nicotine Tob. Res.*, vol. 9, no. 7, pp. 781-784, 2007.
- [46] C. Wittekindt, S. Wagner, C. Mayer and J. Klussmann, "Human papillomavirus (HPV) and head and neck cancer," *Hautarzt*, vol. 63, pp. 24-29, 2012.
- [47] G. D'Souza, A. Keimer, R. Viscidi, M. Pawlita, C. Fakhry, W. Koch, W. Westra and M. Gillison, "Case-control study of human papillomavirus and oropharyngeal cancer," *N. Engl. J. Med.*, vol. 356, pp. 1944-1956, 2007.
- [48] M. Gillison, W. Koch, R. Capone, M. Spafford, W. Westra, L. Wu, M. Zahurak, R. Daniel, M. Viglione, D. Symer, K. Shah and D. Sidransky, "Evidence for a causal association between human papillomavirus and a subset of head and neck cancers," *J. Natl. Cancer Inst.*, vol. 92, no. 9, pp. 709-720, 2000.
- [49] L. Young, C. Dawson, D. Clark, H. Rupani, P. Busson, T. Tursz, A. Johnson and A. Rickinson, "Epstein-Barr virus gene expression in nasopharyngeal carcinoma," *J. Gen. Virol.*, vol. 69, no. Pt 5, pp. 1051-1065, 1988.
- [50] G. Wolf, S. Lippman, G. Laramore and W. Hong, Head and neck cancer, 3rd ed., J. Holland, E. Frei, R. Bast Jr, D. Kufe, D. Morton and R. Weichselbaum, Eds., Philadelphia: Lea & Febiger, 1992, pp. 1211-1274.
- [51] E. Vokes, R. Weichselbaum, S. Lippman and W. Hong, "Head an neck cancer," *N. Engl. J. Med.*, vol. 328, no. 3, pp. 184-194, 1993.
- [52] A. Forastiere, W. Koch, A. Trotti and D. Sidransky, "Head and neck cancer," *N. Engl. J. Med.*, vol. 345, no. 26, pp. 1890-1900, 2001.
- [53] American Joint Committee on Cancer, Breast Cancer Staging, 7th Edition Staging Posters ed., 2009.
- [54] American Academy of Otolaryngology - Head and Neck Surgery Foundation, "Quick reference guide to TNM staging of head and neck dissection classification," 2014. [Online]. Available: [https://www.entnet.org/sites/default/files/NeckDissection\\_QuickRefGuide\\_highresFINAL.pdf](https://www.entnet.org/sites/default/files/NeckDissection_QuickRefGuide_highresFINAL.pdf).

- [55] American Cancer Society, "Lymph Nodes and Cancer," 2015. [Online]. Available: <http://www.cancer.org/cancer/cancerbasics/lymph-nodes-and-cancer>. [Accessed October 2018].
- [56] S. Dubner, S. Ostrower, F. Talavera, J. Garza and D. Narayan, "Head and Neck Cancer - Resection and Neck Dissection," 2017. [Online]. Available: <https://emedicine.medscape.com/article/1289474-overview#showall>.
- [57] J. Still and E. Fear, "Tissue sensing adaptive radar for breast cancer detection—experimental investigation of simple tumor models," *IEEE Trans. Microw. Theory Tech.*, vol. 53, no. 11, pp. 3312-3319, 2005.
- [58] D. Winters, J. Shea, E. Madsen, G. Frank, B. Van Veen and S. Hagness, "Estimating the breast surface using UWB microwave monostatic backscatter measurements," *IEEE Trans. Biomed. Eng.*, vol. 55, no. 1, pp. 247-256, 2008.
- [59] M. Klemm, J. Leendertz, D. Gibbins, I. Craddock, A. Preece and R. Benjamin, "Microwave radar-based breast cancer detection: imaging in inhomogeneous breast phantoms," *IEEE Antennas Wireless Propagat. Lett.*, vol. 8, pp. 1349-1352, 2009.
- [60] J. Croteau, J. Sill, T. Williams and E. Fear, "Phantoms for testing radar-based microwave breast imaging," in *13th International Symposium on Antenna Technology and Applied Electromagnetics and the Canadian Radio Science Meeting*, Banff, Alberta, Canada, 2009.
- [61] J. Garrett and E. Fear, "Average property estimation validation with realistic breast models," in *The 8th European Conference on Antennas and Propagation (EuCAP 2014)*, The Hague, Netherlands, 2014.
- [62] J. Garrett and E. Fear, "Stable and flexible materials to mimic the dielectric properties of human soft tissues," *IEEE Antennas Wireless Propag. Lett.*, vol. 13, pp. 599-602, 2014.
- [63] A. Santorelli, O. Laforest, E. Porter and M. Popovic, "Image classification for a time-domain microwave radar system: Experiments with stable modular breast phantoms," in *9th European Conference on Antennas and Propagation (EuCAP)*, Lisbon, Portugal, 2015.
- [64] R. Scapaticci, L. Di Donato, I. Catapano and L. Crocco, "A feasibility study on microwave imaging for brain stroke monitoring," *PIER B*, vol. 40, pp. 305-324, 2012.
- [65] M. Bjelogrić, M. Volery, B. Fuchs, J. Thiran, J. Mosig and M. Mattes, "Stratified spherical model for microwave imaging of the brain: Analysis and experimental validation of transmitted power," *Microw. Opt. Techn. Lett.*, vol. 60, pp. 1042-1048, 2018.
- [66] A. Fhager, S. Candefjord and M. Elam, "3D simulations of intracerebral hemorrhage detection using broadband microwave technology," *Sensors*, vol. 19, no. 3482, 2019.
- [67] C. Cocosco, R. S. Kwan and D. Collins, "BrainWeb: Simulated Brain Database," [Online]. Available: <https://brainweb.bic.mni.mcgill.ca/brainweb/>.
- [68] J. Brand, R. Kuba and T. Braunreiter, "An improved head-and-neck phantom for radiation dosimetry," *Oral Surg. Oral Med. Oral Pathol.*, vol. 67, no. 3, pp. 338-346, 1989.

- [69] A. Molineu, D. Followill, P. Balter, W. Hanson, M. Gillin, M. Hug, A. Eisbruch and G. Ibbott, "Design and implementation of an anthropomorphic quality assurance phantom for intensity-modulated radiation therapy for the radiation therapy oncology group," *Int. J. Radiat. Oncol. Biol. Phys.*, vol. 63, no. 2, pp. 577-583, 2005.
- [70] M. Paulides, D. Weilheesen, J. Van Der Zee and G. Van Rhoon, "Assessment of the local SAR distortion by major anatomical structures in a cylindrical neck phantom," *Int. J. Hyperth.*, vol. 21, no. 2, pp. 125-140, 2005.
- [71] I. Merunka, O. Fiser, L. Vojackova, J. Vrba and D. Vrba, "Array of balanced antipodal vivaldi antennas used for microwave hyperthermia treatment of neck cancer," in *24th International Conference Radioelektronika*, 2014.
- [72] A. Christ, W. Kainz, E. Hahn, K. Honegger, M. Zefferer, E. Neufeld, W. Rascher, R. Janka, W. Bautz, J. Chen, B. Kiefer, P. Schmitt, H. Hollenbach, J. Shen, M. Oberle, D. Szczerba, A. Kam, J. Guag and N. Kuster, "The virtual family - development of surface-based anatomical models of two adults and two children for dosimetric simulations," *Phys. Med. Biol.*, vol. 55, no. 2, pp. 23-28, 2010.
- [73] H. Ali, "MRI medical image denoising by fundamental filters," in *High Resolution Neuroimaging*, vol. 2, A. Halefoğlu, Ed., IntechOpen, 2018, pp. 111-124.
- [74] R. Gonzalez and R. Woods, *Digital Image Processing*, New Jersey: Prentice Hall, 2002.
- [75] I. Sitdikov and A. Krylov, "Variational image deringing using varying regularization parameter," *Pattern Recogn. Image Anal.*, vol. 25, no. 1, pp. 96-100, 2015.
- [76] S. Saladi and N. Amutha Prabha, "MRI brain segmentation in combination of clustering methods with markov random field," *Int. J. Imaging Syst. Technol.*, vol. 28, no. 3, pp. 207-216, 2018.
- [77] H. Ng, S. Ong, K. Foong, P. Goh and W. Nowinski, "Medical image segmentation using k-means clustering and improved watershed algorithm," in *IEEE Southwest Symposium on Image Analysis and Interpretation*, Denver, CO, 2006.
- [78] J. Han, M. Kamber and J. Pei, *Data Mining, concepts and techniques*, 3rd ed., MA, USA: Elsevier, 2012, pp. 443-496.
- [79] P. Berkhin, "A Survey of Clustering Data Mining Techniques," in *Grouping Multidimensional Data*, Springer, Berlin, Heidelberg, 2006, pp. 25-71.
- [80] S. Roy and D. Bhattacharyya, *Data Mining Techniques and Its Application in Medical Imagery*, Germany: VDM Verlag Dr. Müller, 2010.
- [81] G. Mirzaei and H. Adeli, "Segmentation and clustering in brain MRI imaging," *Rev. Neurosci.*, 2018.
- [82] S. Ray and R. Turi, "Determination of number of clusters in k-means clustering and application in colour image segmentation," in *Proceedings of the 4th International Conference on Advances in Pattern Recognition and Digital Techniques (ICAPRDT'99)*, 2000.

- [83] C. Rosenberger and K. Chehdi, "Unsupervised clustering method with optimal estimation of the number of clusters: application to image segmentation," in *Proceedings 15th International Conference on Pattern Recognition. ICPR*, Barcelona, Spain, 2000.
- [84] J. Rajapakse, J. Giedd and J. Rapoport, "Statistical approach to segmentation of single-channel cerebral MR images," *IEEE Trans. Med. Imaging*, vol. 16, no. 2, pp. 176-186, 1997.
- [85] C. Chen, J. Luo and K. Parker, "Image segmentation via adaptive-mean clustering and knowledge-based morphological operations with biomedical applications," *IEEE Trans. Image Process.*, vol. 7, no. 12, pp. 1673-1683, 1998.
- [86] A. Riahi, "MRI image segmentation by k-means clustering method and detection of lesions," *Int. J. Recent Sci. Res.*, vol. 4, no. 6, pp. 2484-2492, 2015.
- [87] K. Muneer and K. Joseph, "Performance Analysis of Combined k-mean and Fuzzy-c-mean Segmentation of MR Brain Images," in *Computational Vision and Bio Inspired Computing*, 2018, pp. 830-836.
- [88] M. Sharma, G. Purohit and S. Mukherjee, "Information Retrieves from Brain MRI Images for Tumor Detection Using Hybrid Technique K-means and Artificial Neural Network (KMANN)," in *Networking Communication and Data Knowledge Engineering. Lecture Notes on Data Engineering and Communications Technologies*, vol. 4, Singapore, Springer, 2018.
- [89] K. Bhagwat, D. More, S. Shinde, A. Daga and R. Tornekar, "Comparative study of brain tumour detection using k-means, fuzzy c means and hierarchical clustering algorithms," *IJSER*, vol. 4, no. 6, pp. 626-632, 2013.
- [90] D. Gors, P. Suetens, R. Vandenberghe and P. Claes, "Hierarchical spectral clustering of MRI for global-to-local shape analysis: applied to brain variations in alzheimer's disease," in *IEEE 14th International Symposium on Biomedical Imaging*, Melbourne, 2017.
- [91] M. Celebi, Y. Aslandogan and P. Bergstresser, "Mining biomedical images with density-based clustering," in *Proceedings of the International Conference on Information Technology: Coding and Computing (ITCC'05)*, 2005.
- [92] S. Roy and D. Bhattacharyya, "Segmentation of cortical gray and white matters from MRI using density based clustering approach," in *2015 International Symposium on Advanced Computing and Communication (ISACC)*, Silchar, 2015.
- [93] S. Bandyopadyay and T. Paul, "Segmentation of Brain Tumour from MRI image – Analysis of Kmeans and DBSCAN Clustering," *International Journal of Research in Engineering and Science (IJRES)*, vol. 1, no. 1, pp. 48-57, 2013.
- [94] I. Kärkkäinen and P. Fränti, "Minimization of the value of Davies-Bouldin index," in *Proceedings of the IASTED International Conference on Signal Processing and Communications (SPC'2000)*, 2000.
- [95] D. Davies and D. Bouldin, "A cluster separation measure," *IEEE T. Pattern Anal.*, vol. 1, no. 2, pp. 224-227, 1979.

- [96] T. Calinski and J. Harabasz, "A dendrite method for cluster analysis," *Commun. Stat. - Theory Methods*, vol. 3, no. 1, pp. 1-27, 1974.
- [97] F. Pedregosa, G. Varoquaux, A. Gramfort, V. Michel, B. Thirion, O. Grisel, M. Blondel, P. Prettenhofer, R. Weiss, V. Dubourg, M. Vanderplas, A. Passos, D. Cournapeau, M. Brucher, M. Perrot and E. Duchesnay, "Scikit-learn: machine learning in {P}ython," *J. Mach. Learn. Res.*, vol. 12, pp. 2825-2830, 2011.
- [98] L. F. Chen, C. K. Ong, C. P. Neo, V. V. Varadan and V. K. Varadan, *Microwave Electronics: Measurement and Materials Characterization*, John Wiley & Sons, Ltd, 2004.
- [99] R. C. Conceição, J. J. Mohr and M. O'Halloran, *An Introduction to Microwave Imaging for Breast Cancer Detection*, Springer International Publishing, 2016.
- [100] T. Cameron, M. Okoniewski, E. Fear, D. Mew, B. Banks and T. Ogilvie, "A preliminary study of the electrical properties of healthy and diseased lymph nodes," in *14th International Symposium on Antenna Technology and Applied Electromagnetics [ANTEM] and the American Electromagnetics Conference [AMEREM]*, Ottawa, Canada, 2010.
- [101] W. Joines, Y. Zhang, C. Li and R. Jirtle, "The measured electrical properties of normal and malignant human tissues from 50 to 900 MHz.," *Med. Phys.*, vol. 21, no. 4, pp. 547-550, 1994.
- [102] J. Choi, J. Cho, Y. Lee, J. Yim, B. Kang, K. Oh, W. Jung, H. Kim, C. Cheon, H. Lee and Y. Kwon, "Microwave detection of metastasized breast cancer cells in the lymph node; potential application for sentinel lymphadenectomy.," *Breast Cancer Res. Treat.*, vol. 86, no. 2, pp. 107-115, 2004.
- [103] A. Malich, T. Boehm, M. Facius, H. Mentzel, M. Fleck, J. Bottcher, R. Anderson and W. Kaiser, "Use of electrical impedance scanning in the differentiation of sonographically suspicious and highly suspicious lymph nodes of the head-neck region," *Eur. Radiol.*, vol. 12, no. 5, pp. 1114-1120, 2002.
- [104] S. Gabriel, R. Lau and C. Gabriel, "The dielectric properties of biological tissues: II. Measurements in the frequency range 10 Hz to 20 GHz," *Phys. Med. Biol.*, vol. 41, no. 11, pp. 2251-2269, 1996.
- [105] S. Gabriel, R. Lau and C. Gabriel, "The dielectric properties of biological tissues: III. Parametric models for the dielectric spectrum of tissues," *Phys. Med. Biol.*, vol. 41, no. 11, pp. 2271-2293, 1996.
- [106] C. Gabriel, S. Gabriel and E. Corthout, "The dielectric properties of biological tissues: I. Literature survey," *Phys. Med. Biol.*, vol. 41, pp. 2231-2249, 1996.
- [107] "The finite-difference time-domain method," in *Computational Electromagnetics*, vol. 51, Springer New York, 2005, pp. 57-86.
- [108] S. Cruciani, V. De Santis, M. Feliziani and F. Maradei, "Cole-Cole vs Debye models for the assessment of electromagnetic fields inside biological tissues produced by wideband EMF sources," *2012 Asia-Pacific Symposium on Electromagnetic Compatibility*, pp. 685-688, 2012.

- [109] K. Chopra, D. Calva, M. Sosin, K. K. Tadisina, A. Banda, C. De La Cruz, M. R. Chaudhry, T. Legesse, C. B. Drachenberg, P. N. Manson and M. R. Christy, "A comprehensive examination of topographic thickness of skin in the human face," *Aesthet. Surg. J.*, vol. 35, no. 8, pp. 1007-1013, 2015.
- [110] K. S. Ugur, N. Ark, H. Kurtaran, G. Kizilbulut, B. Cakir, D. Ozol and M. Gunduz, "Subcutaneous fat tissue thickness of the anterior neck and umbilicus in patients with obstructive sleep apnea," *Otolaryngol. Head Neck Surg.*, vol. 145, no. 3, pp. 505-510, 2011.
- [111] V. Sabancioğulları, M. Koşar, İ. Şalk, F. Erdil, İ. Öztoprak and M. Çimen, "Diploe thickness and cranial dimensions in males and females in mid-anatolian population: an MRI study," *Forensic Sci. Int.*, vol. 219, no. 1-3, pp. 289.e1-289.e7, 2012.
- [112] G. Rankin, M. Stokes and D. Newham, "Size and shape of the posterior neck muscles measured by ultrasound imaging: normal values in males and females of different ages," *Man. Ther.*, vol. 10, no. 2, pp. 108-115, 2005.
- [113] Frederick Nat. Lab for Cancer Research , "The Cancer Imaging Archive (TCIA)," [Online]. Available: <https://www.cancerimagingarchive.net/#>. [Accessed April 2019].
- [114] S. Nag, Image Registration Techniques: A survey, engrXiv, 2017.
- [115] D. Zwillinger, "Affine Tranformations," in *CRC standard mathematical tables and formulae*, CRC Press LLC, 2003.
- [116] S. Patro and K. Sahu, "Normalization: a preprocessing stage," *CoRR*, 2015.
- [117] R. Haralick, S. Sternberg and X. Zhuang, "Image analysis using mathematical morphology," *IEEE T. Pattern Anal.*, vol. 9, no. 4, pp. 532-550, 1987.
- [118] S. Gabriel and C. Gabriel, "Compilation of the Dielectric Properties of body tissues at RF and Microwave frequencies," June 1996. [Online]. Available: <http://niremf.ifac.cnr.it/docs/DIELECTRIC/Report.html>. [Accessed May 2019].
- [119] R. Eleutério, Microwave Imaging of the Axilla to Aid Breast Cancer Diagnosis, Lisbon: Faculdade de Ciências e Tecnologia - Universidade Nova de Lisboa, 2014.
- [120] E. Zastrow, S. Davis, M. Lazebnik, F. Kelcz, B. Van Veen and S. Hagness, "Development of anatomically realistic numerical breast phantoms with accurate dielectric properties for modelling microwave interactions with the human breast," *IEEE Trans. Biomed. Eng.*, vol. 55, no. 12, pp. 2792-2799, 2008.
- [121] T. Zhang, R. Ramakrishnan and M. Livny, "BIRCH: A new data clustering algorithm and its applications," *Data Min. and Knowl. Discov.*, vol. 1, pp. 141-182, 1997.
- [122] R. Bansal, L. Staib, A. Laine, X. Hao, D. Xu, J. Liu, M. Weissman and B. Peterson, "Anatomical brain images alone can accurately diagnose chronic neuropsychiatric illnesses," *PLOS ONE*, vol. 7, pp. 1-21, 2012.



- [123] C. Lambert, E. Zeestraten, O. Williams, P. Benjamin, A. Lawrence, R. Morris, A. Mackinnon, T. Barrick and H. Markus, “Identifying preclinical vascular dementia in symptomatic small vessel disease using MRI,” *Neuroimage Clin.*, vol. 19, pp. 925-938, 2018.
- [124] S. Huang, B. Franc, R. Harnish, G. Liu, D. Mitra, T. Copeland, V. Arasu, J. Kornak, E. Jones, S. Behr, N. Hylton, E. Price, L. Esserman and Y. Seo, “Exploration of PET and MRI radiomic features for decoding breast cancer phenotypes and prognosis,” *NPJ Breast Cancer*, vol. 24, no. 4, 2018.
- [125] C. Aggarwal, Data mining: the textbook, 1st edition ed., Springer Science+Business Media, 2015.
- [126] J. Palacio Niño and F. Berzal, “Evaluation Metrics for Unsupervised Learning Algorithms,” 2019. [Online]. Available: <https://arxiv.org/abs/1905.05667>.

# Appendix A

## Anthropomorphic models of the Head and Neck for Microwave Imaging



Ciências  
ULisboa

Ana Catarina Pelicano<sup>1</sup>, Raquel C. Conceição<sup>2</sup>

<sup>1</sup> Faculdade de Ciências da Universidade de Lisboa, 1749-016, Lisboa, Portugal

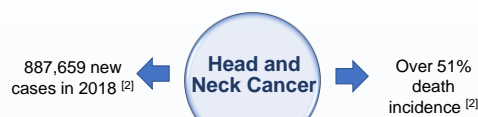
<sup>2</sup> Instituto de Biofísica e Engenharia Biomédica, Faculdade de Ciências da Universidade de Lisboa, 1749-016, Lisboa, Portugal



### ABSTRACT

Currently there is no satisfactory neoadjuvant (i.e. pre-operative) diagnosis to assess whether cancer has spread to neighbouring lymph nodes (LNs). State of the art clinical diagnosis of head and neck cancer often involves removal of Cervical LNs (CLNs) for TNM staging [1]. We propose that LNs within the head and neck region are a prime target for clinical diagnosis using MicroWave Imaging, both because of their shallow location and dielectric properties. We aim to create realistic anthropomorphic models of the head and neck for later testing of a full MWI prototype system, capable of imaging and diagnosing CLNs. This includes developing anthropomorphic phantoms, using state-of-the-art segmentation algorithms.

### INTRODUCTION



In 80% of these cancer cases, cancer cells metastasise through lymphatic and blood vessels [3]

#### STANDARD DIAGNOSIS METHODOLOGY OF CERVICAL LYMPH NODES – NECK DISSECTION



NEGATIVE IMPACT IN PATIENTS AND HEALTH SYSTEMS [4]

- Slow physical recovery;
- Physical deformations (scars);
- Affects speech and swallowing;
- Lymphoedema.



### MICROWAVE IMAGING

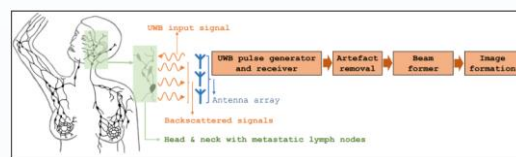


Figure 1. Schematic representing the typical methodology steps of the UWB radar imaging system.

Low cost

Non-ionising

Ultra Wideband (UWB)  
Radar for Microwave  
Imaging

Non-invasive

Low power

### GOAL

Development of anthropomorphic models of the head and neck for later testing in a full MWI prototype system, capable of imaging and diagnosing CLNs.

### METHODOLOGY



### RESULTS

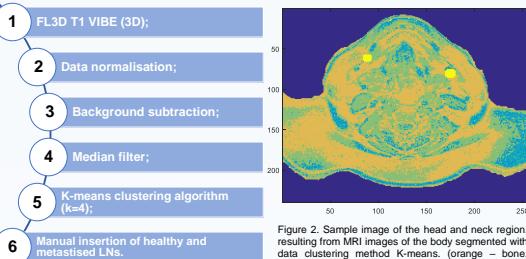


Figure 2. Sample image of the head and neck region, resulting from MRI images of the body segmented with data clustering method K-means. (orange – bone, green – muscle, blue – heterogeneous tissue, yellow – LNs.

### CONCLUSIONS AND FUTURE WORK

- By using this pipeline, we are able to reasonably differentiate tissues in the head and neck region.
- In future work, different MRI sequences will be considered, both because of their worldwide usage in clinical applications and their ability to separate tissues.
- Further tests will help determine the optimal image processing methodology and machine learning algorithms for clustering.

### REFERENCES

- [1] American Joint Committee on Cancer, Breast Cancer Staging, 7th Edition Staging Posters ed., 2009.
- [2] International Agency for Research on Cancer, "World Health Organization, GLOBOCAN 2018: Estimated Cancer Incidence, Mortality and Prevalence – Worldwide in 2018".
- [3] S. Remmert, M. Rottmann, M. Reichenbach, K. Sommer and H. Friedrich, "Lymphknotenmetastasierung bei Kopf-Hals-Tumoren (Lymph node metastasis in head-neck tumors)," Laryngo-Rhino-Otologie, vol. 80, no. 1, pp. 27-35, 2001.
- [4] M. Sapienza, M. Tixier, J. Endo, G. Neto, M. Lopez, S. Nakagawa, F. Belfort, J. Soares Jr, S. Lewin and M. Marone, "The role of sentinel node mapping in malignant melanoma: Experience with 99mTc-phytate and a review of the literature," Anais Brasileiros de Dermatologia, vol. 79, no. 2, pp. 181-191, 2004.
- [5] R. Gonzalez and R. Woods, Digital Image Processing, 3rd ed., NJ, USA: Prentice-Hall, Inc, 2006, pp. 167-180.
- [6] J. Han, M. Kamber and J. Pei, Data Mining, concepts and techniques, 3rd ed., MA, USA: Elsevier, 2012, pp. 443-496.

## Appendix B

# Head and Neck Numerical Phantom Development for Cervical Lymph Node Microwave Imaging

Ana Catarina Pelicano<sup>1</sup>, Raquel C Conceição<sup>2</sup>

<sup>1</sup> Faculdade de Ciências da Universidade de Lisboa, 1749-016 Lisbon, Portugal, [catarina\\_pelicano@hotmail.com](mailto:catarina_pelicano@hotmail.com)

<sup>2</sup> Instituto de Biofísica e Engenharia Biomédica, Faculdade de Ciências da Universidade de Lisboa, 1749-016 Lisbon, Portugal, [rcconceicao@fc.ul.pt](mailto:rcconceicao@fc.ul.pt)

**Abstract**—In this paper, we present a methodology to build a numerical phantom for the head and neck regions, which can be used to develop a cervical lymph node microwave imaging device. We have shown a pipeline of data processing steps which can be applied to Magnetic Resonance Images (MRI) of the head and neck. Such models will be the starting point to start developing a microwave imaging device suitable to detect metastasised cervical lymph nodes and as a result contribute to the correct staging of head and neck cancer.

**Index Terms**— cervical lymph nodes; MRI segmentation; microwave imaging.

### I. Motivation

Head and neck cancer is a broad term referring to any epithelial malignancies arising in the paranasal sinuses, nasal and oral cavity, salivary glands, pharynx, and larynx. This type of cancer reported 887,659 worldwide new cases in 2018, with over 51% death incidence [1]. In up to 80% of these cancer cases, cancer cells metastasised through lymphatic and blood vessels [2] [3].

Currently there is no satisfactory neoadjuvant (i.e. pre-operative) diagnosis to assess whether cancer has spread to neighbouring Lymph Nodes (LNs). The assessment of LNs within the head and neck region often requires their surgical removal and subsequent histopathology. This practice frequently results in the removal of healthy Cervical LNs (CLNs), which ultimately has negative impact on the patient's health and quality of life, and also on the economy of a country, due to the high costs of surgeries and follow-up therapies supported by healthcare systems [4] [5].

If CLNs could be accurately diagnosed with a non-invasive approach ahead of surgery, the quality of life of cancer patients and survivors could potentially be significantly improved and the burden on patients and on healthcare systems reduced [6] [7].

### II. Introduction

As a result of the lack of alternatives to assess CLNs, MicroWave Imaging (MWI) presents itself as an interesting option. Medical MWI uses signals based on the dielectric contrast between different

tissues, propagating through the body to detect internal structures.

Radar MWI operates by illuminating an anatomical region of interest (or models mimicking that region) with an Ultra WideBand (UWB) pulse, and recording and processing the resulting backscattered signals. Medical radar MWI systems typically comprise: UWB antennas, transmit/receive electronics, and dedicated skin artefact removal and beamforming algorithms. Skin artefact removal algorithms remove the large reflection produced by the skin surface; beamforming focuses the backscattered signals so that signals from high scattering regions (e.g. tumour tissues) are combined coherently and signals from clutter are combined incoherently; finally resulting in an image which shows the dielectric scatterers [8] [9]. Instead of creating anatomical images of the body, radar-based MWI creates a map of microwave scattering, which translates in a map of the dielectric properties of the irradiated area. Here, the abnormalities in the tissues are easily detected and quantified [10]. In addition to being a comfortable and non-invasive imaging modality, it is also portable, low-cost, user-independent, and uses low-power.

MWI has gained significant momentum in the past few years with numerous research projects, patient studies [8] [9] and clinical trials [11] [12], and new products being brought to market (e.g. MARIATM [13]), mostly in the area of breast cancer and stroke detection. Although MWI technology has matured considerably for some clinical applications, performance improvements are required to make clinical usage feasible.

The main objective of this paper is to use Machine Learning techniques to create realistic anthropomorphic phantoms which can be later used to develop medical MWI systems for screening and diagnosis, as there is a significant diagnostic blind-spot regarding mass screening of lymph nodes in the case of head and neck cancers.

As screening CLNs using a microwave UltraWideBand (UWB) radar technology has never been attempted before, the first steps comprise

modelling the head and neck region according to its anatomy, with special attention to tissue architecture, distribution, and dielectric properties. This includes developing three-dimensional (3D) anthropomorphic phantoms of the head and neck region, using state-of-the-art segmentation algorithms and assigning the realistic dielectric properties of biological tissues to the segmented tissues. In order to create a 3D realistic MRI-derived phantom of the head and neck regions, a thorough study of Data Mining (DM) clustering techniques for data segmentation must be conducted. Furthermore, metrics such as Silhouette are used for clustering evaluation and algorithm selection purposes. As the dielectric properties of the tissues modelled are to be incorporated into the 3D anatomically realistic model, 4-pole-Cole-Cole model is used to describe the behaviour of the dielectric properties of the biological tissues with frequency.

### III. Materials

The phantoms developed were based on MRI data downloaded from a public archive of medical images of cancer, The Cancer Imaging Archive (TCIA) [14]. In particular, from a “collection” called The Cancer Genome Atlas Head-Neck Squamous Cell Carcinoma (TCGA-HNSC), hence different scanner modalities, manufactures and acquisition protocols were available. DICOM files from TCIA were visualised and exploited with RadiAnt DICOM Viewer software. A manually created mask for later background subtraction was obtained from iSEG® software. Software toolkits and toolboxes (e.g. Numpy, Scipy, Scikit-learn from Python™, and Statistics and Machine Learning in Toolbox™ in MATLAB®) were used for the creation of unsupervised Machine Learning (ML) algorithms for data segmentation, with reported applications in medical imaging [15]. Furthermore, 3D Slicer software (version 4.10.1) was used to perform image registration techniques.

### IV. Methodology and Results

#### A. MRI Data Selection

Exams of five different subjects were examined on their ability to fulfil conditions such as: (i) slices must be orthogonal to the coordinate axes, (ii) the resolution and signal-to-noise ratio must allow a clear and easy visual identification of the main biological structures. The MRI sequences available include: T1, T1 post contrast, T1 FLAIR, T1 Turbo Spin-Echo (TSE), FL3D T1 VIBE, T2 STIR and T2 with SPAIR. Later, combinations of data, for the chosen patient, were also considered.

#### B. Pre-processing methodologies

Data normalisation was the first step in data pre-processing, which permitted to scale the data values

in a specific range (in this case, 0.0 to 255.0). We have used the Minimum-Maximum normalisation.

Binary masks were created to eliminate background noise. Firstly, a threshold was applied to the original images resulting in binary images where the original pixels with values below the threshold were represented with 0's and the pixels with values above, with 1's. This threshold was empirically determined; only one condition was taken into consideration when choosing this value: no pixels outside the body region can be included in the mask. The resulting mask is tolerable as it could be later corrected. The small gaps in the anatomical region after the application of the threshold were addressed by using *Close*, a morphological operation that allows the filling of small holes. Finally, by applying the mask of each slice to the original data we have removed the background.

MRI images are generally prone to Gaussian noise and Salt and Pepper noise due to image acquisition errors, such as sensor noise and electronic circuit noise, and transmission errors [16]. The removal of noise, which corrupts the information in the image, and the smoothness of other sharp transitions (e.g. edges) can be accomplished by using filters in the frequency domain. High frequencies are responsible for detail, *i.e.*, sharp transitions such as noise and edges. If the goal is to remove noise, then filters capable of suppressing high frequencies while leaving the low frequencies unchanged should be applied - the LowPass (LP) filters. In this work we have considered the ideal, Butterworth and Gaussian filters, which cover the range from very sharp (ideal) to very smooth (Gaussian) filter functions. The non-linear median filter was also tested as it is very effective in the presence of Salt and Pepper noise [17]. Besides testing each filter individually, some filters combinations were also attempted in order to obtain the best conjugation of filters characteristics which provided better quality images.

#### C. Segmentation Algorithms (Data Mining Clustering)

DM is the process of discovering interesting patterns and knowledge from massive amounts of data. Typically, we use clustering methods, also known as unsupervised learning, to discover hidden patterns within the data [18] [19]. Hence, it is one of the processes in segmentation successfully applied to medical image analysis [20]. Clustering is the process of grouping a set of data objects into clusters (which should correspond to different classes) by maximizing intraclass similarity and minimizing interclass similarity. Traditional clustering techniques are broadly classified into the following categories: partitioning methods, hierarchical methods, density-based methods, and grid-based methods [18]. The proximity measure is an important step since it allows the definition of the concept of

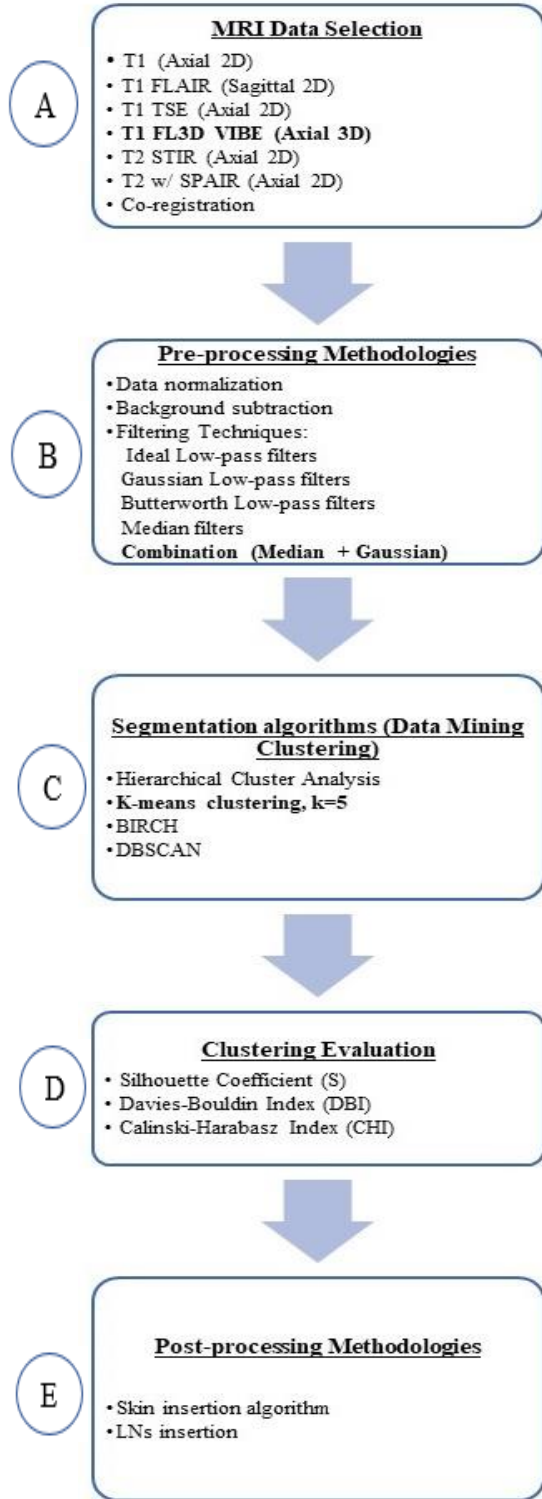


Fig 1. Pipeline with processing steps from MRI images to full 3D numerical model of the head and neck regions.

similarity between data samples [21]. The clustering algorithms tested include: Agglomerative Hierarchical Cluster Analysis, K-means clustering, BIRCH and DBSCAN.

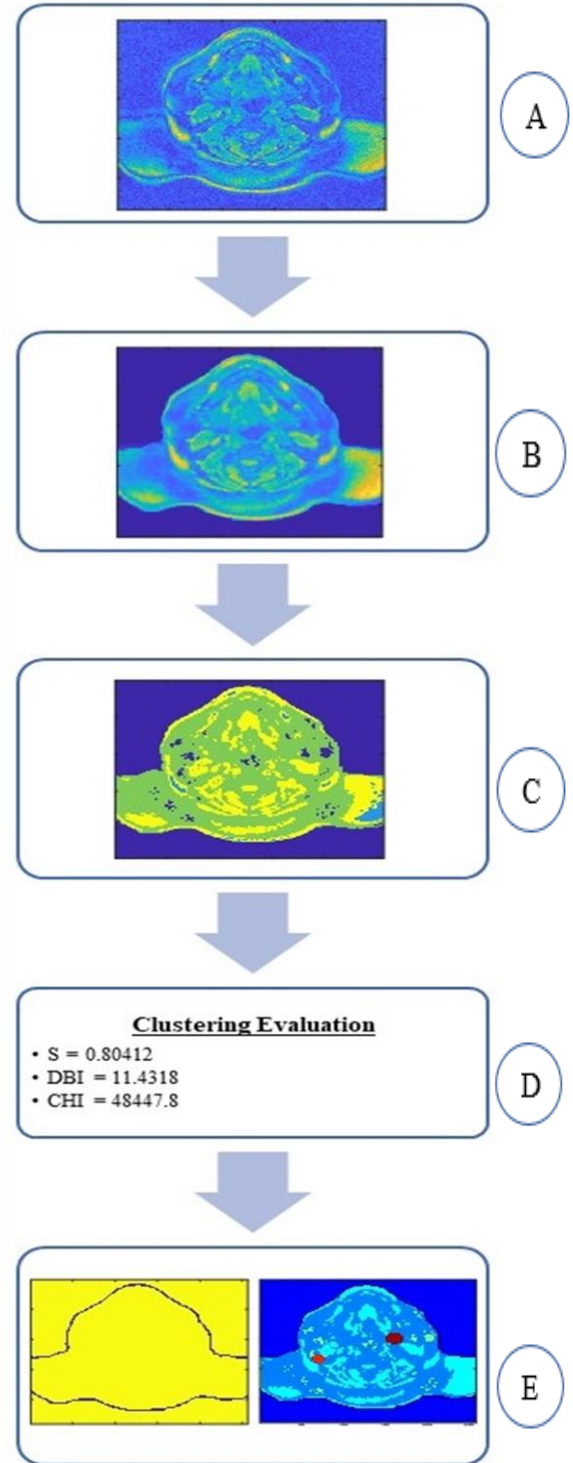


Fig 2. Intermediate results obtained when applying the pipeline with processing steps from MRI images to full 3D numerical model of the head and neck regions (matching with Fig.1).

#### D. Clustering Evaluation

After applying a clustering algorithm, it is important to assess how good the resulting clusters are. When the ground truth of a data set is not

available, intrinsic methods which evaluate the goodness of a clustering by considering how well the clusters are separated are used [18]. Some of the intrinsic methods tested in this work included: the silhouette coefficient, the David-Bouldin index, and the Calinski-Harabasz index, which are detailed below.

The Silhouette coefficient is computed for all objects of a data set. Its value varies between 1 and -1, whether the cluster containing the object is compact and the object is far away from other clusters, or the object is closer to objects in other clusters rather than objects within the same group, respectively [18].

The Davies-Bouldin Index (DBI) takes into consideration both errors caused by representing the data objects with their cluster centroids (intra cluster diversity) and the distance between clusters (inter cluster diversity). Values closer to zero indicate a better partition of the data [22].

The Calinski-Harabasz Index (CHI) expresses the ratio of between cluster variance and the overall within cluster variance. A higher value of CHI relates to a model with better defined clusters [23].

#### E. Post-processing methodologies

After the application of the segmentation algorithms we have encountered some difficulties.

As the skin tissue was not identified in a particular cluster, we have developed an algorithm which allowed the introduction of synthetic layer of skin. The inputs were the volume of binary masks and the thickness of the skin layer, which was fixed to 1.4 mm. In each slice of the transverse plane, which divides the body into superior and inferior parts, this algorithm detects changes in the values of the mask. Then, a layer of skin is introduced at the surface of the body region towards the interior.

After the application of segmentation algorithms, the LNs were not distinguishable from other body regions. In order to address this problem, we have chosen to proceed with the manual insertion of the LNs, following the anatomical description given in [24].

The classification of the LNs into the appropriate 6 anatomical levels required a thorough study of the anatomy. The determination of these frontiers was a procedure with several approximations and simplifications.

The methodology from A to E, and resulting intermediate results are represented in Fig. 1 and Fig. 2, respectively, in which we highlighted the optimal algorithms for each processing step.

#### F. Assignment of Dielectric Properties

The models created within the scope of this paper are compatible with future studies that use FDTD simulation. As Cole-Cole models offer a suitable

approach for representing the frequency variation of the relative permittivity and conductivity of many biological tissues, they will be implemented. In particular, the 4-Cole-Cole model, which is considered the best fitting technique as it describes the four relaxation mechanisms exhibited by biological tissues in a frequency range of 10Hz to 100 GHz [25]. Initially, to assign dielectric properties to MRI derived models, four dielectric properties curves for permittivity and conductivity were considered: a curve for skin, bone, fat and muscle tissue. In order to account for the dielectric differences within bone, fat and muscle tissue due to physiological processes, a dielectric variation of 5% with respect to the nominal property was incorporated [26]. Thus, we have obtained seven curves of the dielectric properties: one for the skin tissue, and two curves which limit the lower and upper bond for the bone, fat and muscle tissues. Although the curves cover a large range of frequency, we have only depicted the range of interest in Fig. 3. The 4-Cole-Cole parameters for each curve were found in [26]. Healthy and malignant lymph nodes were modelled according to the values obtained from [27] as the 4-Cole-Cole parameters for these tissues are not available. The parameters used to model the LNs refer to the Debye model, which is a simplification of the 4-Cole-Cole model, hence we have used the Debye parameters to define the 1<sup>st</sup> pole of the 4-Cole-Cole model and the 2<sup>nd</sup>-3<sup>rd</sup>-4<sup>th</sup> poles were assumed to be null. Fig. 4 depicts the four curves of the dielectric properties of the healthy and metastasised LNs, both cross-section and surface. As before, this figure only covers the frequency range of interest for our application.

The assignment of the dielectric properties results in a matrix with the same dimensions as the model, in which each voxel contains the dielectric properties values, for a user specified frequency, of the correspondent voxel of the model. In order to obtain this, several steps occur: (1) For each cluster, the

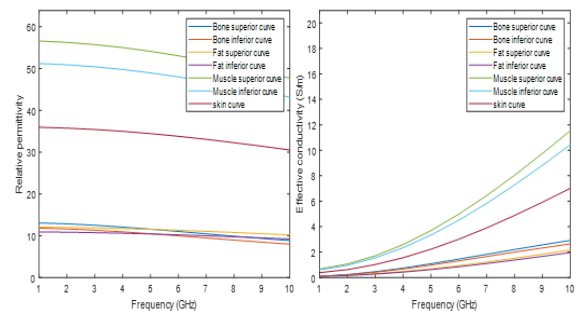


Fig. 3. Dielectric properties curves considered to assign the dielectric properties to the tissues in the cervical region, which are represented in the developed models and phantom generator. The graph on the left depicts the permittivity curves, and the graph on the right shows the conductivity curves, for the considered biological tissues. Both curves were obtained by using the 4-Cole-Cole formulation.



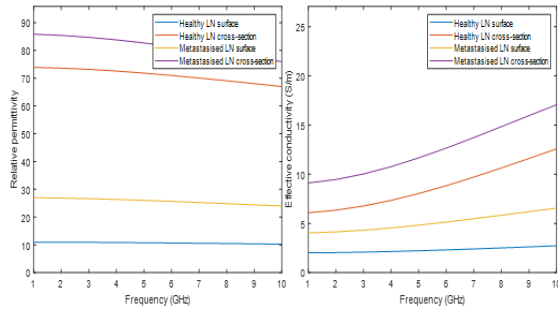


Fig. 4. Dielectric properties curves considered to assign the dielectric properties to the LNs which are inserted in the developed models. The graph on the left depicts the permittivity curves, and the graph on the right shows the conductivity curves, for the healthy and unhealthy cross-section and surface of the LNs. Both curves were obtained by using the 4-Cole-Cole formulation, the missing 4-Cole.Cole parameters were assumed to be null.

maximum and the minimum value of the intensity of the MRI scan is determined, (2) To these maximum and minimum intensity voxels, we associate the superior curve and the inferior curve of the tissue, respectively, (3) The remaining voxels of the same cluster are linearly mapped to a value between the curves of that tissue.

## V. Discussion and Conclusions

In this work, MRI exams of five different patients whose clinical data was acquired using different protocols, were studied. Our preference was to choose images with the higher resolution in all anatomical planes. We observed that the differences in the resolution of sagittal and coronal planes between all the exams were not as significant as the differences of resolutions in the axial plane. Therefore, T1 FL3D VIBE sequence was chosen over the others given its significant higher resolution in the axial plane. The combination of the different exams was also excluded since we could not infer additional anatomical information.

Both Ideal and Butterworth filters resulted in images with several small-sized granularities, which compromise 3D-printed phantoms. Median filters were proved the best for smoothing edges and Gaussian filters were very effective in removing noise. The combination of the last two was proven the best approach for data pre-processing since it allowed the best anatomical information retrieval.

No useful segmentation was obtained from DBSCAN and BIRCH algorithms. In the first case, the algorithm was not capable of grouping data points in large clusters with anatomical meaning, instead, only small and very dispersive clusters were found. Hence, we have excluded the DBSCAN algorithm for clustering. The results of BIRCH showed severe loss of anatomical information for  $k \leq 4$ , and several small-sized granularities for  $k \geq 5$ . Neither option is appropriate to be used in our model, thus, BIRCH

algorithm was excluded from the methodology pipeline. Although providing clustering with anatomical meaning, HCA algorithms showed unreasonable computational costs - 8h per slice and approximately ~32 days to cluster the initial volume (Intel® Core™ i7-3630QM and 16.0 GB). Besides, between slice cluster verification was required. Finally, K-means clustering was the chosen algorithm given its speed and good clustering quality. In order to determine the optimal  $k$  for each algorithm, three different metrics were calculated. Results showed that good values of metrics did not imply a good anatomical information retrieval – this was observed empirically. As a result, visual inspection and prior anatomical knowledge were used to assess the segmentation quality. To finalise the model, skin tissue and CLNs were manually inserted followed by the assignment of the dielectric properties to the tissues.

Future work will include the incorporation of this model in a realistic anthropomorphic phantom generator, which can be later used to develop medical MWI systems for screening and diagnosis CLNs.

## Acknowledgment

This work is supported by Fundação para a Ciência e a Tecnologia-FCT, FCT/MEC (PIDDAC) under the Strategic Programme UID/BIO/00645/2013.

## References

- [1] International Agency for Research on Cancer, "World Health Organization, GLOBOCAN 2018: Estimated Cancer Incidence, Mortality and Prevalence Worldwide in 2018," In: <http://gco.iarc.fr/>.
- [2] S. Remmert, M. Rottmann, M. Reichenbach, K. Sommer and H. Friedrich, "Lymphknotenmetastasierung bei Kopf-Hals-Tumoren (Lymph node metastasis in head-neck tumors)," *Laryngo-Rhino-Otologie*, vol. 80, no. 1, pp. 27-35, 2001.
- [3] N. Patani, M. Dwek and M. Douek, "Predictors of axillary lymph node metastasis in breast cancer: A systematic review," *Eur J Surg Oncol*, vol. 33, no. 4, pp. 0748-7983, 2007.
- [4] M. Sapienza, M. Tavares, I. Endo, G. Neto, M. Lopes, S. Nakagawa, et al., "The role of sentinel node mapping in malignant melanoma: Experience with 99mTc-phytate and a review of the literature," *Anais Brasileiros de Dermatologia*, vol. 79, no. 2, pp. 181-191, 2004.
- [5] S. Exposto, Personal communication, 2014.
- [6] S. G. Komen, "Facts for Life: Axillary Lymph Node," 2009. In: [http://ww5.komen.org/uploadedfiles/Content\\_Binaries/806-392a.pdf](http://ww5.komen.org/uploadedfiles/Content_Binaries/806-392a.pdf).
- [7] Cancer Research UK, "Lymphoedema after breast cancer treatment," In: <https://www.cancerresearchuk.org/about-cancer/breast-cancer/living-with/lymphoedema-after-treatment>.
- [8] E. Fear, J. Bourqui, C. Curtis, D. Mew, B. Docktor and C. Romano, "Microwave breast imaging with a monostatic radar-based system: A study of application to patients," *IEEE Transactions on Microwave Theory and Techniques*, vol. 61, no. 5, pp. 2119-2128, 2013.

- [9] E. Porter, K. Duff, M. Popovic and M. Coates, "Investigation of time-domain microwave radar with breast clinic patients," in 10th EuCAP, Switzerland, 2016, pp. 1-3.
- [10] E. Fear, "Microwave Imaging of the Breast," *Technol Cancer Res Treat*, vol. 4, no. 1, pp. 69-82, 2005.
- [11] F. Yang, L. Sun, Z. Hu, H. Wang, D. Pan, R. Wu, et al., "A large-scale clinical trial of radar-based microwave breast imaging for Asian women: Phase I," in 2017 IEEE APS-USNC/URSI, San Diego, CA, USA, 2017, pp. 781-783.
- [12] A. Preece, I. Craddock, M. Shere, L. Jones and H. Winton, "MARIA M4: clinical evaluation of a prototype ultrawideband radar scanner for breast cancer detection," *J Med Imaging*, vol. 3, no. 3, pp. 033502.1-7, 2016.
- [13] Micrima Limited, "Micrima - Evolving Medical Imaging," 2018. In: <http://micrima.com/>.
- [14] Frederick Nat. Lab for Cancer Research, "The Cancer Imaging Archive (TCIA)," In: <https://www.cancerimagingarchive.net/#>.
- [15] University of Oxford, "Biomedical Image Analysis - Institute of Biomedical Engineering," 2018. In: [www.ibme.ox.ac.uk/research/biomed](http://www.ibme.ox.ac.uk/research/biomed).
- [16] H. Ali, "MRI Medical Image Denoising by Fundamental Filters," *SCIREA Journal of Computer*, vol. 2, no. 1, pp. 12-26, 2017.
- [17] R. Gonzalez and R. Woods, *Digital Image Processing*, New Jersey: Prentice Hall, 2002.
- [18] J. Han, M. Kamber and J. Pei, *Data Mining, concepts and techniques*, 3rd ed., MA, USA: Elsevier, 2012, pp. 443-496.
- [19] P. Berkhin, "A Survey of Clustering Data Mining Techniques," in *Grouping Multidimensional Data*, Springer, Berlin, Heidelberg, 2006, pp. 25-71.
- [20] S. Roy and D. Bhattacharyya, *Data Mining Techniques and Its Application in Medical Imagery*, Germany: VDM Verlag Dr. Müller, 2010.
- [21] G. Mirzaei and H. Adeli, "Segmentation and Clustering in Brain MRI Imaging," *Rev Neurosci*, 2018.
- [22] I. Kärkkäinen and P. Fränti, "Minimization of the value of Davies-Bouldin index," in *Proceedings of the IASTED-SPC*, 2000.
- [23] F. Pedregosa, G. Varoquaux, A. Gramfort, V. Michel, B. Thirion, O. Grisel, et al., "Scikit-learn: Machine Learning in {P}ython," *J. Mach. Learn. Res.*, vol. 12, pp. 2825-2830, 2011.
- [24] R. Seeley, P. Tate and T. Stephens, *Anatomy and Physiology*, 8th Edition ed., McGraw-Hill Higher Education, 2007.
- [25] S. Cruciani, V. De Santis, M. Feliziani and F. Maradei, "Cole-Cole vs Debye Models for the assessment of Electromagnetic Fields inside Biological Tissues Produced by Wideband EMF Sources," in *Asia-Pacific Symposium on Electromagnetic Compatibility*, 2012.
- [26] S. Gabriel and C. Gabriel, "Compilation of the Dielectric Properties of body tissues at RF and Microwave frequencies," 1996. In: <http://niremf.ifac.cnr.it/docs/DIELECTRIC/Report.html>.
- [27] R. Eleutério, *Microwave Imaging of the Axilla to Aid Breast Cancer Diagnosis*, Lisbon: Faculdade de Ciências e Tecnologia - Universidade Nova de Lisboa, 2014.



Table C 1: Parameters of the 4-Cole-Cole Formulation, in a frequency range from 10 Hz to 20 GHz, for the cervical tissues represented in the developed models and phantom generator.

| Tissues | $\epsilon_{\infty}$ | $(\sigma_2)$<br>[S/m] | $\Delta \epsilon_1$ | $\Delta \epsilon_2$ | $\Delta \epsilon_3$ | $\Delta \epsilon_4$ | $\alpha_1$ | $\alpha_2$ | $\alpha_3$ | $\alpha_4$ | $\tau_1$<br>[ps] | $\tau_2$<br>[ns] | $\tau_3$<br>[μs] | $\tau_4$<br>[ms] |
|---------|---------------------|-----------------------|---------------------|---------------------|---------------------|---------------------|------------|------------|------------|------------|------------------|------------------|------------------|------------------|
| Bone    | 2.500               | 0.020                 | 10.00               | 180.0               | 5.00E+3             | 1.00E+5             | 0.200      | 0.200      | 0.200      | 0.000      | 13.263           | 79.577           | 159.155          | 15.915           |
| Fat     | 2.500               | 0.035                 | 9.00                | 35.00               | 3.30E+4             | 1.00E+7             | 0.200      | 0.100      | 0.050      | 0.010      | 7.958            | 15.915           | 159.155          | 15.915           |
| Muscle  | 4.000               | 0.200                 | 50.00               | 7000                | 1.20E+6             | 2.50E+7             | 0.100      | 0.100      | 0.100      | 0.000      | 7.234            | 353.678          | 318.310          | 2.274            |
| Skin    | 4.000               | 0.000                 | 32.00               | 1100                | 0.000               | 0.000               | 0.000      | 0.200      | 0.200      | 0.200      | 7.234            | 32.481           | 159.155          | 15.915           |

Table C 2: Parameters of the Debye models for LNs from [114] suitable to extract dielectric properties at a centre frequency of 7.5 GHz, applied to a 1-Cole-Cole Model.

| Tissues                       | $\epsilon_{\infty}$ | $(\sigma_2)$<br>[S/m] | $\Delta \epsilon_1$ | $\alpha_1$ | $\tau_1$<br>[ps] |
|-------------------------------|---------------------|-----------------------|---------------------|------------|------------------|
| Healthy LN surface            | 8.00                | 2.00                  | 3.00                | 0.200      | 9.24             |
| Healthy LN cross-section      | 47.00               | 6.00                  | 27.00               | 0.200      | 9.40             |
| Metastatised LN surface       | 17.00               | 4.00                  | 10.00               | 0.100      | 10.47            |
| Metastatised LN cross-section | 55.00               | 9.00                  | 31.00               | 0.000      | 11.00            |

## Appendix C